

3D SCANNING IMPERFECTION MEASUREMENTS FOR FEM ANALYSIS OF STEEL LINKS

Candidate: Eng. Viktor SZALAI

Scientific coordinator: Professor Dr. Eng. Aurel STRATAN

Session: June 2023

ABSTRACT

Prin dezvoltarea rapidă a tehnologiilor de scanare 3D și implementarea unor concepte relativ noi, precum digital twin și reverse engineering în industria construcțiilor, a fost identificată o nouă aplicație inovativă: măsurarea imperfecțiunilor geometrice reale și crearea de modele 3D pentru simulări cu elemente finite. În analiza cu metoda elementelor finite (FEM), construirea modelelor tridimensionale (3D) cu imperfecțiuni geometrice reale ale structurilor sau elementelor structurale din oțel poate fi dificilă din punct de vedere tehnic și necesită un consum important de timp. Până în prezent, nu exista o abordare automată robustă pentru conversia măsurătorilor obținute pe baza scanării 3D, într-un model valid pentru analize numerice cu elemente finite (FEA). În această lucrare a fost propusă o modalitate simplă și practică care poate converti norul de puncte obținut în urma scanării 3D într-un model cu elemente finite. Un alt obiectiv al acestei lucrări a fost sintetizarea metodologiilor și tehnologiilor existente de scanare 3D propuse în literatura științifică și de industrie. Pe parcursul lucrării, sunt revizuite diferite tipuri de tehnici conexe, precum scanarea laser terestră și aeriană (LiDAR), scanarea cu laser albastru, cu lumină structurată, fotogrametria (terestră, aeriană). De asemenea, lucrarea cuprinde un studiu de caz care abordează problematica prelucrării norilor de puncte tridimensionali care sunt generați pe baza scanării 3D. Au fost selectate 5 tehnologii distincte de scanare 3D pentru măsurarea unor linkuri demontabile din oțel inoxidabil pentru cadre contravântuite excentric, cu scopul de a evalua imperfecțiunile geometrice reale, precum și pentru utilizarea directă în simulări cu elemente finite a imperfecțiunilor măsurate.

ABSTRACT

Along with the rapid development of 3D scanning technologies, and the implementation of relatively new processes such as digital twinning and reverse engineering in the construction industry, an appropriate application of these in FEM simulations for example, can greatly facilitate analysis of real geometries when is needed. In this study, a new approach to construct 3D finite element models using advanced techniques in the field of 3D scanning is introduced. In the finite element method (FEM), constructing three-dimensional (3D) models with real geometric imperfections of structures or structural elements can be technically difficult and time inefficient. To date, there is no robust automated approach to translate this data directly into a valid model for FE analysis. In this thesis it was studied how to provide a simple and practical procedure that can convert point clouds to FE models. Another objective of this thesis is to provide an overview of 3D scanning methodologies and technologies proposed in the existing scientific and industrial literature. Throughout the thesis, various types of the related techniques are reviewed, which consist, mainly, of close-range, aerial, terrestrial photogrammetry, and mobile, terrestrial and airborne laser scanning, as well as time-of-flight, structured-light and phase-shift methods. Also, the work includes a case study that addresses the issue of processing three-dimensional point clouds that are generated from 3D scans. Five distinct 3D scanning technologies were selected for the measurement of replaceable stainless steel links used for eccentrically braced frames for the purpose of evaluating real geometric imperfections as well as for direct use in finite element simulations of measured imperfections.

ACKNOWLEDGMENTS

First and foremost, I am extremely grateful to my supervisor, Prof. Dr. Eng. Aurel Stratan for his invaluable advice, continuous support, and patience during my MSc. study. I would also like to thank PhD. student Eng. Anna Ene, PhD. student Eng. Paul Zdrenghia, Msc. student Eng. Andreea Diana Clepe, Prof. Dr. Eng. Sorin Herban, BSc. Student Cristian Farkas, the companies CadWorks Intl., and Hexagon Manufacturing Intelligence for their technical support on my study. I would like to thank Prof. Dr. Eng. Daniel Grecea, Eng. Ovidiu Abrudan, Tech. Milojko Ung, and all the personnel of the Department of Steel Structures and Structural Mechanics. It is their kind help and support that have made my study and life in the past two years a wonderful time. Finally, I would like to express my gratitude to my parents, my girlfriend, my grandparents, and all my family. Without their tremendous understanding and encouragement in the past few years, it would have been impossible for me to complete my study.

CONTENTS

1	INTRODUCTION	17
2	3D SCANNING FUNDAMENTALS	19
2.1	GENERAL INFORMATION	19
2.2	HISTORY OF 3D SCANNING	20
3	OVERVIEW OF 3D SCANNING TECHNOLOGIES	23
3.1	CONTACT TECHNIQUE	23
3.1.1	TRADITIONAL COORDINATION MEASURING MACHINE (CMM)	24
3.1.2	PORTABLE COORDINATE MEASURING MACHINES	27
3.2	NON-CONTACT TECHNIQUE	27
3.2.1	NON-CONTACT ACTIVE SCANNERS	27
3.2.2	NON-CONTACT PASSIVE SCANNERS	55
3.3	DATA PROCESSING OF 3D SCANS AND MODEL RECONSTRUCTION	66
4	CURRENT APPLICATIONS OF 3D SCANS IN CIVIL ENGINEERING	71
4.1	STRUCTURAL HEALTH MONITORING	71
4.2	CULTURAL HERITAGE – DIGITAL DOCUMENTATION, BIM, AND STRUCTURAL ANALYSIS	72
4.3	SCAN TO FEM	74
5	INITIAL GEOMETRIC IMPERFECTIONS OF STEEL ELEMENTS: METROLOGY AND NUMERICAL MODELLING	79
6	IMPERFECTION MEASUREMENTS OF STAINLESS-STEEL LINKS	85
6.1	GENERAL DESCRIPTION	85
6.2	EXPERIMENTAL SPECIMENS AND TEST SETUP	86
6.2.1	EXPERIMENTAL SETUP	86
6.2.2	CYCLIC LOADING PROTOCOL	87
6.2.3	TIGHTENING OF THE PRELOADED BOLTS	88
6.2.4	INSTRUMENTATION AND DATA ACQUISITION	89
6.2.5	EXPERIMENTAL DATA PROCESSING	91
6.3	GEOMETRIC DIMENSION AND IMPERFECTION MEASUREMENTS	93
6.3.1	TRADITIONAL GEOMETRIC DIMENSION MEASUREMENTS	93
6.3.2	3D SCANNING FOR DIMENSION AND IMPERFECTION MEASUREMENTS	95
6.3.3	RESULTS	112
6.4	POST-PROCESSING OF THE SCANNED DATA AND 3D MODELLING OF THE GEOMETRIC IMPERFECTIONS	115
6.4.1	MANUAL MESH GENERATION FROM POINT CLOUDS	116
6.4.2	GENERATING SOLID MODELS FROM 3D SURFACE MODELS	122
6.4.3	DEVIATION MEASUREMENT ANALYSIS	127
7	FINITE ELEMENT MODELLING OF THE GEOMETRIC IMPERFECTIONS	131
7.1	NUMERICAL MODEL	131
7.1.1	FE MODEL WITHOUT IMPERFECTIONS	131
7.1.2	FE MODEL WITH IMPERFECTIONS APPLIED AS BUCKLING MODES	133
7.1.3	FE MODEL WITH EQUIVALENT IMPERFECTIONS APPLIED AS PRESSURE LOAD	134

7.1.4	FE MODEL WITH MEASURED IMPERFECTIONS APPLIED AS PRESSURE LOAD	136
7.1.5	FE MODEL DEVELOPED FROM THE 3D SCAN.....	137
7.2	MODEL CALIBRATION.....	139
7.3	RESULTS.....	139
CONCLUSIONS	145
REFERENCES	147
APPENDIX A	153
APPENDIX B	155

LIST OF FIGURES

Figure 1 – Existing 3D Scanning technologies.....	23
Figure 2 – Different typologies of CMM’s	24
Figure 3 – The time-of-flight methods: pulsed modulation (top) and continuous- modulation (bottom) (Li, 2014).	28
Figure 4 – Extending distance using a multi-frequency technique (Jongenelen, et.al., 2011)	30
Figure 5 – Laser classes	33
Figure 6 – Static scanners (Trimble TX8 – left, Z+F IMAGER – right)	34
Figure 7 – Mobile scanner (Leica Pegasus Backpack)	34
Figure 8 – Hand-held scanner (Leica BLK2GO)	35
Figure 9 – UAV scanner (DJI Zenmuse)	35
Figure 10 – Smartphone scanner (Apple Inc.)	36
Figure 11 – LiDAR Rear Camera CIS (Apple Inc.)	37
Figure 12 – Michelson interferometer principle	39
Figure 13 – Principle of modern white - light interferometers	40
Figure 14 – TopMap Pro.Surf (Polytec Interferometer)	40
Figure 15 – Structured light scanner principle.....	41
Figure 16 – Traditional white light scanner (HP PRO S3)	42
Figure 17 – Wavelength of different colours	42
Figure 18 – Example of pseudorandom structured pattern	44
Figure 19 – Example of binary encoded pattern	45
Figure 20 – Example of n-ary encoded pattern and its cross-section	45
Figure 21 – Example of triangular phase encoded pattern and its cross-section	46
Figure 22 – Example of trapezoidal phase encoded pattern and its cross-section	46
Figure 23 – Example of sinusoidal phase encoded pattern and its cross-section.....	47
Figure 24 – Example of static blue light scanner (Hexagon Stereo scanner).....	48
Figure 25 – Example of automated blue light scanner (Capture 3D - ATOS 5)	48
Figure 26 – Example of handheld white light scanners (left – Creafom Go! SCAN3D, right – Artec 3D Leo).....	49
Figure 27 – Triangulation principle.....	51
Figure 28 – Triangulation principle – multi-camera solution.....	52
Figure 29 – Laser scanners with measuring arms (left – Hexagon Absolute arm, right – Nikon Model Maker H120)	53
Figure 30 – Hand-held laser scanners (left – Creafom Handyscan 3D, right – ZG Scan 717).....	54

Figure 31 – Aerial photogrammetry principle of overlapping.....	57
Figure 32 – Aerial photogrammetry methods of data acquisition : a) satellite (Sentinell 1 – European Space Agency); b) drone (DJI Phantom); c) commercial aircraft.....	57
Figure 33 – Close-range photogrammetry approaches	58
Figure 34 – Data exchange in a photogrammetric measurement	59
Figure 35 – Nikon D6 based on CMOS technology	61
Figure 36 – DSLR cameras in small and medium format vs Smartphone camera.....	61
Figure 37 – DPA Industrial photogrammetry camera (Hexagon)	62
Figure 38 – Arago automated photogrammetry (Rigsters).....	62
Figure 39 – Schematics depicting the recommended orientation of the cameras in a stereovision system	64
Figure 40 – Three-different-speckle-patterns used for DIC.....	65
Figure 41 – VIC 3D (Correlated solutions).....	65
Figure 42 – Point cloud obtained from a scanned cube	67
Figure 43 – Delaunay triangulation method	68
Figure 44 – Marching cubes algorithm.....	69
Figure 45 – Comparison between NURBS (left) and T-splines (right)	69
Figure 46 – Example of a solid model.....	70
Figure 47 – Photogrammetric data processing workflow	70
Figure 48 – Global sway imperfections.....	79
Figure 49 – Local imperfection assessment for columns (EN 1993-1-1)	80
Figure 50 – Local imperfection assessment for beams (EN 1993-1-1).....	80
Figure 51 – Equivalent imperfections for lateral torsional buckling	82
Figure 52 – Equivalent imperfections for cross-sections of plated structures	83
Figure 53 – Cyclic loading protocol for replaceable links	87
Figure 54 – Cyclic loading protocol for replaceable links	88
Figure 55 – Combined tightening method parameters, acc. to EN 1090-2:2008	89
Figure 56 – Instrumentation of the experimental setup.....	90
Figure 57 – Local displacement transducers layout on the link.....	90
Figure 58 – VIC system setup.....	91
Figure 59 – Geometry of the test setup	92
Figure 60 – Tools used for manual geometric dimension measurements.....	93
Figure 61 – Measured dimensions of the specimens.....	93
Figure 62 – 3D Measurements with the Absolute Arm.....	97
Figure 63 – Positioning of the laser probe for scanning the edges	98
Figure 64 – Post-processing software and real-time display of the specimen (Inspire)	98

Figure 65 – Schematic representation of the EinScan Pro HD set-up	99
Figure 66 – Calibration of the structured light scanner	100
Figure 67 – Scanning process with structured light	101
Figure 68 – Positioning of the structured light scanner towards the specimen	101
Figure 69 – Post-processing software and real-time display of the specimen (Solid Edge)	102
Figure 70 – Re-usable targets for multiple scans.....	103
Figure 71 – Changed position of the specimen for a more complete scan	104
Figure 72 – Setting the resolution level (left) and calibration (right) of the LiDAR scanner.....	105
Figure 73 – Positioning of the targets for the LiDAR scanning.....	106
Figure 74 – General view of the LiDAR measurement set-up (a)	106
Figure 75 – General view of the LiDAR measurement set-up (b)	107
Figure 76 – Scan alignment precisions	107
Figure 77 – Polycam – 3D scanning app	108
Figure 78 – Smartphone LiDAR measurement set-up	109
Figure 79 – Point cloud crop and final result in Polycam	110
Figure 80 – Incomplete point cloud due to reflective surfaces of the specimens	111
Figure 81 – Workflow of obtaining solid models from point clouds	115
Figure 82 – Imported point cloud of the laboratory building	117
Figure 83 – Imported point cloud before proper alignment	117
Figure 84 – Identifying the measured specimen	118
Figure 85 – Point cloud segmentation	118
Figure 85 – Merging the six point clouds	119
Figure 86 – The final cleaned and coloured point cloud.....	119
Figure 87 – Computing normals on the point cloud	120
Figure 88 – Poisson surface reconstruction.....	120
Figure 89 – Obtained mesh model from the point cloud	121
Figure 90 – Geometry from mesh plug-in in Abaqus	121
Figure 91 – Abaqus error during conversion from mesh to geometry	122
Figure 92 – Close Holes tool in Autodesk Fusion 360	123
Figure 93 – Removing degenerated faces.....	124
Figure 94 – Wrap tool used for deleting all inner structures.....	124
Figure 95 – Rebuild mesh body function.....	125
Figure 96 – Scaled and repaired model	125
Figure 97 – Face count reduction	126
Figure 98 – Automated mesh to solid conversion	126

Figure 99 – Final 3D solid model with virtual topology (black lines).....	127
Figure 100 – Overlaying the point cloud with the CAD model.....	128
Figure 101 – Colorised map of the dimension deviation	128
Figure 102 – Geometric dimension comparison in a section cut.....	129
Figure 103 – Shape of the geometric imperfections of the flanges	129
Figure 104 – Welding angle deviation measurement.....	130
Figure 105 – Deviation measurement between two different scans.....	130
Figure 106 – Numerical model of the link and experimental rig	132
Figure 107 – Diagonal connectors DT1 and DT2 for rotation monitoring.....	133
Figure 108 – Magnitude used for the equivalent geometric imperfections.....	133
Figure 109 – The 4th eigenvalue buckling mode of the link and procedure for importing geometric imperfections obtained in buckling analysis step.....	134
Figure 110 – The model reproducing imperfections by applying pressure on the link components and procedure for importing geometric imperfections obtained in imperfection analysis step	136
Figure 111 – Imperfection reference points on the link web and flange	136
Figure 112 – Combining virtual topology.....	138
Figure 113 – The FE mesh of the model.....	138
Figure 114 – Comparison of post-test deformed link and the plastic strain distribution of the numerical model at the corresponding rotation	139
Figure 115 – Numerical vs. experimental response curves of the calibrated model	139
Figure 116 – Link shear force – rotation diagram for investigated link models	143
Figure 117 – Plastic strain distribution of the numerical model and buckling of the web of experimental specimen.....	144

LIST OF TABLES

Table 1 – Comparison between different Lidar scanners.....	38
Table 2 – Comparison between different structured light scanners	50
Table 3 – Comparison between different laser scanners.....	55
Table 4 – Comparison between different photogrammetric instruments.....	63
Table 6 – Nomenclature of the links tested in the experimental program	86
Table 7 – Dimensions of specimen S-C.....	94
Table 8 – Dimensions of specimen S-2DS-C1.....	94
Table 9 – Dimensions of specimen S-2DS-C2.....	95
Table 10 – Applied scanners / Specimen.....	95
Table 11 – Technical specifications of the used scanners	96
Table 12 – Comparison between the five scanner systems.....	112
Table 13 – Comparison between manual measurements and 3D scans of specimen S-C	113
Table 14 – Comparison between measurements of specimen S-C (continuation)	113
Table 15 – Comparison between measurements of specimen S-2DS-C1.....	113
Table 16 – Comparison between measurements of specimen S-2DS-C1 (continuation)	114
Table 17 – Comparison between measurements of specimen S-2DS-C2.....	114
Table 18 – Comparison between measurements of specimen S-2DS-C2 (continuation)	114
Table 19 – Post-processing capabilities of the software that comes with each scanner	116
Table 20 – Applied code-based pressure loads on link	134
Table 21 – Resulted imperfection values for the link flanges.....	135
Table 22 – Resulted imperfection values for the link web.....	135
Table 23 – Imperfection value calculation for link web and flanges	137
Table 24 – Results obtained for link rotation equal to 0.15 rad	141
Table 25 – Results obtained for link rotation equal to 0.30 rad	142

1 INTRODUCTION

A digital twin, also called data twin, can be described as a digital representation of a real-world object. Digital twins have many applications outside the built environment, and are used in the automotive, healthcare, systems engineering, and aerospace industries. In the context of the construction industry, a "digital twin" refers to a digitalized replica that represents an exact virtual representation of a construction project or asset. An asset can take many forms such as a building, a cluster of buildings, a bridge, a roadway, a city block, or even an entire city. Digital twins, in the realm of construction industry, can be referred to as data twins, virtual models, or even the successors of as-built drawings. The production of digital twins involves the collection and combining real-world information about the building or structure using advanced technologies such as 3D scanners, unmanned aerial vehicles, sensing devices and imaging tools. The use of digital twins in the construction industry presents a crucial advantage, as it facilitates the enhancement of analytical capacities associated with the implementation of building information modelling (BIM). The incorporation of digital twin technology into building information modelling (BIM) models introduces an enhanced level of capability, allowing key stakeholders to visually represent the current state, functional parameters, and spatial location of tangible assets in real time. Digital twin technology is also growing interest among researchers, because of its practical purposes, such as simulation, testing, or monitoring the effectively indistinguishable digital counterpart of a structure or parts of a structure.

Reverse engineering on the other hand, is defined as a process in which structures, or objects are deconstructed to extract exact design information from them and enables the recreation of it.

The two processes mentioned above have in common one important step, the geometric data acquisition type: 3D scanning. There are nowadays several different 3D scanning systems that fit into a wide range of applications. It was mandatory to compare these systems in the following chapter and evaluate the advantages and disadvantages for each of them, aiming to select the best fitting technologies for a newly proposed use: creating 3D models of structures or parts of structures for numerical analysis that consider the real geometric imperfections.

The finite element analysis (FEA) is used in many fields including here also civil engineering for numerically approximating physical structures that are too complex for regular analytical solutions. It is a result of its excellent accuracy of approximation and its comprehensive compatibility with different geometries of structures when analytical solutions cannot be obtained.

Referring to the field of steel construction, initial geometric imperfections are found to be one of the most unfavourable factors in the design, numerical analysis and construction of steel elements and structures, which may lead to their reduced strength and stability. Such imperfection is almost inevitable and may occur in the manufacture, transportation, and installation of steel members. Structural engineers can consider the material and geometric imperfections in the steel design according to EN 1993-1-1 (EN

1993-1-1: Design of steel structures - Part 1-1: General rules and rules for buildings). These imperfections are modelled by means of additional equivalent static loads or deformed shape (global sway imperfections or local bow imperfections) that simulate the effect of possible imperfections. The effects of the initial geometric imperfections on the stability performance of steel members have been also recently investigated by many researchers using the numerical method. (Feng,et. al., 2019). Finite element modelling considering also initial geometric imperfection enhances the accuracy and reliability of the numerical results (Xu, et. al., 2023).

The traditional modelling method that is available in the current codes only considers the amplitude of imperfection, which may lead to unreliable results. A novel method and modelling technique for obtaining the real initial geometric imperfection of steel members was proposed in this thesis. Different types of 3D scanners were employed to generate 3D point-cloud models, and a workflow of data processing was developed to convert the 3D point-cloud model to actual digital geometric model. After that, such geometric models can be directly imported into general FE software (Abaqus).

In the past, imperfection measurements were generally carried out with contact instruments, such as a dial gauge, and dimensions were manually measured with callipers and micrometres. These modes of measurement can only provide a sparse representation of the actual imperfect geometry. Existing imperfection measurements do not capture the full three-dimensional imperfect geometry, but current capabilities in 3D scanning provide viable candidates for full-field non-contact measurement.

2 3D SCANNING FUNDAMENTALS

2.1 GENERAL INFORMATION

Metrology is defined by the International Bureau of Weights and Measures (BIPM) as **"the science of measurement"**. The 3D scanning technology is widely used in metrology to analyse a real-world object or environment to collect data on its shape and possibly its appearance (i.e., colour). The collected data can then be used to construct digital three-dimensional models.

The first 3D scanning technology was created in the 1960s. The early scanners used lights, cameras, and projectors to perform this task. Due to limitations of the equipment, it often took a lot of time and effort to scan objects accurately. After 1985 they were replaced with scanners that could use white light, lasers, and shadowing to capture a given surface. Many different technologies can be used to build these 3D scanning devices; each technology comes with its own limitations, advantages, and costs. Many limitations in the kind of objects that can be digitized are still present: for example, optical technologies encounter many difficulties with shiny, mirroring, or transparent objects. There are several different kinds of 3D scanners, with prices ranging from the couple thousands to the hundreds of thousands. Collected 3D data is useful for a wide variety of applications. The purpose of a 3D scanner is usually to create a 3D model. This 3D model consists of a polygon mesh or point cloud of geometric samples on the surface of the subject. These points can then be used to extrapolate the shape of the subject (a process called reconstruction). If colour information is collected at each point, then the colours or textures on the surface of the subject can also be determined. These devices are used extensively by the entertainment industry in the production of movies and video games. Other common applications of this technology include industrial design, orthotics and prosthetics, reverse engineering and prototyping, quality control/inspection and documentation of cultural artifacts. The 3D Laser Scanning market including hardware, software, and services is rather dynamic with major segments experiencing rapid product innovation. The market contains exceptional opportunities with rapid forecasted growth driven by both replacing older mechanical methods, and by improved workflow with lower overall project costs, which enables more projects (Ebrahim 2011).

In some situations, a single scan will not produce a complete model of the subject. Multiple scans, from different directions, are usually helpful to obtain information about all sides of the subject. These scans have to be brought into a common reference system, a process that is usually called alignment or registration, and then merged to create a complete 3D model. This whole process, going from the single range map to the whole model, is usually known as the 3D scanning pipeline (Bernardini and Rushmeier, 2002).

2.2 HISTORY OF 3D SCANNING

Starting with Galileo Galilei, who devised in 1638 an experiment that seemed able to show that the velocity of light is finite (Foschi and Leone, 2009), over the course of history, metrology went through several evolutions. Worth of mentioning is the introduction of the **metric system** in 1795 by the French government, now known as the International System of Units. One meter was preliminary defined as one ten millionth of the distance between the North Pole and the Equator crossing through Paris. Of course, the meter definition has evolved over the centuries, but is still considered today as the length reference to which every measuring tool refers. Next is a brief history of the 3D scanning development (Site 1) (Site 2).

The first use of **photogrammetry** appears shortly after the emergence of photography in 1840. The credit goes to French geodesist, François Arago. He presented to the Academy of Science this technology that enabled him to determine the position of objects in space based on photographs taken from different viewing angles, without knowing the position of the shots beforehand. Nowadays Photogrammetry is widely used in fields such as topographic mapping, architecture, engineering, manufacturing, quality control, police investigations, cultural heritage, and geology. A somewhat new application is the scanning of objects to automatically make 3D models of them. Since photogrammetry relies on images, there are physical limitations when those images are of an object that has strong reflective or dark surfaces.

American Physicist Albert A. Michelson thought detection of motion through ether might be measurable. To do so, he invented in 1887 a new instrument called the **interferometer**. Interferometers evolved in time and are using in present the interference of superimposed waves to extract information. Interferometry is an important investigative technique in the fields of astronomy, fiber optics, engineering metrology, optical metrology, oceanography, seismology, spectroscopy (and its applications to chemistry), quantum mechanics, nuclear and particle physics, plasma physics, remote sensing, biomolecular interactions, surface profiling, microfluidics, mechanical stress/strain measurement, velocimetry, optometry, and making holograms.

Speaking of contact 3D scanning technologies, the first **Coordinate Measuring Machine** appeared in the early 60s and was made of 3D tracing devices with a simple digital readout (DRO) displaying the XYZ position. The initial CMM was developed by the Ferranti Company in Scotland during the 50s. This unit, however, had only two axis. The very first three-axis prototypes arrive during the 1960s and are invented by the Italian company DEA (now part of the Hexagon Metrology Group). Soon afterwards, automated CMMs appeared in the 60s to perform complex inspections of Concorde supersonic jet engines.

Portable CMMs with **measuring arms** arrive in the 80s, revolutionizing the measurement process: it is now possible to bring **metrology tools** to the production industry. This innovation eliminates the need to move manufactured parts to a dedicated, controlled environment. However, because measuring arms use a classic technology

based solely on precision mechanical parts, these portable CMMs remain very sensitive to vibrations and instabilities induced by the environment. Therefore, considerable precautions are required when operating them.

Although the first **3D scanners** were developed in the 60s, it is not until 1985 that the **laser technology** is applied to **3D scanning**. Prior, the 3D scanning models used lights, cameras, and projectors to perform a scan. However, a lot of time and effort was required to scan objects accurately. Scanners built after 1985 use white/blue light, lasers, and shadowing to capture a given surface.

Since 1994, a new airborne terrain modelling technology has been available to the surveying industry. The term "Airborne Laser Scanner" (ALS) evolved as the hardware utilized in the aircraft is a logical advancement of the Airborne Laser Profilers used primarily by the forestry industry for many years. Other titles attributed to the same piece of hardware include "**LiDAR**" (the term favoured in the United States), and "Airborne Laser Terrain Mapper (ALTM)", the brand name used by the major hardware manufacturer in this field. Terrestrial laser scanning has already found its place between the standard technologies for objects acquisition. The laser scanner can be described as a motorized total station, which automatically measures all the points in its horizontal and vertical field. For each measured point, its distance to the laser scanner together with the horizontal and the vertical angles are recorded. So, the space coordinates relative to the scanner position can be easily computed (Abdelhafez, 2009). 3D laser scanning developed during the last half of the 20th century in an attempt to accurately recreate the surfaces of various objects and places. The technology is especially helpful in fields of research and design.

In 1996, 3D Scanners took the key technologies of a **manually operated arm** and a **stripe 3D scanner** - and combined them in ModelMaker. This flexible system is the world's first Reality Capture System. It produces complex models, and it textures those models with colour. Coloured 3D models were now produced in minutes.

3 OVERVIEW OF 3D SCANNING TECHNOLOGIES

There are a variety of technologies for digitally acquiring the shape of a 3D object. The techniques work with most or all sensor types including optical, acoustic, laser scanning, radar, thermal, and seismic. A well-established classification (Curless,2000) divides them into two types: contact and non-contact. Non-contact solutions can be further divided into two main categories, active and passive. There are a variety of typologies that fall under each of these categories (Figure 1).

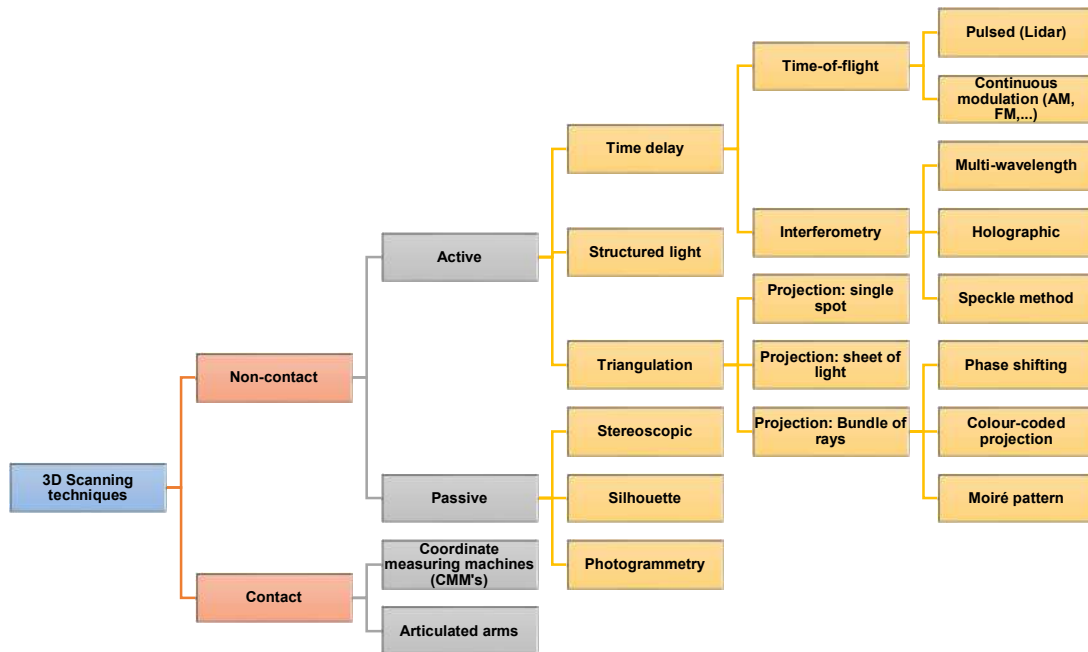


Figure 1 – Existing 3D Scanning technologies

3.1 CONTACT TECHNIQUE

3D contact scanners, generally calibrated to operate on a fixed platform, often contain a probe located at the end of an articulated mechanical arm. The arm may be robotically or manually manipulated over the part's surface. As the probe contacts the object's surface the scanner records the X, Y,Z position of the probe by taking positional measurements of the armature. The recorded positions form a point cloud, which can be used to calculate a 3D mesh. Some highly accurate 3D scanners called Coordinate Measuring Machines (CMMs) (Figure 2) are often used by the manufacturing industry to inspect parts for early indications of assembly problems. 3D contact scanners suffer from slow scan rates and may not be ideal for delicate objects, such as precious artworks, as physical contact may damage or deform the surface [Site 3].



Figure 2 – Different typologies of CMM's

3.1.1 TRADITIONAL COORDINATION MEASURING MACHINE (CMM)

Contact 3D scanners probe the subject through physical touch. A CMM (Coordinate Measuring Machine) is an example of a contact 3D scanner. A coordinate measuring machine (CMM) is a device for measuring the physical geometrical characteristics of an object. This machine may be manually controlled by an operator, or it may be computer controlled. Measurements are defined by a probe attached to the third moving axis of this machine. Probes may be mechanical, optical, laser, or white/blue light, amongst others.

It is used mostly in manufacturing and can be very precise. The disadvantage of CMMs though, is that they require contact with the object being scanned. Thus, the act of scanning the object might modify or damage it. This fact is very significant when scanning delicate or valuable objects such as historical artifacts. The other disadvantage of CMMs is that they are relatively slow compared to the other scanning methods. Physically moving the arm that the probe is mounted on can be very slow and the fastest CMMs can only operate at a few hundred hertz. In contrast, an optical system like a laser scanner can operate from 10 to 500 kHz. Other examples are the hand driven touch probes used to digitize clay models in the computer animation industry. The typical CMM is composed of three axes, an X, Y, and Z. These axes are orthogonal to each other in a typical three-dimensional coordinate system. Each axis has a scale system that indicates the location of that axis. The machine will read the input from the touch probe, as directed by the operator or programmer. The machine then uses the X,Y, Z coordinates of each of these points to determine size and position with micrometre precision typically. Coordinate measuring machines include three main components [Site 4]:

- The main structure which includes three axes of motion;
- Probing system;
- Data collection and reduction system - typically includes a machine controller, desktop computer, and application software.

They are often used for:

- Dimensional measurement;

- Profile measurement;
- Angularity or orientation measurement;
- Depth mapping;
- Digitizing or imaging;
- Shaft measurement.

They are offered with features like:

- Crash protection;
- Offline programming;
- Reverse engineering;
- CAD Model import capability.

The machines are available in a wide range of sizes and designs with a variety of different probe technologies. They can be operated manually or automatically through Direct Computer Control (DCC). They are offered in various configurations such as benchtop, freestanding, handheld, and portable. Specific parts of a CMM are:

a) Machine body

In modern machines, the gantry type superstructure has two legs and is often called a bridge. This moves freely along the granite table with one leg (often referred to as the inside leg) following a guide rail attached to one side of the granite table. The opposite leg (often outside leg) simply rests on the granite table following the vertical surface contour. Air bearings are the chosen method for ensuring friction free travel. In these, compressed air is forced through a series of very small holes in a flat bearing surface to provide a smooth but controlled air cushion on which the CMM can move in a frictionless manner. The movement of the bridge or gantry along the granite table forms one axis of the XY plane. The bridge of the gantry contains a carriage which traverses between the inside and outside legs and forms the other X or Y horizontal axis. The third axis of movement (Z axis) is provided by the addition of a vertical quill or spindle which moves up and down through the center of the carriage. The touch probe forms the sensing device on the end of the quill. The movement of the X, Y and Z axes fully describes the measuring envelope. Optional rotary tables can be used to enhance the approachability of the measuring probe to complicated workpieces. The rotary table as a fourth drive axis does not enhance the measuring dimensions, which remain 3D, but it does provide a degree of flexibility. Some touch probes are themselves powered rotary devices with the probe tip able to swivel vertically through 90 degrees and through a full 360-degree rotation. As well as the traditional three axis machines, CMMs are now also available in a variety of other forms. These include CMM arms that use angular measurements taken at the joints of the arm to calculate the position of the stylus tip. Such arm CMMs are often used where their portability is an advantage over traditional fixed bed CMMs. Because CMM arms imitate the flexibility of a human arm they are also often able to reach the insides of complex parts that could not be probed using a standard three axis machine.

b) Mechanical probe

In the early days of coordinate measurement mechanical probes were fitted into a special holder on the end of the quill. A very common probe was made by soldering a hard ball to the end of a shaft. This was ideal for measuring a whole range of flat, cylindrical, or spherical surfaces. Other probes were ground to specific shapes, for example a quadrant, to enable measurement of special features. These probes were physically held against the workpiece with the position in space being read from a 3-Axis digital readout (DRO) or, in more advanced systems, being logged into a computer by means of a footswitch or similar device. Measurements taken by this contact method were often unreliable as machines were moved by hand and each machine operator applied different amounts of pressure on the probe or adopted differing techniques for the measurement. A further development was the addition of motors for driving each axis. Operators no longer had to physically touch the machine but could drive each axis using a hand box with joysticks in much the same way as with modern remote-controlled cars. Measurement accuracy and precision improved dramatically with the invention of the electronic touch trigger probe. The pioneer of this new probe device was David McMurtry who subsequently formed what is now Renishaw plc. Although still a contact device, the probe had a spring-loaded steel ball (later ruby ball) stylus. As the probe touched the surface of the component the stylus deflected and simultaneously sent the X,Y, Z coordinate information to the computer. Measurement errors caused by individual operators became fewer and the stage was set for the introduction of CNC operations and the coming of age of CMMs. Optical probes are lens-CCD-systems, which are moved like mechanical ones, and are aimed at the point of interest, instead of touching the material. The captured image of the surface will be enclosed in the borders of a measuring window, until the residue is adequate to contrast between black and white zones. The dividing curve can be calculated to a point, which is the wanted measuring point in space. The horizontal information on the CCD is 2D (XY) and the vertical position is the position of the complete probing system on the stand Z-drive (or another device component). This allows entire 3D-probing.

There are newer models that have probes that drag along the surface of the part taking points at specified intervals, known as scanning probes. This method of CMM inspection is often more accurate than the conventional touch-probe method and most times faster as well. The next generation of scanning, known as non-contact scanning, includes high speed laser single point triangulation [Site 5], laser line scanning [Site 6], and white light scanning [Site 7], is advancing very quickly. This method uses either laser beams or white light that are projected against the surface of the part. Many thousands of points can then be taken and used to not only check size and position, but to create a 3D image of the part as well. This "point-cloud data" can then be transferred to CAD software to create a working 3D model of the part. These optical scanners are often used on soft or delicate parts or to facilitate reverse engineering.

3.1.2 PORTABLE COORDINATE MEASURING MACHINES

Portable CMMs are different from "traditional CMMs" in that they most commonly take the form of an articulated arm. These arms have six or seven rotary axes with rotary encoders, instead of linear axes. Portable arms are lightweight (typically less than 20 pounds) and can be carried and used nearly anywhere. The inherent trade-offs of a portable CMM are manual operation (always requires a human to use it), and overall accuracy is somewhat too much less accurate than a bridge type CMM. Certain non-repetitive applications such as reverse engineering, rapid prototyping, and large-scale inspection of low-volume parts are ideally suited for portable CMMs. Traditional CMM technology using touch probes is today often combined with other measurement technology. This includes laser, video, or white light sensors to provide what is known as multi-sensor measurement [Site 8].

3.2 NON-CONTACT TECHNIQUE

Non-contact 3D scanners, as the name implies, do not make physical contact with an object or surface. Instead, noncontact 3D scanners rely on some active or passive techniques to scan an object. The final result is a highly accurate cloud of points that can be used for reverse engineering, virtual assembly, engineering analysis, feature and surface inspection or rapid prototyping [Site 5].

3.2.1 NON-CONTACT ACTIVE SCANNERS

Active scanners emit some kind of radiation or light and detect its reflection in order to probe an object or environment. Possible types of emissions used include light, ultrasound, or x-ray [Site 9]. Active 3D Scanning can generally be categorized into three main methods: **triangulation**, **time-delay**, and **structured light**.

Time-delay techniques can be further divided into two categories: **time-of flight** and **interferometry**.

3.2.1.1 Time-delay technique

3.2.1.1.1 Time-of-flight

Time-of-flight is an active 3D scanning technique that uses **laser** light to probe the subject. At the heart of this type of scanning is a time-of-flight laser rangefinder. A 3D time-of-flight (TOF) camera works by illuminating the scene with a modulated light source and observing the reflected light. The phase shift between the illumination and the reflection is measured and translated to distance. Typically, the illumination is from a solid-state laser or a LED operating in the near-infrared range (~850nm) invisible to the human eyes. An imaging sensor designed to respond to the same spectrum receives the light and converts the photonic energy to electrical current. Note that the light entering the sensor has an ambient component and a reflected component. Distance (depth) information is

only embedded in the reflected component. Therefore, high ambient component reduces the **signal to noise ratio (SNR)**.

To detect phase shifts between the illumination and the reflection, the light source is **pulsed** or **modulated** by a **continuous wave (CW)**, source, typically a sinusoid or square wave. Square wave modulation is more common because it can be easily realized using digital circuits (Hansard, et. al., 2012). Pulsed modulation can be achieved by integrating photoelectrons from the reflected light, or by starting a fast counter at the first detection of the reflection. The latter requires a fast photodetector, usually a single-photon avalanche diode (SPAD). This counting approach necessitates fast electronics, since achieving 1 millimetre accuracy requires timing a pulse of 6.6 picoseconds in duration. This level of accuracy is nearly impossible to achieve in silicon at room temperature (Charbon, et. al., 2013).

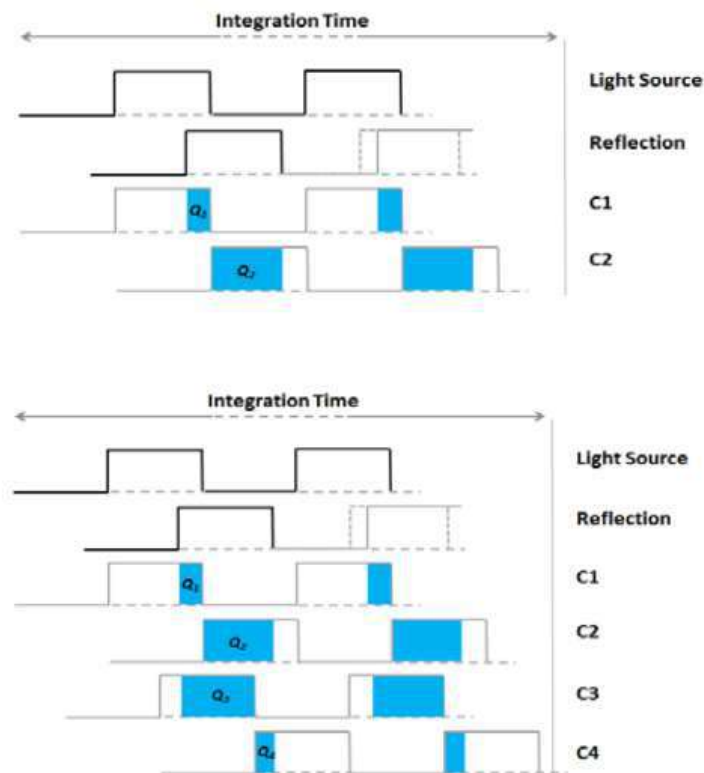


Figure 3 – The time-of-flight methods: pulsed modulation (top) and continuous-modulation (bottom) (Li, 2014).

The pulsed method is straightforward. The light source illuminates for a brief period (Δt), and the reflected energy is sampled at every pixel, in parallel, using two out-of-phase windows, C1 and C2, with the same Δt . Electrical charges accumulated during these samples, Q1 and Q2, are measured and used to compute distance using the formula:

$$d = \frac{1}{2} \times c \times \Delta_t \times \left(\frac{Q_2}{Q_1 + Q_2} \right) \quad (1)$$

In contrast, the CW method takes multiple samples per measurement, with each sample phase-stepped by 90 degrees, for a total of four samples. Using this technique, the phase angle between illumination and reflection, φ , and the distance, d , can be calculated by

$$\varphi = \arctan\left(\frac{Q_3 - Q_4}{Q_1 - Q_2}\right) \quad (2)$$

$$d = \frac{c}{4\pi} \times \varphi \quad (3)$$

It follows that the measured pixel intensity (A) and offset (B) can be computed by:

$$A = \frac{\sqrt{(Q_1 - Q_2)^2 + (Q_3 - Q_4)^2}}{2} \quad (4)$$

$$B = \frac{Q_1 + Q_2 + Q_3 + Q_4}{4} \quad (5)$$

In all of the equations, c is the speed-of-light constant (299,792,458 m/s). The complexity of the CW method, as compared to the pulsed method, may seem unjustified, but a closer look at the CW equations reveals that the terms, $(Q_3 - Q_4)$ and $(Q_1 - Q_2)$ reduces the effect of constant offset from the measurements. Furthermore, the quotient in the phase equation reduces the effects of constant gains from the distance measurements, such as system amplification and attenuation, or the reflected intensity. These are desirable properties. The reflected amplitude (A) and offset (B) do have an impact on the depth measurement accuracy. The depth measurement variance can be approximated by:

$$\sigma = \frac{c}{4 \times \sqrt{2} \times \pi \times f} \times \frac{\sqrt{A+B}}{c_d \times A} \quad (6)$$

The modulation contrast, c_d , describes how well the TOF sensor separates and collects the photoelectrons. The reflected amplitude, A , is a function of the optical power. The offset, B , is a function of the ambient light and residual system offset. One may infer from Equation 6 that high amplitude, high modulation frequency and high modulation contrast will increase accuracy; while high offset can lead to saturation and reduce accuracy. At high frequency, the modulation contrast can begin to attenuate due to the physical property of the silicon. This puts a practical upper limit on the modulation frequency. TOF sensors with high roll off frequency generally can deliver higher accuracy.

The fact that the CW measurement is based on phase, which wraps around every 2π , means the distance will also have an aliasing distance. The distance where aliasing occurs is called the ambiguity distance, d_{amb} , and is defined as:

$$d_{amb} = \frac{c}{2 \times f} \quad (7)$$

Since the distance wraps, d_{amb} is also the maximum measurable distance. If one wishes to extend the measurable distance, one may reduce the modulation frequency, but at the cost of reduced accuracy, as according to Equation 6. Instead of accepting this compromise, advanced TOF systems deploy multi-frequency techniques to extend the distance without reducing the modulation frequency. Multi-frequency techniques work by adding one or more modulation frequencies to the mix. Each modulation frequency will

have a different ambiguity distance, but true location is the one where the different frequencies agree. The frequency of when the two modulations agree, called the beat frequency, is usually lower, and corresponds to a much longer ambiguity distance. The dual-frequency concept is illustrated below.

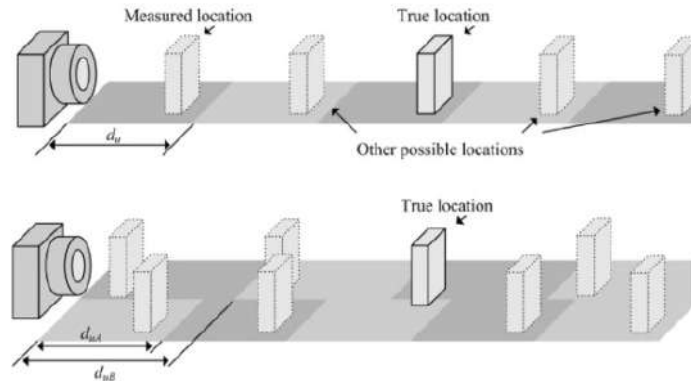


Figure 4 – Extending distance using a multi-frequency technique (Jongenelen, et.al., 2011)

The accuracy of a time-of-flight 3D laser scanner depends on how precisely we can measure the time (t): 3.3 picoseconds (approx.) is the time taken for light to travel 1 millimetre. The laser rangefinder only detects the distance of one point in its direction of view. Thus, the scanner scans its entire field of view one point at a time by changing the range finder's direction of view to scan different points. The view direction of the laser rangefinder can be changed either by rotating the range finder itself, or by using a system of rotating mirrors. The latter method is commonly used because mirrors are much lighter and can thus be rotated much faster and with greater accuracy. Typical time-of-flight 3D laser scanners can measure the distance of 10,000~100,000 points every second. From this category of 3D scanning technologies is worth mentioning the well-established **LIDAR method (pulsed modulation)**.

LIDAR is a laser technology that captures the surfaces of an object or a space in three dimensions. The word "lidar" is an acronym for **L**ight **D**etection **A**nd **R**anging. LiDAR technology has application in geomatics, archaeology, geography, geomorphology, seismology, forestry, remote sensing, and atmospheric physics (Cracknell, et al, 2007), as well as in airborne laser swath mapping (ALSM), laser altimetry and LiDAR Contour Mapping. LiDAR uses the same principle as RADAR. Just transmitting a beam of light to a target (the ground) and measuring the time it takes for the beam to echo back and calculating Range from the result. LiDAR differs from RADAR mainly in its ability to resolve very small targets and penetrate vegetation. The acronym LADAR (Laser Detection And Ranging) is often used in military contexts. The term "laser radar" is sometimes used even though LiDAR does not employ microwaves or radio waves and is not therefore radar even though both systems employ electromagnetic radiation.

The introduction of the LiDAR principle dates back to pre-laser times. In the 1930s first attempts were made to measure air density profiles in the upper atmosphere by

determining the scattering intensity from searchlight beams. Height information was obtained by scanning the receiver field of view of a distant telescope along the continuous light beam. In 1938, pulses of light were used for the first time to measure cloud base heights. The generation of light pulses by electric sparks and flashlamps allowed the replacement of the bistatic configuration by a monostatic setup, i.e., a setup in which transmitter and receiver are collocated and the height information is actively deduced from a measurement of the round-trip time between pulse emission and signal detection. Ever since, success in Lidar development has been strongly connected with progress in optical and electronic technology (Wandinger, 2005).

In recent years, light detection and ranging (LiDAR) technology has gained huge popularity in various applications such as navigation, robotics, remote sensing, and advanced driving assistance systems (ADAS). This popularity is mainly due to the improvements in LiDAR performance in terms of range detection, accuracy, power consumption, as well as physical features such as dimension and weight. Several literatures on LiDAR technology have been highlighting four commonly used mechanisms in LiDAR systems: Opto-mechanical, electromechanical, micro-electromechanical systems (MEMS), and solid-state scanning. The studies revealed that electro-mechanical scanning is the most prominent technology in use today. The commercially available 1D time of flight (TOF) LiDAR instrument is currently the most attractive option for conversion from 1D to 3D LiDAR system, provided that low scanning rate is not an issue. As for applications with low size, weight, and power (SWaP) requirements, MEMS scanning is found to be the better alternative. Finally, solid-state LiDAR systems are expected to fill in the gap in ADAS applications despite the low technology readiness in comparison to MEMS scanners. However, since solid-state scanning is believed to have superior robustness, field of view (FOV), and scanning rate potential, great efforts are given by both academics and industries to further develop this technology. (Raj et. al., 2020).

LiDAR uses ultraviolet, visible, or near infrared light to image objects and can be used with a wide range of targets, including non-metallic objects, rocks, rain, chemical compounds, aerosols, clouds, and even single molecules (Cracknell, et al, 2007). A narrow laser beam can be used to map physical features with very high resolution (0.1 mm). Wavelengths in a range from about 10 micrometres to the UV (ca. 250 nm) are used to suit the target. Typically, light is reflected via backscattering. Based on different kinds of backscattering, the LiDAR can be accordingly called Rayleigh LiDAR, Mie LiDAR, Raman LiDAR, and Na/Fe/K Fluorescence LiDAR and so on (Cracknell, et al, 2007).

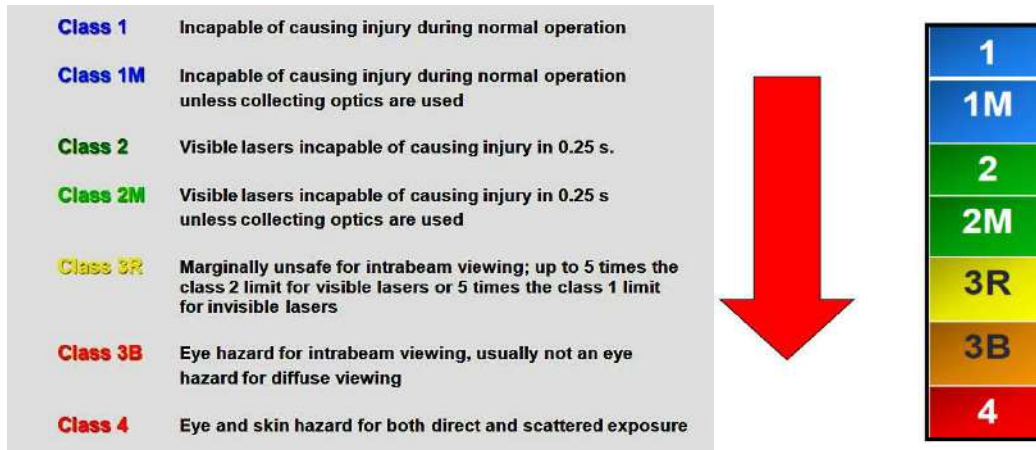
In terms of design, a basic LiDAR system involves a laser range finder reflected by a rotating mirror (top). The laser is scanned around the scene being digitised, in one or two dimensions (middle), gathering distance measurements at specified angle intervals (bottom). In general, there are two kinds of LiDAR detection schema: **"incoherent"** or **direct energy detection** (which is principally an amplitude measurement) and **coherent detection** (which is best for Doppler, or phase sensitive measurements). Coherent systems generally use optical heterodyne detection which being more sensitive than direct detection allows them to operate a much lower power but at the expense of more complex

transceiver requirements [Site 10]. In both coherent and incoherent LiDAR, there are two types of pulse models: micro pulse LiDAR systems and high-energy systems. Micro pulse systems have developed as a result of the ever increasing amount of computer power available combined with advances in laser technology. They use considerably less energy in the laser, typically about one microjoule, and are often "eye-safe," meaning they can be used without safety precautions. High-power systems are common in atmospheric research, where they are widely used for measuring many atmospheric parameters: the height, layering and densities of clouds, cloud particle properties (extinction coefficient, backscatter coefficient, depolarization), temperature, pressure, wind, humidity, trace gas concentration (ozone, methane, nitrous oxide, etc.) (Cracknell, et al, 2007).

There are several major components to a LiDAR system:

- a) **Laser** — 600–1000 nm lasers are most common for non-scientific applications. They are inexpensive, but since they can be focused and easily absorbed by the eye, the maximum power is limited by the need to make them eye safe. Eye-safety is often a requirement for most applications. A common alternative, 1550 nm lasers, are eye-safe at much higher power levels since this wavelength is not focused by the eye, but the detector technology is less advanced and so these wavelengths are generally used at longer ranges and lower accuracies. They are also used for military applications, as 1550 nm is not visible in night vision goggles, unlike the shorter 1000 nm infrared laser. Airborne topographic mapping LiDAR's generally use 1064 nm diode pumped YAG lasers, while bathymetric systems generally use 532 nm frequency doubled diode pumped YAG lasers because 532 nm penetrates water with much less attenuation than does 1064 nm. Laser settings include the laser repetition rate (which controls the data collection speed). Pulse length is generally an attribute of the laser cavity length, the number of passes required through the gain material (YAG, YLF, etc.), and Q-switch speed. Better target resolution is achieved with shorter pulses, provided the LiDAR receiver detectors and electronics have sufficient bandwidth (Cracknell, et al, 2007).

It is important to mention that lasers are classified by wavelength, power, and potential for biological damage (Figure 4):



- b) **Scanner and optics** — How fast images can be developed is also affected by the speed at which they are scanned. There are several options to scan the azimuth and elevation, including dual oscillating plane mirrors, a combination with a polygon mirror, a dual axis scanner. Optic choices affect the angular resolution and range that can be detected. A hole mirror or a beam splitter are options to collect a return signal.
- c) **Photodetector and receiver electronics** — Two main photodetector technologies are used in LiDAR's: solid state photodetectors, such as silicon avalanche photodiodes, or photomultipliers. The sensitivity of the receiver is another parameter that has to be balanced in a LiDAR design.
- d) **Position and navigation systems** — LiDAR sensors that are mounted on mobile platforms such as airplanes or satellites require instrumentation to determine the absolute position and orientation of the sensor. Such devices generally include a Global Positioning System (GPS) receiver and an Inertial Measurement Unit (IMU).

There are a wide variety of applications of LiDAR, as often mentioned in National LiDAR Dataset programs, in agriculture, archaeology, biology and conservation, geology and soil science, meteorology and atmospheric environment, law enforcement, military, physics and astronomy, robotics, surveying, cultural heritage. In case of the Construction Industry and Civil Engineering, LiDAR is seen as a relatively new and innovative tool used for documentation and structural health monitoring, as-built drawings of existing structures, reverse engineering, digital twinning, 3D modelling used to perform FEA and other engineering analysis.

Overall, there are many different types of LiDAR based laser scanners on the market as for example static (Figure 5), mobile (Figure 6), hand-held (Figure 7), and UAV devices (Figure 8).



Figure 6 – Static scanners (Trimble TX8 – left, Z+F IMAGER – right)



Figure 7 – Mobile scanner (Leica Pegasus Backpack)



Figure 8 – Hand-held scanner (Leica BLK2GO)



Figure 9 – UAV scanner (DJI Zenmuse)

Traditionally, LiDAR systems and laser scanners are expensive and large pieces of equipment that capture real-world environments. Since 2020, **Apple Inc.** have introduced a LiDAR sensor in some iPhone and iPad models (Figure 10), namely iPhone 12 Pro, iPhone 12 Pro Max, iPhone 13 Pro, iPhone 13 Pro Max, iPhone 14 Pro, iPhone 14 Pro Max, iPad Pro 2020, iPad Pro 2021 and iPad Pro 2022 (as of May 2023). Compared to other LiDAR devices in the market, the LiDAR-equipped iPhones/iPads are available at cheaper prices ($\leq 2000 \text{ EUR}$) and are lighter in weight (187–684 g). These iPhones/iPads have been found suitable for acquiring 3D point clouds. This enables Apple device users to create realistic, accurate, and fast 3D representations of close-range objects and environments. The Apple LiDAR Scanner can measure the distance to surrounding objects up to 5 meters away, works both indoors and outdoors, and operates at the photon level at nano-second speeds. The LiDAR sensors create accurate high-resolution models of small objects with a side length $> 10 \text{ cm}$ with an absolute accuracy of $\pm 1 \text{ cm}$. New depth frameworks in iPadOS combine depth points measured by the LiDAR Scanner, data from

both cameras and motion sensors, and is enhanced by computer vision algorithms on the A12Z Bionic for a more detailed understanding of a scene (Apple Inc., 2020).

The laser is emitted from a Vertical Cavity Surface Emitting Laser (VCSEL) at a near infrared spectrum in a 2D array. Compared to common Edge Emitting Lasers (EEL), VCSELs are convenient for mobile devices (Figure 11), as they can be constructed in small dimensions featuring a feasible ratio between laser power consumption and supplied power as well as a narrow wavelength bandwidth. Flash illuminating facilitates the observation of the entire field of view (FoV) at once, but it is also limiting the size and range of the FoV. The direct time of flight (dTOF) of the pulses emitted by the VCSEL is measured with a Single Photon Avalanche Photodiode (SPAD). Increases in power density of VCSELs in combination with SPADs makes flash-LiDAR solutions feasible for consumer-grade devices like the iPad and iPhone. The VCSEL emits an array containing 8×8 points that is diffracted into 3×3 grids, making a total of 576 points. The focal length is equivalent to 26 mm and therefore the same as the main 12 MP camera of the iPad and iPhone (Luetzenburg, et. al., 2021).



Figure 10 – Smartphone scanner (Apple Inc.)

The implications of using this technology are mainly related to augmented and mixed reality applications, but its deployment for surveying tasks also seems promising. Over the last two years, an increasing number of mobile apps using the Apple LiDAR sensor for 3D data acquisition have been released. However, their performance and the 3D positional accuracy and precision of the acquired 3D point clouds have not yet been fully validated. Among the solutions available, as of May 2023, four iOS apps are worth mentioning: SiteScape, EveryPoint, 3D Scanner App and Polycam.

The scanning performed with a smartphone will not replace precise solutions based on terrestrial laser scanning. This is mainly due to the fact that the accuracy achieved with the Apple products are reliable to a single centimetre, and thus this type of device can be used for work of limited accuracy. The cost of scanning with an iPhone is low enough to certainly have a positive impact on the popularity of using point clouds and their derivative products in construction and other fields.

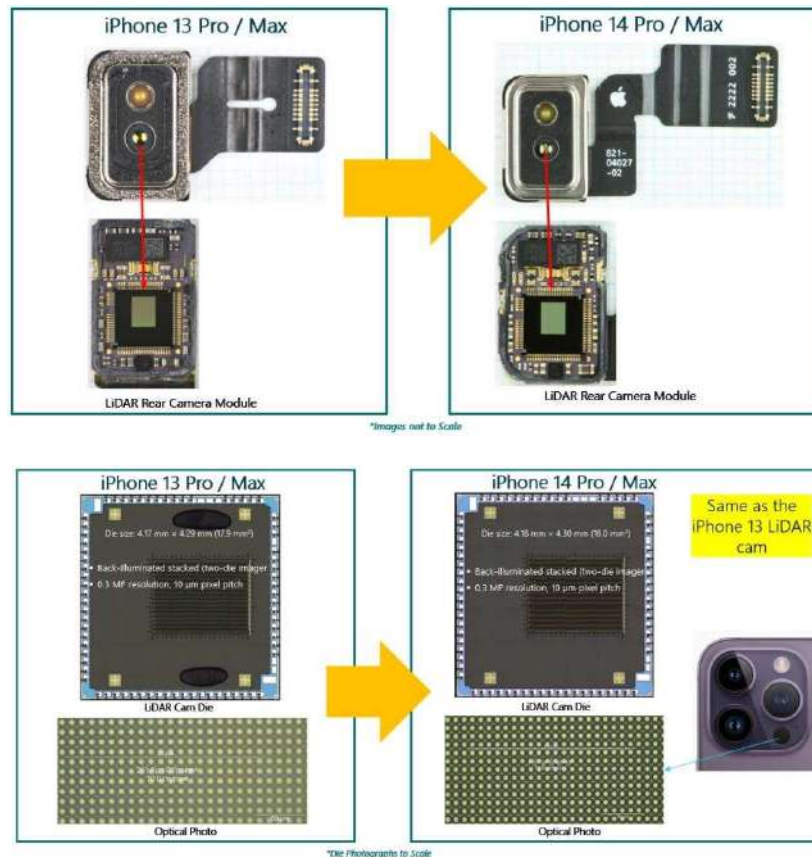


Figure 11 – LiDAR Rear Camera CIS (Apple Inc.)

Overall, the LiDAR sensor introduced by Apple Inc. in 2020 for the iPad Pro and iPhone Pro models presents a novel, cost effective and time efficient alternative to established methods of 3D scanning. Although accuracy and precision of the iPhone LiDAR models do not reach state-of-the-art standards, improvements in raw point cloud export, maximum scan size and range are only a matter of time for the still novel software applications.

To conclude, in Table 1 is shown a comparison chart of different types of 3D scanners based on Lidar technology, to compare the technical information applicable to the main types of scanners (static, mobile, hand-held, UAV and smartphone) provided by the most important manufacturers on the market (Trimble, Z+F, Leica, DJI) and a relatively new competitor (Apple Inc.). Based on the provided technical information, it is visible that most of Lidar scanners have a laser class of 1, meaning that they are incapable of causing injury to the eye, they have a wavelength between 830 and 1500 nanometres, a wide operating range, high resolution but also require a high financial investment, elaborate logistics, complicated training of the user and extensive data processing. Recently, off-the-shelf drones equipped with Lidar sensors already reduced the costs for obtaining a high-resolution dataset considerably, but they are well suited for just a few types of applications such as topographic surveying, structural health monitoring or disaster management. In terms of pricing, but depending on the type of application, accuracy and range demand,

the solution provided by Apple Inc. could be seen as a new and more convenient alternative. Further research is still demanded to evaluate the capabilities of the smartphone scanner for different applications such as surveying, reverse engineering, or other types of measurements.

Table 1 – Comparison between different Lidar scanners

Device name	Trimble TX8	Z+F IMAGER 5010C	Leica Pegasus	Leica BLK2GO	DJI Zenmuse	Iphone 14Pro
Scanner type	static	static	mobile	hand-held	UAV	smartphone
Dimensions (w x d x h)	335 x 386 x 242 (without tripod)	170 x 286 x 395 (without tripod)	730x 270 x 310	279 x 80	152 x 110 x 169	147.5 x 71.5 x 7.85
Weight (kg)	11.2	9.8	11.9	0.7	0.9	0.2
Laser class	1	1	1	1	1	1
Laser wavelength (μm)	1.5	1.5	1.5	0.83	0.90	0.94
Range (m)	0.6 - 120	0.3 – 187.3	1 - 200	0.5 - 25	2 - 450	0.1 - 5
Resolution (mm)	2	0.1	20	3	30	10
Data acquisition rate (pts/sec)	1 mill.	1.016 mill.	0.9 mill.	0.42 mill.	0.48 mill.	-
Price (€)	≈75.000	≈100.000	≈65.000	≈55.000	≈30.000	≈2000

3.2.1.1.2 Interferometry

The notion of **interferometry** describes the use of the interference of different light waves to record the 3D position in space. Optical interferometry has been used since the nineteenth century. Due to the limited intensity and coherence of conventional light sources, measurements were limited to distances of only a few centimetres. With the advent of laser technology these restrictions have been overcome. This technique allowed the development of interferometry as a fast, versatile, and high-precision measurement technique for measuring long distances.

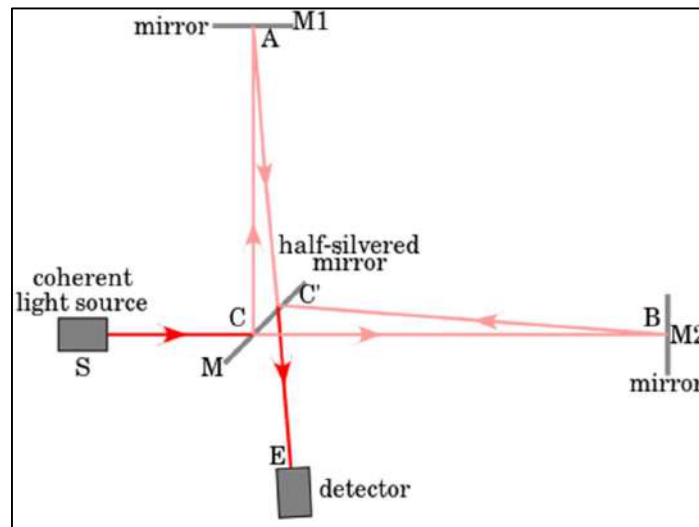


Figure 12 – Michelson interferometer principle

Interferometric distance measurements provide a much higher degree of accuracy than time-of-flight. However, it is preferable that the measurements in this case be carried out in controllable atmospheric environments (for example, in indoor stations, in enclosures) and the distances to be measured do not exceed the order of tens of meters. In an interferometric laser scanner, the laser beam is divided using a ray divider, which reflects one side of it (half) in one direction (the reference arm) and transmits the other half to the measuring arm. Both sides of the radius go through the two different paths and when they combine, the so-called interference fringes occur. Very small displacements (of the order of fractions of wavelengths) can be detected (using coherence detection) and in this way longer distances can be measured by counting wavelengths. Many systems are based on this principle, as they have as a main feature the very high accuracy, but – on the other hand – they are very expensive and because of the more rapidly development of other modern scanning methods (time-of-flight, triangulation, structured light), interferometry is mainly used in industrial quality control measurements for relatively small surfaces or objects.

Modern white-light based interferometers use the interference effects that occur when the light reflected from the sample is superimposed with the light reflected by a high-precision reference mirror. The collimated light beam is split into a measurement beam and a reference beam at a beam splitter. The measurement beam strikes the sample, the reference beam strikes a mirror. Light reflected from the mirror and the sample is recombined at the beam splitter and focused onto a camera.

Whenever the optical path for an object point in the measuring arm and the optical path in the reference arm are the same, constructive interference takes place for all wavelengths in the light source's spectrum and the camera pixel of the object point in question has maximum intensity. For object points with a different optical path, the assigned camera pixel has a low intensity. Consequently, the camera registers all the image points at the same height.

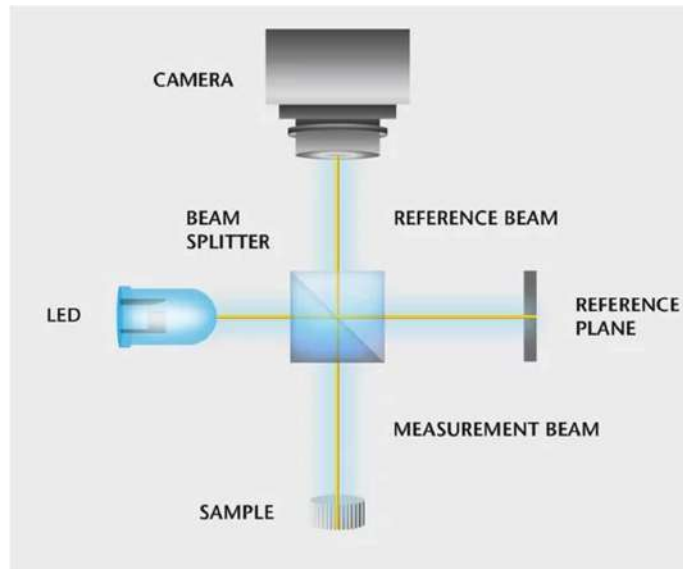


Figure 13 – Principle of modern white - light interferometers

These interferometers are mainly used when determining the topography of functional surfaces is needed, in industrial quality control measurements, and for microstructure detailing. Under optimal conditions they can achieve precision in the sub-nanometre range.

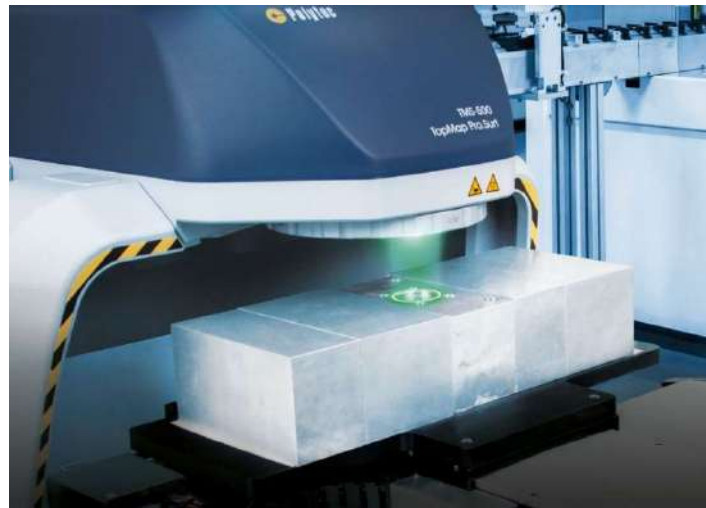


Figure 14 – TopMap Pro.Surf (Polytec Interferometer)

3.2.1.2 Structured light

Historically known as “white light” 3D scanners, mainly structured light 3D scanners are a type of non-contact metrology that white LED projected light to produce 3D measurements. This technology has been on the market for almost 20 years and used commercially as early as 1995. Using the same trigonometric method as laser scanners the distance from the sensors to the light source is known but works by projecting a

pattern of light onto the object to scan and not a laser line (or dot) (Figure 15). These 3D scanners project a light pattern consisting of bars, blocks, or other shapes onto an object.

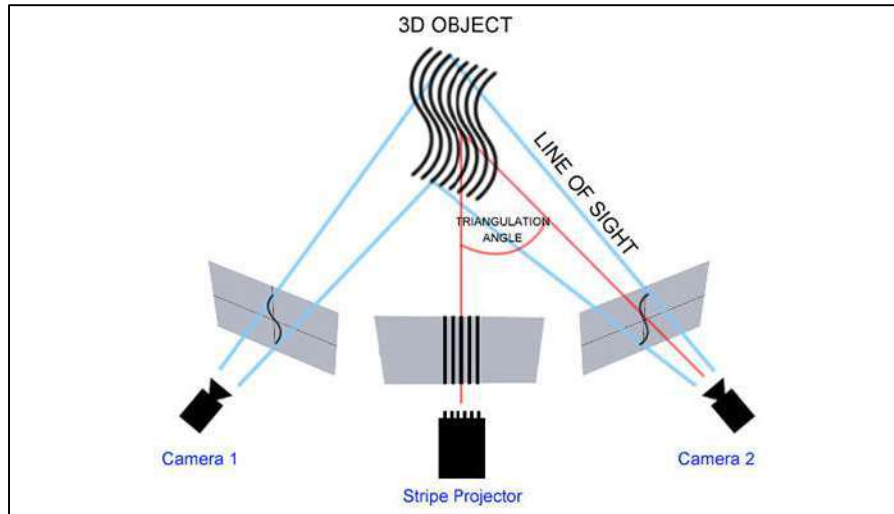


Figure 15 – Structured light scanner principle

Structured light sensors, usually utilize visible non-coherent light sources for object point coding purposes that are projected on a whole camera field of view, thus being able to measure points in a range of a million within a single view measurement. Because of its non-coherent light source type, there is no speckle effect affecting the recorded images, but its light intensity decreases rapidly with distance from the source. Early types of sensors consisted of a single camera and single projecting device (Figure 16), but since the two cameras provide over-determined mathematical triangulation model, sensors with the two cameras of the same focal distances are nowadays more widespread. If there is a need for more than a single view measurement, unlike dual camera systems, single camera systems require a precise turntable or the robotic positioning devices since they can't exploit the passive photogrammetric principles which require more than one observation of the same visually coded object spot. However, numerical registration of raw 3D points in different coordinate systems could replace the need of a precise mechanical alignment units providing there is a sufficient overlapping surface area with the distinctive features (Georgopoulos, et. al.,2010).



Figure 16 – Traditional white light scanner (HP PRO S3)

The benefit of structured light technology is how fast scans are. A scan can be achieved in about 2 seconds and the scanning area is also quite large (Webster, 2016). Just like laser scanners, structured light scanners offer a high resolution.

One of the disadvantages of this type of scanner is that they are sensitive to the lighting conditions in a given environment. This is less true of laser scanners. For example, working outside would be extremely difficult.

White light scanners can capture a whole area simultaneously, instead of a single line or crosshair at a time. This provides a great richness in detail, and all but eliminates motion distortion. Some of these 3D scanners are even able to provide the live measurements of a moving object.

Blue light 3D scanning technology is the advanced version of the white light technology, has shown better precision, higher accuracy, and improved data quality. One reason why blue light 3D scanning provides stronger benefits is its **wavelength** (Figure 17). While white light is a combination of all the colours in the visible spectrum, blue light has a narrow surface that is optimal for filtering out interference from ambient light.

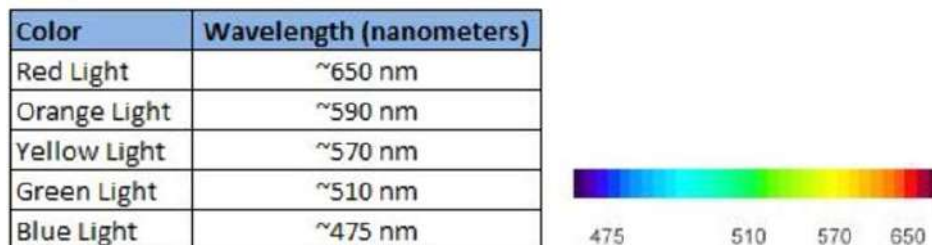


Figure 17 – Wavelength of different colours

Scanners that project a fringe pattern (sometimes called “structured light”) take their measurements over time. They require several sequential projections to be done at a given time, and their decoding occurs through a temporal projection. Their results are therefore not instantaneous and require the device to be static. In comparison, white light scanners that project a coded pattern can be handheld and moved, which greatly

increases their flexibility and ease of use. They provide very quick results, since their measuring area is larger, and the scanner decodes the specific light pattern for each frame the camera captures (Ebrahim, 2014).

When compared to traditional laser scanning, structured light scanning offers several advantages. Laser scanners use laser beams to measure an objects surface and is often a tedious, labour-intensive operation, requiring the user to leverage a portable 3D scanner or articulated arm and wave the scanner over the scanned object, leading to redundant and overlapping data. Structured light scanners use a camera mounted on a tripod or robot for a **point-and -shoot style workflow** that minimizes setup and programming.

While still very reliable, light coded pattern scanners typically achieve the accuracy of other 3D scanners (up to 0.007 mm) just in controlled environments, but they provide both unrivalled speed and flexibility. The technology is working based on the following principles:

- **Signalising** - a special projector casts a specifically designed type of light pattern onto the measurement object;
- **Capturing** - each structured light scanner is equipped with two digital camera units that capture this projection at predefined viewing angles. The entire measuring process takes between a few seconds and several minutes and is completed as soon as images from all sides of the object have been captured;
- **Calculating** - the resulting images are then analysed based on the principle of spatial image triangulation and used to derive highly accurate dimensional information about the measurement surface.

The type of structured pattern projected onto the scene or object to be captured plays a key role in determining the speed, achievable resolution, and accuracy of the system (Bell, et. al., 2014). A summary of several different structure pattern encodings is presented next (Webster, 2016):

- **2D pseudorandom codifications** – in this approach, an array of size $n_1 \times n_2$ is encoded via a pseudorandom sequence such that any $k_1 \times k_2$ kernel within the array is unique. To encode the array, the polynomial modulo n^2 method is used, which can be mathematically described as:

$$2^{n-1} = 2^{k_1 k_2} - 1 \quad (8)$$

$$n_1 = 2^{k_1} - 1 \quad (9)$$

$$n^2 = 2^n - 1/n_1 \quad (10)$$

The benefits of this method are that it is based on a well-documented approach that is easy to understand and implement. Drawbacks of this method, however, include its sensitivity to noise and its inability to achieve a high spatial resolution. The resolution limitations are constrained by the resolution of the projector in both directions. An example of pseudorandom pattern, is shown in Figure 18.

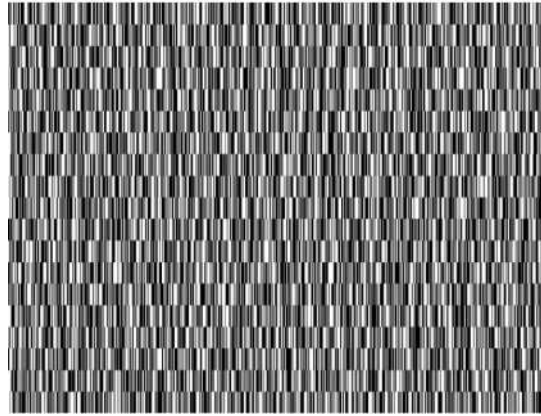


Figure 18 – Example of pseudorandom structured pattern

- **Binary structured codifications** – in this approach a scene is encoded by using just two intensity values (Figure 19): all black (intensity 0) and all white (intensity 1). The spatial resolution using binary codes is limited by the projectors and the camera's resolution. Within one projected binary pattern, each pixel within a stripe will contain the same intensity value (either a 1 or a 0) as each stripe must be larger than one of the projector's pixels. Given this, however, the individual pixels within the stripe cannot be differentiated. As pixel-level correspondence between the camera and the projector cannot be obtained, a high measurement accuracy using the binary codification is difficult to achieve. As only two intensity values are used to construct a unique codeword for each pixel, it takes n patterns to encode 2^n pixels. As the number of pixels increases, then so does the number of patterns required to achieve a dense 3D scan.

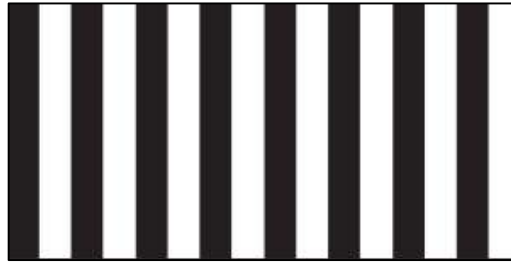


Figure 19 – Example of binary encoded pattern

- **N-ary codifications** –a scene is encoded with more than just two intensity values (Figure 20), any subset of values from 0 to 255. The use of many intensity values effectively decreases the number of patterns that need to be projected to encode a scene. One advantage of this fact is an increase in potential sensing speed. However, using many intensity values can lead to disadvantages because of noise and surface variations. Also, as many values between 0 and 255 may be used, sometimes without much contrast between them, this method is very sensitive to the focus level of the projector and camera.

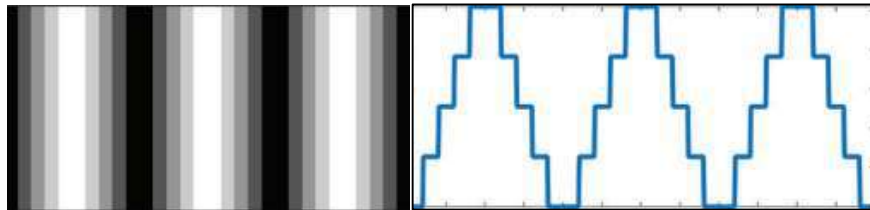


Figure 20 – Example of n-ary encoded pattern and its cross-section

- **Triangular phase codifications** – a triangular pattern refers to the shape a plot of the cross section of the pattern makes. One disadvantage of using a single pattern is its high sensitivity to noise. To address this, more patterns can be used to uniquely encode a scene. To generate more triangular patterns, the original triangular structure can be **shifted** by some amount (Figure 21).

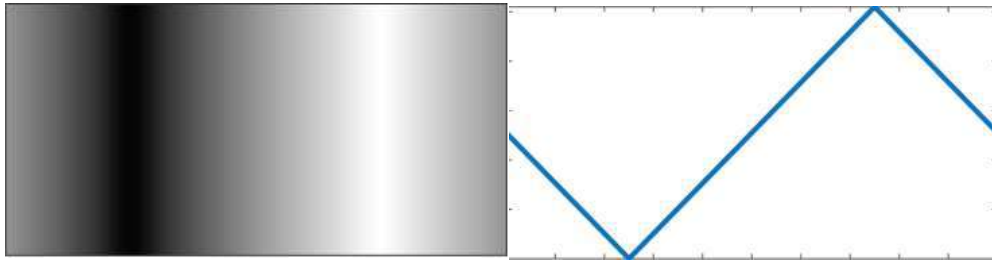


Figure 21 – Example of triangular phase encoded pattern and its cross-section

- **Trapezoidal phase codifications** – This method (Figure 22) maintains the speed offered by triangular approaches via the use of intensity ratio calculations yet is six times less sensitive to noise (Huang, et. al., 2004).

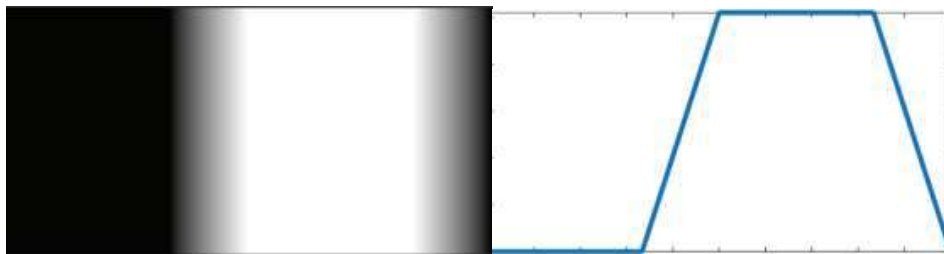


Figure 22 – Example of trapezoidal phase encoded pattern and its cross-section

- **Continuous sinusoidal phase codifications** - With sinusoidal patterns (Figure 23), pixel-level resolution is possible as intensities vary across the image from point to point at known frequencies and therefore can be differentiated. Given this, the correspondence between the camera and the projector can be determined more precisely, thus increasing the potential sensing accuracy of such method. These sinusoidal patterns, also known as fringe patterns, have been studied extensively in optical metrology due to their ability to reach pixel-level spatial resolution. To generate such fringe patterns, the used principle is the **digital fringe projection**, which uses a digital video projector to project computer-generated sinusoidal patterns onto the scene to be scanned. Instead of using intensity values to establish correspondence, phase information is used. One benefit of this is an inherent robustness to surface texture variation.

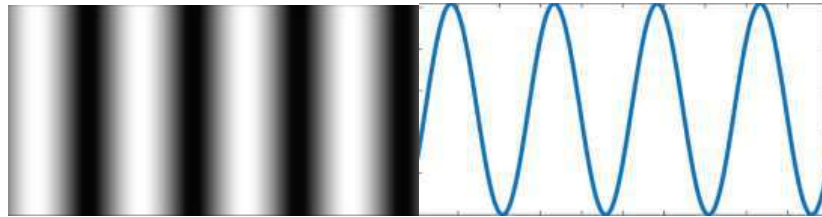


Figure 23 – Example of sinusoidal phase encoded pattern and its cross-section

As mentioned before, currently there are two main structured light technologies used widely for 3D scanning in different fields of application: **white light technology** and **blue light technology**. In many senses, blue light is just a more efficient and useful alternative to white light scanners. In comparison with other 3D scanning technologies, white light and blue light scanners are less sensitive to heat and can achieve the same quality results when scanning in a controlled environment, but as an important disadvantage, there are other locations (such as outdoors) where the quality is inferior to laser scanners (sensitive to the lighting conditions). In comparison with laser scanners, the concern about **eye-safety danger** is missing because of the fact that structured light is being based on simple light.

In summary, structured light technology has his own strengths and weaknesses. Deciding if structured light is suitable for a project largely depends on the following parameters: **the scanned object (dimensions)**, **scanning environment and resolution**.

Because of the high accuracy they can provide (up to 0.007 mm), the advantage to capture also reflective or transparent surfaces (in comparison to laser scanners), the range of applications is wide and varies from industrial metrology and quality control, reverse engineering, volume measurements, documenting objects of cultural heritage, capturing environments for augmented reality, to body shape measurements, wrinkle measurement on leather or cardiac mechanics analysis. Data from these scanners can be also utilized for CFD and FEA simulation and analysis to assist in calculating displacement, stress and strain under internal and external loads, mainly in the fields of aerospace engineering, automotive and transportation or mechanics. One important disadvantage that comes with this technology is that the environment in which the scan is taking place needs to be controlled (laboratory conditions).

Overall, there are two main types of structured light scanners existing on the market, based on the light source (white or blue). The scanners can be found in different forms, based on the type of application they are used: static (Figure 24), automated (Figure 25) or hand-held (Figure 26).



Figure 24 – Example of static blue light scanner (Hexagon Stereo scanner)



Figure 25 – Example of automated blue light scanner (Capture 3D - ATOS 5)



Figure 26 – Example of handheld white light scanners (left – Creafom Go! SCAN3D, right – Artec 3D Leo)

In Table 2 is presented a comparison between six structured light scanners selected from the market and based on their technical specifications, it can be concluded that this technology has its own benefits (high speed, accuracy, resolution) and downsides (small part size range).

Table 2 – Comparison between different structured light scanners

Device name	Creaform GO! SCAN 3D	Hexagon Stereo	Capture 3D ATOS 5	Artec 3D Leo	HP PRO S3	Range Vision PRO
Light source	white	blue	blue	white	white	blue
Dimensions (w x d x h)	89 x 114 x 346	600 x 430 x 260	550 x 320 x 200	227 x 163 x 228	323 x 613 x 209	408 x 350 x 125
Weight (kg)	1.25	12	14	1.8	8.8	6.5
Stand-off distance (mm)	400	840	880	1000	500	900
Accuracy (mm)	0.05	0.01	0.02	0.1	0.03	0.01
Part size range (m)	0.1 – 4	0.075 – 1	0.1 – 1	0.2 – 2	0.03 – 0.5	0.03 – 1.2
Resolution (mm)	0.2	0.01	0.02	0.2	0.05	0.03
Data acquisition rate (pts/sec)	1.5 mill.	8 mill.	12 mill.	35 mill.	2.3 mill.	15 mill.
Price (€)	≈35.000	≈65.000	≈55.000	≈40.000	≈5.000	≈15.000

3.2.1.3 Triangulation

It is a method used for precise measurement of distances, using sensors based on laser triangulation. The National Research Council of Canada was among the first institutes to develop the triangulation-based laser scanning technology in 1978 (Roy Mayer, 1999). The name is suggested by the fact that the emitted laser beam and the reflected, together with the base (the distance between the laser emitter and the CCD camera) form a triangle. The length of one side of the triangle, the distance between the camera and the laser emitter are known. The angle of the laser emitter corner is also known. The angle of the camera corner can be determined by evaluating the location of the laser dot in the camera's field of view (Figure 27). These three parameters fully determine the shape and size of the triangle. In most cases, laser stripes, or a single laser dot, are swept across the scanned object but to speed up the acquisition process, the laser stripes are preferred [Site 11]. There are four main components of a 3D triangulation

system: **the camera, the line projector (laser-based), a moving mechanism** that moves the object or camera/laser system through the field of view of the imaging system and a **software to process the captured image and accurately translate pixel offsets.**

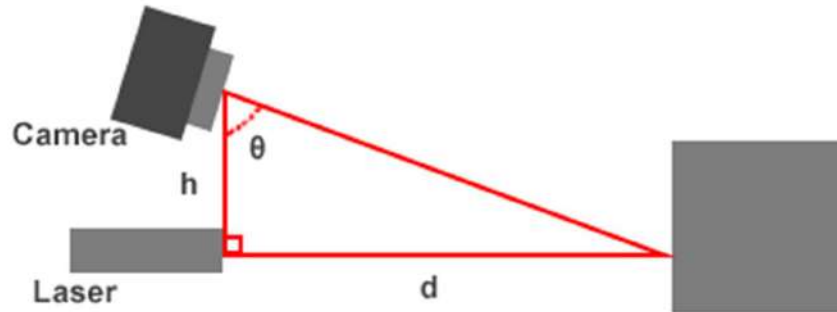


Figure 27 – Triangulation principle

The distance from the instrument to the scanned object (d) is determined geometrically from the length base (h) and recorded angle (θ). The 3D position of the surface element on which the laser beam is reflected derives from solving the equation:

$$d = h \times \tan(\theta) \quad (11)$$

Based on the number of cameras, we can distinguish two main types of scanners using triangulation:

- *one-camera solution* - in principle, in this method, a beam of laser rays is emitted by the instrument and is reflected from the surface of the object towards a collecting lens, located on the instrument at a known distance from the transmitter. The lens focuses the image of the reflected laser spot, which is detected and collected by a video camera, usually a CCD sensor (Charged Coupled Device). Depending on the model, the camera includes a measuring range between 45° and 65° with respect to the measuring center. The angle of the emitted laser beam is recorded by the device (it can be defined and changed incrementally), also the distance between the laser source and the video camera is known from calibration.
- *multi-camera solution* - is based on the same principle, but with the use of two CCD cameras, located at the ends of the base (Figure 28).

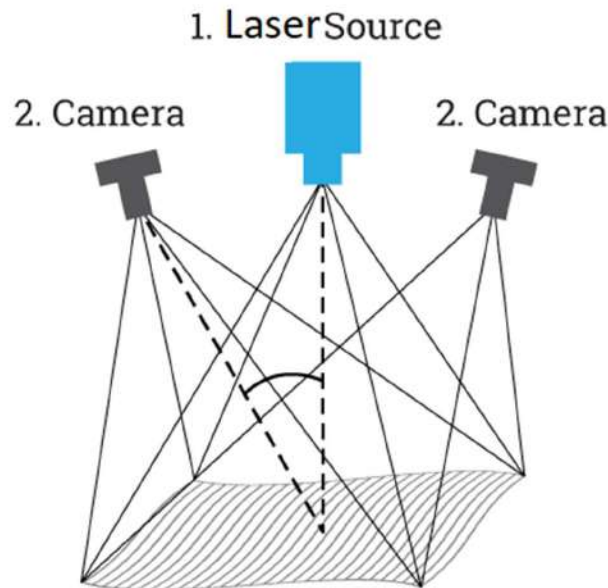


Figure 28 – Triangulation principle – multi-camera solution

Since a laser beam is used to sweep around an object for the purpose of its 3D representation, this implies that the angle of the laser beam must be changed gradually as it traverses the object. Due to the physical limitations of using a larger measurement base and field of camera view, scanners that use the principle of triangulation are used in general for applications where the stand-off range is less than 10 metres. However, compared to scanning systems that are based on the principle of time measurement, triangulation offers a very high precision of determining the spatial positions of an object, in micron range.

In practice, the method of **active triangulation** was introduced to solve the problem of the measurement technique from classical triangulation. The issue, corresponding to the classic triangulation, can be summarized as follows: two different images taken from two different points (of view), relative orientation of the two cameras and adjusting (matching) the paired points in the two images. To identify the matching points between the two images can be time consuming and incomplete. The active triangulation method uses the radius laser to solve this problem by marking the points on the object with the help of its colour, so that this point can be easily detected in the image.

Currently there are three main categories of scanners available on the market based on the laser technology, with respect to their field of use: **blue-laser**, **red-laser** (quality control, reverse engineering, cultural heritage) and **green-laser** (bathymetry).

Laser beams are produced using special techniques, which usually involve a special substance through which photons are produced and released as a focused beam of laser. Photons are produced by means of a chemical reaction on a particular substance that emits photons of a particular wavelength, which are then concentrated using a tube and reflective mirrors to produce an intense beam of light. Energy is added to the usual light by this process.

The most widely used scanners are based on the blue-laser technology, because it is in fact an improved version of the red-laser technology, mainly due to their wavelengths. In comparison red-laser has a wavelength of 630-670 nanometres, while blue-laser has just 360-480 nanometres.

Overall, laser scanners that use the triangulation principle have a limited range of some meters, but their accuracy is relatively high in comparison with Lidar scanners. When comparing with structured light, triangulation is more advantageous regarding the fact that it does not require controlled laboratory conditions. Due to these advantages, a series of applications have been identified such as: prototyping, quality Control, FE analysis, aerodynamics, reverse engineering, automotive modelling and design modifications, virtual assembly, cultural heritage preservation, virtual reality, augmented reality, wound monitoring, medical prosthesis design.

Based on the form in which they are manufactured, two main types of scanners are distinguished: equipped with a *measuring arm* (Figure 29) or *hand-held* (Figure 30).



Figure 29 – Laser scanners with measuring arms (left – Hexagon Absolute arm, right – Nikon Model Maker H120)

The combination of a laser scanner and measuring arm enables a spherical measuring volume depending on the maximum reach of the arm and an automated fusion of the scanned laser lines. The arm calculates the exact position of the probe at each point through embedded encoders on each axis (or joint) in the arm. To account for the different reflection behaviour of surfaces the camera exposure time can be adapted. The measuring arm ensures higher precision and accuracy for the scanning process, determine, and

record the location of a probe in 3D space and report the results through software. The arm calculates the exact position of the probe at each point through embedded encoders on each axis (or joint) in the arm. Measurement arms are available in multiple working volumes, typically from 1.2 to 4.5 metres (with a radial reach from 0.5 to 2 metres in any direction). They are also characterized by the number of rotational axes – arms typically come in 6 or 7-Axis configurations, with 6-Axis models used in high accuracy, hard probing applications and 7-Axis models used when additional articulation is needed for use with laser scanning attachments and specialty probes. Hand-held laser scanners are less accurate in comparison with those equipped with a measuring arm but are more reliable in terms of pricing and speed.



Figure 30 – Hand-held laser scanners (left – Creafom Handyscan 3D, right – ZG Scan 717)

Hexagon, Faro, Nikon, Creafom, Zeiss, ZG Technology are just a few examples from a vast variety of manufacturers that are providing solutions on the laser scanning market. In Table 3 is presented a comparison between five scanners selected from the mentioned manufacturers, in terms of accuracy, range, speed and price.

Table 3 – Comparison between different laser scanners

Device name	Creaform HANDYSCAN 3D Black	Hexagon Absolute Arm	FARO Quantum Max	Nikon Model Maker H120	ZG SCAN 717
Scanner type	hand-held	measuring arm	measuring arm	measuring arm	Hand-held
Laser type	blue	blue	blue	blue	red
Laser class	2M	2	2	2	2
Dimensions (w x d x h)	79 x 142 x 288	based on the arm	based on the arm	based on the arm	310 x 147 x 80
Working volume of arm (m)	-	1.2 – 4.5	2 - 4	2 – 4.5	-
Weight (kg)	0.94	12	10	11	0.83
Stand-off distance (mm)	300	115	115	80	300
Accuracy (mm)	0.025	0.01	0.07	0.08	0.02
Part size range (m)	0.05 – 4	0.05 – 4.5	0.05 – 4.5	0.06 – 5.25	0.1 – 4
Resolution (mm)	0.025	0.04	0.035	0.035	0.05
Data acquisition rate (pts/sec)	1.3 mill.	1.2 mill.	1.2 mill.	1.5 mill.	0.48 mill.
Price (€)	≈60.000	≈100.000	≈80.000	≈100.000	≈40.000

3.2.2 NON-CONTACT PASSIVE SCANNERS

Passive scanners do not emit any kind of radiation, instead they rely on detection of radiation reflected by the environment (visible light or radiation from infrared range). Passive methods use, most of the time, only one digital camera. These techniques are based on finding correspondence between 2D images, which, not always have a unique solution. The accuracy of this method depends largely on the resolution of the image acquisition system and the density of properties identifiable in the image. There are three main passive scanning techniques (Trebuña, et. al., 2018):

- **Photogrammetric techniques** - usually employ two video cameras, slightly apart, looking at the same scene. By analysing the slight differences between the images seen by each camera, it is possible to determine the distance at each point in the images. This method is based on the same principles driving human stereoscopic vision.
- **Stereoscopic techniques** - usually use a single camera but take multiple images under varying lighting conditions. These techniques attempt to invert the image formation model in order to recover the surface orientation at each pixel.
- **Silhouette techniques** - use outlines created from a sequence of photographs around a three-dimensional object against a well contrasted background. These silhouettes are extruded and intersected to form the visual hull approximation of the object.

3.2.2.1 Photogrammetry

Photogrammetry, as its name implies, is a three-dimensional coordinate measuring technique that uses 2D photographs (a block of overlapped images) as the fundamental medium for metrology or measurement for a wide range of applications. The principle used in photogrammetry is triangulation. By taking photographs from at least two different locations, so-called 'lines of sight' can be developed from each camera to points on the object. These lines of sight, sometimes called rays owing to their optical nature, are mathematically intersected to produce the three-dimensional coordinates of the points of interest, , basically the photographs are mathematically intersected to create accurate three-dimensional coordinates. With photogrammetry, the quality of the measurement depends on exposure, field-of-view (FoV), and focus (Horswell, 2013).

Another fundamental property of a photogrammetric image is the image scale or photo-scale ((Luhmann, et. al., 2006)). The photo-scale factor m defines the relationship between the object distance h and principal distance c . Alternatively it is the relationship between an object distance X in the object, in a direction parallel to the image plane, and the corresponding distance in image space x' :

$$m = \frac{h}{c} = \frac{X}{x'} \quad (12)$$

Photogrammetry can be categorised by method of recording and processing in:

- Analogue photogrammetry;
- Analytical photogrammetry;
- Digital photogrammetry.

Digital photogrammetry evolved from analogue photogrammetry, which appeared simultaneously with the invention of photography. By camera position and object distance, two general types of photogrammetry can be identified: **aerial** (uses aerial images acquired by satellite, commercial aircraft or UAV drone to collect images of buildings, structures and terrain) and **terrestrial** (with the camera handheld or on mounted on a tripod). Terrestrial photogrammetry dealing with object distances up to ca. 200 m is also termed **close-range photogrammetry** (Aber, et. al., 2010).

Aerial photogrammetry (Figure 31) can be classified depending on the angle of the optical axis in: *vertical (nadir)*, *high oblique*, *low oblique* or *panoramic*. Aerial photogrammetry provides a **bird's eye** view of large areas, enabling to capture features of the earth surface or structures in their spatial context. In Figure 32 are presented three types of image acquisition methods for aerial photogrammetry.

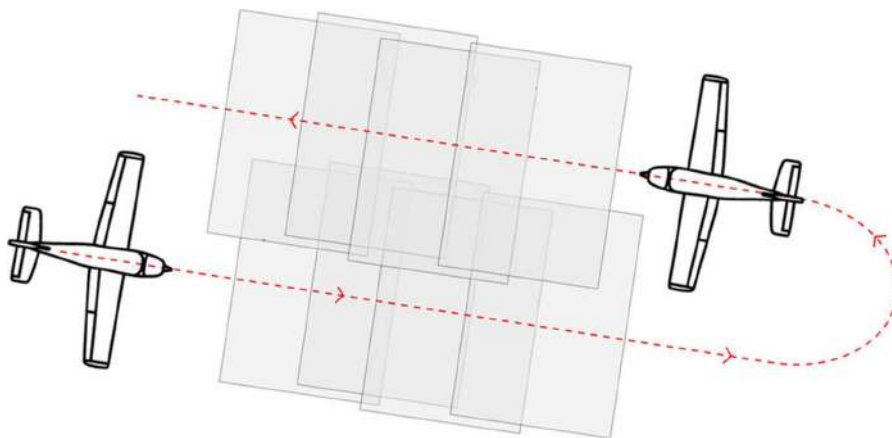


Figure 31 – Aerial photogrammetry principle of overlapping

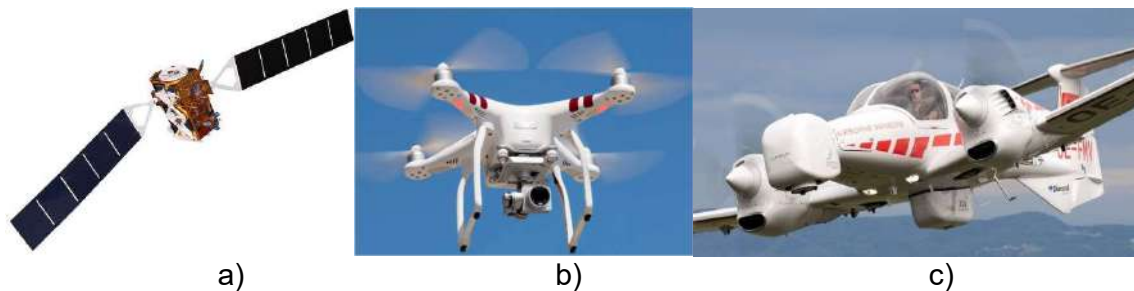


Figure 32 – Aerial photogrammetry methods of data acquisition : a) satellite (Sentinell 1 – European Space Agency); b) drone (DJI Phantom); c) commercial aircraft

Close-range photogrammetry is a technique for obtaining geometric information, e.g. position, size and shape of any object, that was imaged on **horizontal photos** before. There are different approaches for the photogrammetric restitution of an object (Figure 33):

- *Single images;*
- *Stereographic processing;*

- *Bundle restitution.*

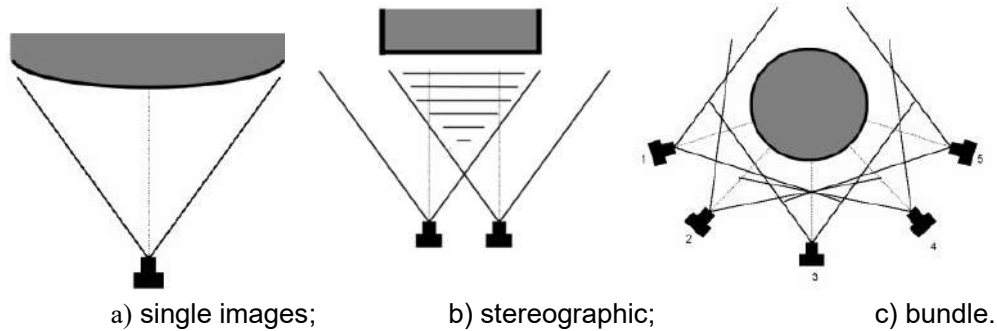


Figure 33 – Close-range photogrammetry approaches

3D geometry can be reconstructed just using the stereographic or bundle approaches, because a single image is insufficient. The following steps are involved in the processing of photogrammetric images:

- Determining the centre of each frame (**interior orientation**): the interior orientation establishes transformation parameters between the camera coordinate system and the image pixel coordinate system. This is done by: the measurement of the fiducial marks in the images expressed in the image pixel coordinate system. Fiducial marks are marks on the edges of the camera field that define the camera coordinate system by means of their coordinate values. The amount and the position of the fiducial marks depends on the camera type or camera manufacturer) in the images expressed in the image pixel coordinate system.
- Automatic and semi-automatic correlation processes are used to align the frames with each other (**relative orientation**) Relative orientation is the process of recovering the position and orientation of one image with the other in an individual image space coordinate system.
- Determine the absolute position and orientation of each frame in space (**absolute orientation**) Absolute orientation is a fundamental and important task in photogrammetry and robotics. It aims to find the best transformation parameters which relate the stereo model coordinates and geodetic coordinates.

These steps generate oriented stereoscopic modules (pairs of orientated frames) that can be easily handled. Another important step for obtaining high-quality photogrammetric measurements is the improvement of the digital images and can be accomplished by one of the following methods:

- *Contrast enhancement* - is performed for images that have low contrast;
- *Noise reduction* - this method highlights hard-to-reach images and limits image colours;
- *Image binarization* - method of obtaining black and white images from an

image that additionally contain undesired images for unpleasant technological reasons;

- *Image restoration* – implies removing any distortions that affect the image;
- *Image segmentation* is the process of splitting up uniform regions of interest in the image.
- *Outline extraction* - provides a closed outline.

Figure 34 shows what type of information exchange takes place in a photogrammetric measurement.

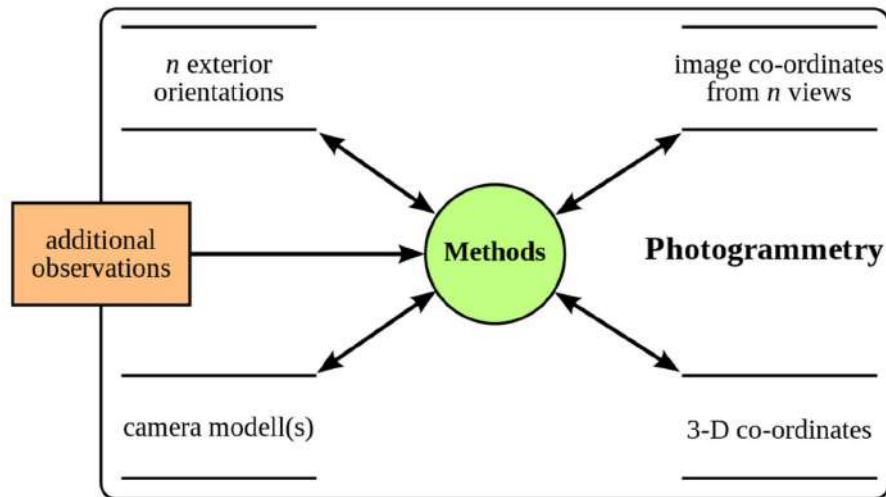


Figure 34 – Data exchange in a photogrammetric measurement

The *3D coordinates* define the locations of object points in the 3D space. The *image coordinates* define the locations of the object points on the film or an electronic imaging device. The *exterior orientation* of a camera defines its location in space and its view direction. The *inner orientation* defines the geometric parameters of the imaging process. This is primarily the focal length of the lens but can also include the description of lens distortions. Further *additional observations* play an important role: with *scale bars*, basically a known distance of two points in space, or known *fix points*, the connection to the basic measuring units is created. Each of the four main variables can be an *input* or an *output* of a photogrammetric measurement.

Based on the application area, photogrammetry can be categorised as follows:

- **engineering photogrammetry** - applications include the measuring of coordinates, quantification of distances, heights, areas and volumes, preparation of topographic maps, digital terrain models, generating digital elevation models and orthophotographs, cadastre, 3D modelling, structural health monitoring, as-built drawings.
- **architectural photogrammetry** - cultural heritage documentation, archaeology, building facade and elevation reconstruction for architectural purposes.

- **industrial photogrammetry** – applications include automotive and aerospace manufacturing, car body deformation measurement, crash testing, part-to-part alignment.
- **biostereometrics** – medical applications such as medical CAD/CAM, 3D modelling of prosthetics.
- **forensic photogrammetry** – police investigations.

The successful use of photogrammetry in these applications require several technical components that form an efficient and economic system (Luhmann, 2010). The following list summarises these components and related technical issues:

- ***imaging sensor***: resolution (number of pixels), available lenses, acquisition and data transfer speed, camera stability, synchronisation, data compression;
- ***targeting and illumination***: representation of interesting object features, target shape and size, wavelength of light sources, restrictions to object access, illumination power and measurement volume;
- ***imaging configuration***: number of camera stations, desired measurement accuracy, network design, redundancy, robustness, self-calibration ability, datum definition and object control, self-control of orientation and calibration;
- ***image processing***: automation of target recognition and identification, sub-pixel measurement of target centre, multi-image matching approaches, feature tracking;
- ***3D reconstruction***: methods for determination of 3D coordinates (e.g. spatial intersection, bundle adjustment) and error statistics;
- ***data interfaces***: integration into CAD/CAM environments, machine and data interfaces, user interaction and displays, etc; and
- ***verification of accuracy***: reference bodies, reference data, standards and guidelines, and acceptance tests.

The imaging sensor technology is the key feature of a photogrammetry system. The process of selecting an optimal imaging sensor device is influenced by a range of factors including resolution, accuracy, speed and frequency of data acquisition, synchronization, volumetric data capacity, spectral data precision, range of visibility, digital connectivity, as well as the cost considerations associated with the device. Generally, it is deemed favourable to utilize cameras possessing superior resolution, imaging speed, and precision to facilitate optimum efficiency and productivity, while concurrently ensuring minimal expenses and enhanced investment returns for the system. Nowadays the range of available cameras and imaging sensors is huge. Based on CCD (charge-coupled device) and CMOS (complementary metal oxide semiconductor that converts photons to electrons for digital processing) technology, sensors are available with very high resolutions (up to 60 Mpixel), very high frame rates (up to 2000 Hz), pixel sizes varying between about 1.4 and 15 μm , and different sensor formats (Figure 35).



Figure 35 – Nikon D6 based on CMOS technology

High-resolution digital SLR (single-lens reflex) cameras are also available with sensors between 10 and 60 Mpixel. Suitable cameras in classical small format (35 mm SLR) are offered by companies such as Nikon, Canon, and Sony (Figure 36-a), whereas medium-format cameras are available from Rollei, Hasselblad or Alpa (Figure 36-b). For applications that do not require high accuracy and resolution, a reliable alternative is the smartphone (Figure 36-c); recent developments on the smartphone market facilitate the use of this relatively new instrument in photogrammetry.



Figure 36 – DSLR cameras in small and medium format vs Smartphone camera

There are still very few cameras specifically designed for close-range photogrammetric applications. The classical ‘metric camera’ approach with stable interior orientation requires high additional effort in terms of optical and mechanical sensor design (Luhmann, 2010). The main advantage of these cameras is their assured stability and the consequent reduced need for periodic or on-the-job calibration, for example in applications where high accuracy is demanded without the technical possibility for simultaneous camera calibration. Depending upon the mechanical stability of the cameras and their relative orientation, such systems can provide measurement accuracy of about 0.05 mm

over a range of up to 2 m. Accuracy in absolute length measurement is closer to 0.1 mm and the overall accuracy is generally stated at around 1:20,000 (Luhmann, 2010).

Relatively new, specially designed close-range photogrammetric instruments (Figures 37-38) are available from manufacturers such as Hexagon and Arago by Rigsters (innovative automated photogrammetry).



Figure 37 – DPA Industrial photogrammetry camera (Hexagon)

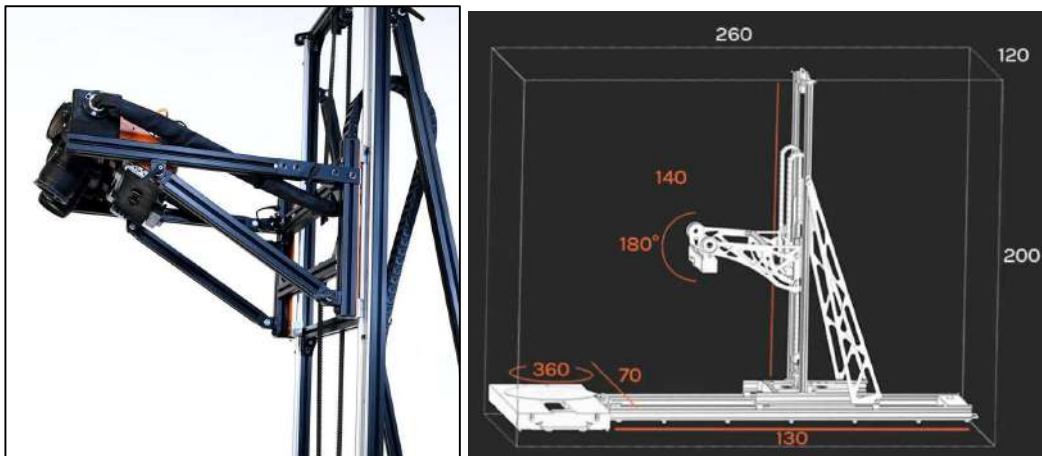


Figure 38 – Arago automated photogrammetry (Rigsters)

Overall, the drawbacks of photogrammetry are that it is time-consuming, requires a relatively high amount of expertise to carry out correctly, and even then, may not produce the needed results if the conditions aren't proper. A photogrammetric measurement might need dozens – sometimes hundreds – of photos, ensuring that each picture is of sufficiently high quality and that there is adequate overlap between images. Also, changes in lighting conditions from one photo to the next can be a major drawback.

In Table 4 is presented a comparison in terms of accuracy, resolution, speed, and price, between four instruments selected from the mentioned manufacturers.

Table 4 – Comparison between different photogrammetric instruments

Device name	Nikon D6	Hasselblad H6D-100c	Apple Iphone 14 PRO	Hexagon DPA
Sensor type	CMOS	DSLR	OIS	C1
Dimensions (w x d x h)	160x163x92	153x131x122	147.5x71.5x7.85	300x100x170
Weight (kg)	1.27	2.10	0.2	2.8
Accuracy (mm)	-	-	-	0.02
Resolution (MP)	20.8	100	48	50.6
Data acquisition rate (frames/s)	5.5	1.5	10	5
Price (€)	≈7.000	≈30.000	≈2000	≈45.000

3.2.2.2 Silhouette

Silhouette techniques are another important category of non-contact passive measurement methods that are widely used in different engineering applications such as industrial metrology, inspection, and testing or for research purposes. From this category are worth mentioning the well-established **digital image correlation** and **virtual image correlation** techniques.

Since the 1970s, digital image correlation (DIC) applications have been rapidly growing in different engineering fields. DIC combined with a stereo camera system offers full-field measurements of three-dimensional shapes, deformations (i.e., in-plane and out-of-plane deformations), and surface strains, which are of most interest in many structural testing applications. DIC systems have been used in many conventional structural testing applications (Shadmehri, et. al., 2019).

Formerly, DIC was used for measuring deformations and strains on a planar object subjected mainly to in-plane loadings. This was referred to as two-dimensional (2D) DIC, which to date remains an important technique for 2D deformations and strain measurements in material testing. However, nonplanar objects subjected to out-of-plane loading and deformations are mostly unavoidable in practice. In the 1990s, 2D DIC was extended to three-dimensional (3D) measurements through stereovision systems (Figure

39). Referred to as 3D DIC, the system consists of two or more cameras to capture digital images of the object of interest from two or more perspectives. Using a stereoscopic sensor setup, the position of each point in the area of interest is focused on a specific pixel in the camera plane. If the orientation of the sensors with respect to each other (extrinsic parameters) and the magnifications of the lenses and all imaging parameters (intrinsic parameters) are known, the 3D position of any point in the area of interest can be calculated by applying image correlation algorithms.

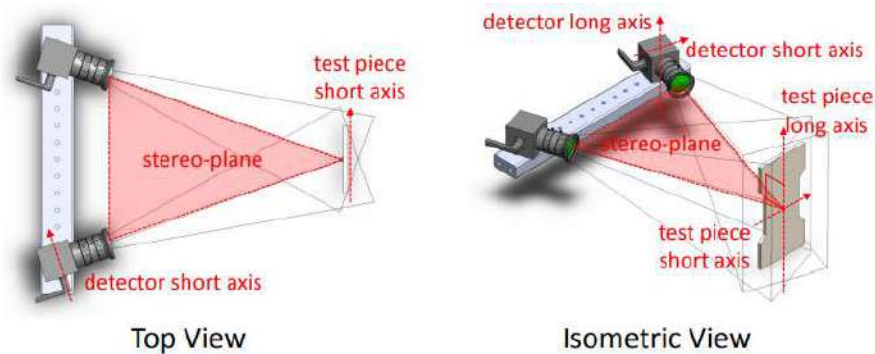


Figure 39 – Schematics depicting the recommended orientation of the cameras in a stereovision system

This process determines the shift and/or rotation and distortion of little facet elements in the reference image. For a surface with no texture or a uniform texture, each location is indistinguishable from any other point. A speckle pattern (Figure 40) can be applied to the surface to provide a means of uniquely identifying every point. A small area is defined around each point on the surface. These areas are known as subsets. For a properly applied speckle pattern each subset will have an arrangement of speckles which is unique from any other subset. If the locations of enough subsets can be found in pictures taken before and after the application of a load, then the displacement field can be determined. High resolution digital cameras are used to capture photographs of the specimen before and during (or after) loading. The center of the subsets is tracked instead of random points because the pattern in the subset will be statically unique, as opposed to individual points that appear very similar to one another. If the position of many subsets centres can be tracked from the photograph of an unloaded specimen to the photograph of the loaded specimen a deformation field can be generated (Davidson, 2008).

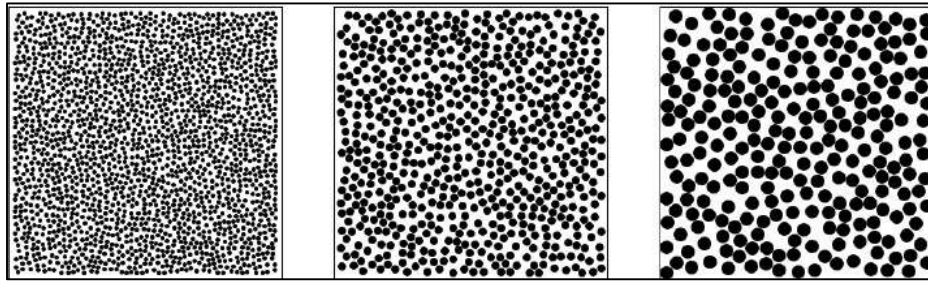


Figure 40 – Three-different-speckle-patterns used for DIC

The use of the virtual image correlation (VIC) technique involves identifying the optimal match between a contour or silhouette that is present within an image and a contour or silhouette that is described through an analytical representation in a virtual image. The optical parameters of the virtual image are obtained thanks to a minimization process. The sub-pixel precision and the robustness of the method are shown onto practical experiments. Examples of use are given in the fields of strain measurement, metrology of engineered parts, mechanical testing, and metrology of highly deformable structures. With other words, the virtual correlation method has been formerly issued from the DIC: the reference image, which does not exist in the case of interest where the goal is to measure a boundary in a sole image, is replaced by a virtual image. This one consists in a sketch description of the contour or silhouette which is to be measured, based on a curve with a grey level evolving smoothly from white to black (François, et. al., 2016). An example of VIC system is presented in Figure 41.



Figure 41 – VIC 3D (Correlated solutions)

The workflow of a DIC application includes the following steps:

- apply uniform base coat to the measured specimen;

- apply speckle pattern;
- focus cameras;
- capture calibration photos;
- capture null speckle photos;
- load specimen;
- capture load speckle photos;
- import calibration and speckle photos into specialised image correlation software;
- calibrate system;
- set null photo as reference;
- run correlation;
- calculate measurements;
- export data.

3.3 DATA PROCESSING OF 3D SCANS AND MODEL RECONSTRUCTION

The usual result obtained from measurements based on the listed principles is represented by a (considerable) number of points, called in the literature **point cloud**. The point cloud is a collection of points, defined as position by XYZ coordinates in a common system of reference, which reveals to the observer information about the spatial shape, position, and distribution of an object or group of objects. It may also contain additional information, such as intensity. The point clouds produced by 3D scanners and 3D imaging can be used directly for measurement and visualisation. It can be concluded that the point cloud contains two types of information:

- *metric*, which describes the geometry of the object and its spatial relations with the environment.
- *thematic*, which are used to describe the surface properties of scanned objects and to estimate the accuracy of the acquired data.

Depending on the size, shape, and complexity of the scanned objects, they could require multiple scans from different positions. In each position, a set of coordinates is obtained (point cloud) defined in a local, internal coordinate system of the instrument. To combine (assemble) these different positions, it is necessary to know the positions and orientation of the coordinate systems for each scan relative to a local/global coordinate system of the scanned area. This transformation, from a theoretical point of view, takes place according to the next equation:

$$x_c = R \times x_s \quad (13)$$

where:

- R – is the rotation matrix;
- t – is the translation vector;
- x_c – are coordinates in the common system;
- x_s – are coordinates in the instruments system.

Practically, the process of combining results from various positions of different point clouds and transforming these results into one common coordinate system (common point cloud), is defined as **registration**. Registration can be considered as a preliminary phase of **georeferencing** (the process of coupling point clouds into a single system), but there are also cases (situations) in which this is assimilated with georeferencing, when registering individual point clouds is made directly in the chosen external coordinate system.

Following the registration and georeferencing operations, the resulting common point cloud

can enter the modelling process. The final product of this operation is represented by a 3D model of the scanned object. The modelling procedures are specific to practical applications. **Point cloud processing** involves transforming the recorded raw point cloud into a final product. These final products can be presented in a multitude of shapes and formats: cleaned (from noise) point cloud, standard 2D representations (plans, elevations, profiles) or complex 3D models suitable for various purposes. There are currently both open-source and licensed applications available on the market for point cloud processing (CloudCompare, Euclidean, Point Cloud Library). An example of a point cloud is depicted in Figure 42.

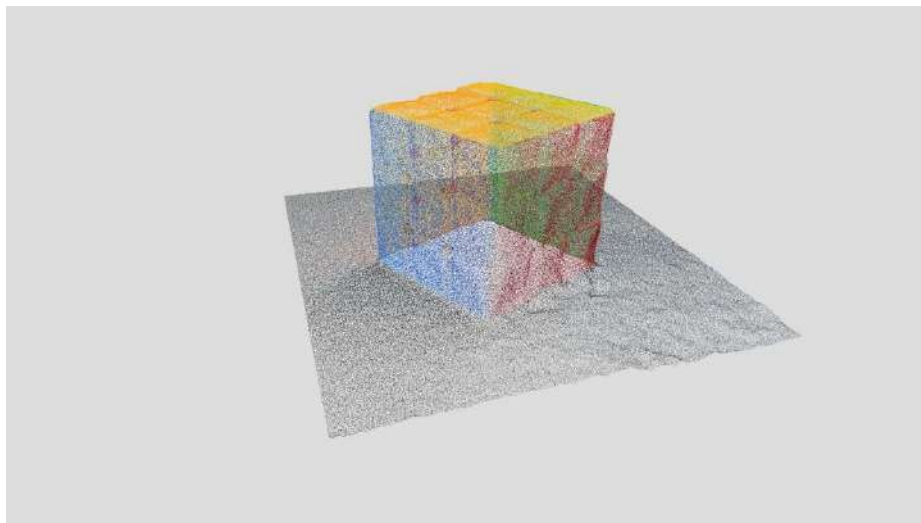


Figure 42 – Point cloud obtained from a scanned cube

Other types of data obtained directly from the scanning process or based on the point cloud processing are **polygon mesh models**, **surface models** and **solid CAD models**. In a polygonal representation of a shape, a surface is modelled as many small faceted flat surfaces. Polygon models, also called mesh models, are useful for

visualization, but can be very large data sets, and are relatively un-editable in this form. Reconstruction to polygonal model involves finding and connecting adjacent points with straight lines in order to create a continuous surface. Many applications, both open-source and licensed, are available for this purpose (GigaMesh, MeshLab, PointCab, PolyWorks, Rapidform, Geomagic, Imageware, Rhino 3D etc.).

One of the well-established methods for reconstruction to polygonal models is the **Delaunay method**. This method involves extraction of tetrahedron surfaces from initial point cloud. The Delaunay triangulation is a cell complex that subdivides the convex hull of the point sampling. If the point sampling fulfils certain non-degeneracy conditions, then all faces in the Delaunay triangulation are simplices and the Delaunay triangulation is unique (Cazals, et. al., 2006). The combinatorial and algorithmic complexity of the Delaunay triangulation grow exponentially with the dimension of the embedding space of the original surface. With other words, as shown also in Figure 43 the Delaunay triangulation explores the neighbourhood of a sample point in all relevant directions in a way that even accommodates non-uniform point samplings.

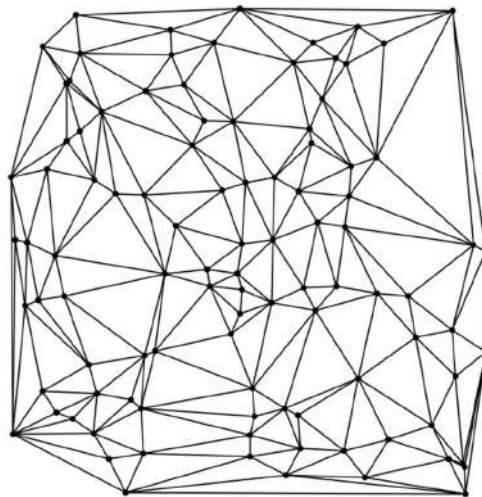


Figure 43 – Delaunay triangulation method

Another method for 3D reconstruction of a point cloud in a **surface** defined as **zero set method**, is performed using a distance function which assigns to each point in the space a signed distance to the surface. A contour algorithm is used to extract a zero-set which is used to obtain polygonal representation of the object. Thus, the problem of reconstructing a surface from a disorganized point cloud is reduced to the definition of the appropriate function f with a zero value for the sampled points and different to zero value for the rest. An algorithm called **marching cubes** (Figure 44) established the use of such methods. Loss of geometry precision in areas with extreme curvature, i.e., corners, edges is one of the main issues encountered. Furthermore, pre-treatment of information, by applying some kind of filtering technique, also affects the definition of the corners by softening them. There are several studies related to post-processing techniques used in

the reconstruction for the detection and refinement of corners, but these methods increase the complexity of the solution (Wang, 2006).

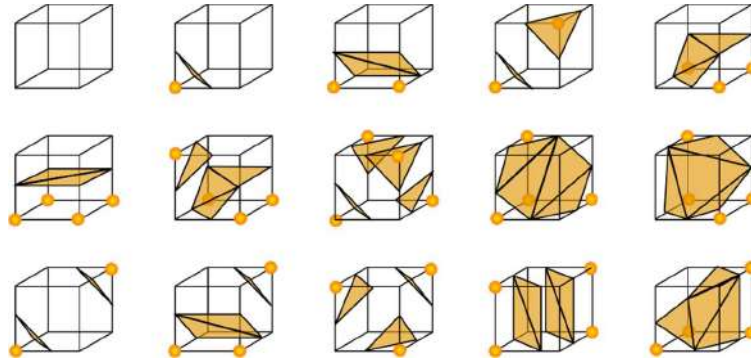


Figure 44 – Marching cubes algorithm

The next level of sophistication in modelling involves using a quilt of curved surface patches to model the shape. These might be **NURBS** (non-uniform rational basis splines), **TSplines** or other representations of curved topology (Figure 45). Using NURBS, the spherical shape becomes a true mathematical sphere. These models are somewhat editable, but only in a sense of deforming the surface. Providers of surface modelling applications include Rapidform, Geomagic, Rhino 3D, Maya, T Splines etc.

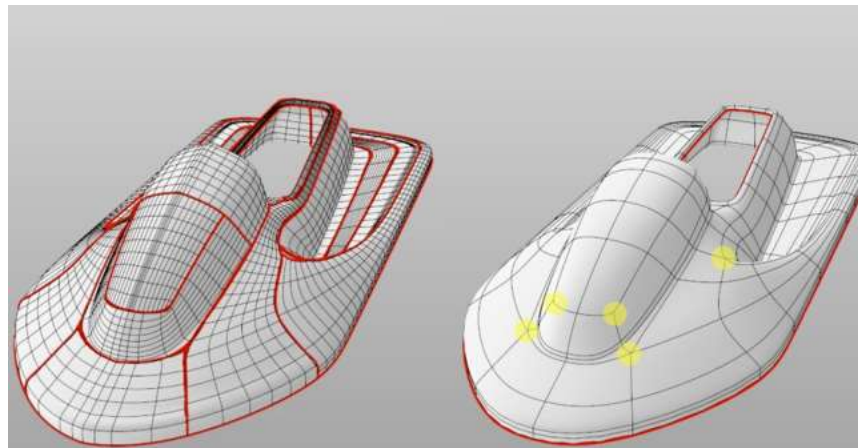


Figure 45 – Comparison between NURBS (left) and T-splines (right)

From an engineering/manufacturing perspective, the ultimate representation of a digitized shape is the editable, parametric CAD model (**solid model**).

These **solid models** (Figure 46) describe not simply the envelope or shape of the object, but also embody the "design intent". With other words the geometry of a solid model is *complete* (points in a 3D space can be classified within and outside the model), *valid* (vertices, edges, faces are connected properly), and *unambiguous* (only one interpretation of an object). Currently the CAD market offers various programs that can enable solid modelling, such as SolidWorks, Xtract3D, DeziignWorks, CATIA, AutoCAD, Revit, Geomagic, Imageware, Rhino 3D, Rapidform, etc.

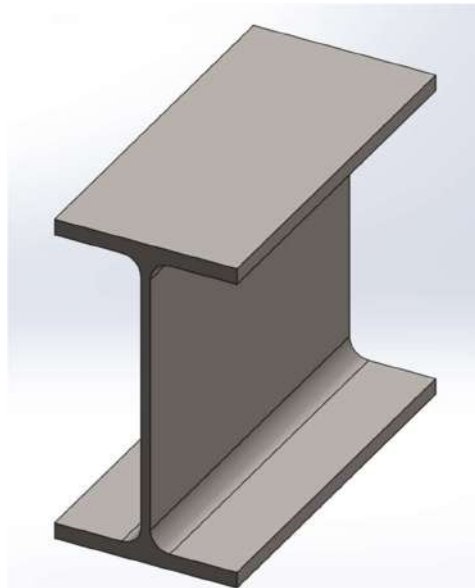


Figure 46 – Example of a solid model

3D data acquisition and object reconstruction can also be performed using **stereo image pairs**. Stereo photogrammetry or photogrammetry based on a **block of overlapped images** is the primary approach for 3D mapping and object reconstruction using 2D images. Close-range photogrammetry has also matured to the level where cameras or digital cameras can be used to capture the close-look images of objects, e.g., buildings, and reconstruct them using the very same theory as aerial photogrammetry (Figure 47).

Programs such as RealityCapture, Metashape, Agisoft or 3DF Zephyr are used for image overlapping (alignment) with the aim of obtaining a point cloud. Cleanup and further processing can be performed with applications such as MeshLab, GigaMesh, Netfabb or MeshMixer to obtain a polygon mesh.

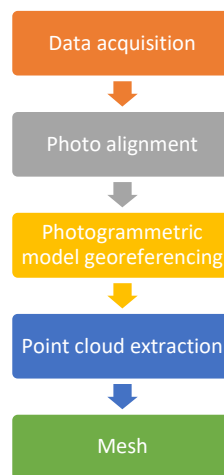


Figure 47 – Photogrammetric data processing workflow

4 CURRENT APPLICATIONS OF 3D SCANS IN CIVIL ENGINEERING

Current applications of 3D scans in the field of civil engineering and construction industry include: mapping an existing construction site, design validation, construction progress evaluation, creation of 3D building models (BIM models), structural health monitoring (detecting structural changes resulting from exposure to extreme loadings such as earthquake, impact, or fire), surveying, as-built drawings of bridges, industrial buildings, and monuments, documentation of historical sites, quality control, create GIS (Geographic information system) maps and Geomatics.

However, the potential use of spatial 3D point clouds remains an emergent topic among researchers for a vast variety of applications. The following chapter provides an overview of the available research on this topic.

4.1 STRUCTURAL HEALTH MONITORING

Vacca, et. al., 2016 presents an interesting approach to use the terrestrial laser scanner for monitoring the deformations and the damages of buildings. Three case studies were mentioned relating to damaged and/or unsafe buildings: Sivillier Castle (Villasor - Sardinia- Italy), the Bell Tower of Mores (Sardinia-Italy) and industrial building (Cagliari – Italy). A laser scanner survey (LIDAR) was carried out that not only provided valuable information but also highlighted structural metric deformation and degradation. Firstly, the study of the deformation of some vertical walls of Sivillier Castle (XV Century). Secondly, the study of the verticality of a Bell Tower (XIX Century), 40 m high, and the degradation of the statue at the top of it. Thirdly, the study of the deformation of an industrial building which was subjected to fire. The utilization of TLS for the monitoring of structures offered a non-destructive approach, provided the geometry of the structures (form and dimensions). The processing of the point clouds into 3D models were done with JRC Reconstructor Software v. 3.1.0, (Gexcel Ltd). The obtained 3D models were highly accurate and allowed the study of structural deformations.

Xie, et. al., 2017 developed a 3D modelling algorithm for tunnel deformation monitoring based also on terrestrial laser scanning (LIDAR). Using the proposed algorithm, relative deformation of the tunnel including settlement, segment dislocation and cross section convergence can be visualized using computer programs such as Cyclone and Matlab. The point cloud was firstly transformed into a text file (TXT) so that Matlab can process the data. Also, a case study of the Shanghai West Changjiang Road tunnel was presented, where TLS was applied successfully to measure tunnel deformation over multiple sections. The proposed 3D modelling algorithm processed the point cloud to allow visualization of the relative deformation of the tunnel.

Cui, et. al., 2023 is also presenting an interesting approach, for generating finite element mesh from 3D laser point clouds for tunnel structures. The point cloud model of the tunnel was acquired using terrestrial laser scanning and mobile laser scanning. The finite element mesh was obtained from the raw point cloud data using a newly developed

clock simulation extraction algorithm. Further, the generated FE model of the tunnel structure was used for numerical simulation analysis in Abaqus.

4.2 CULTURAL HERITAGE – DIGITAL DOCUMENTATION, BIM, AND STRUCTURAL ANALYSIS

Vilceanu, et. al., 2021 presented the use of laser scanning for conservation of cultural heritage buildings. In the framework of a case study that refers to a residential building situated in the municipality of Timisoara, Romania, considered as a historic monument, a TLS measurement was performed both before and after its rehabilitation. The measurements provided diverse kinds of products such as a 3D model, as-built drawings, and architectural renderings.

Guarnieri, et. al., 2008 proposed a 3D model-based structural analysis on a structure belonging to Cultural Heritage. Namely, the outer and inner side of the walls of Montagnana, an ancient city near Padova, Italy, aiming to detect the areas of the wall requiring consolidation works. Acquired point clouds were registered in Cyclone employing retroreflective target to strength the alignment results, which were compared with the ones obtained by the application of Procrustes Analysis algorithms, in order to verify the effectiveness of such registration method. After that cross sections have been extracted from the global 3D model, where wall thickness and shape variation were clearly visible, for structural analysis. Cross-sections extracted from the unified 3D model of the walls were imported as DXF in the Straus software for the linear static analysis aiming to study the response of the wall structure to three different effects: self-weight, wind load and out off-plumb effect.

A highly relevant contribution to this field is proposed by Funari, et. al., 2021, developing a framework for digital twin generation of historic masonry structures based on point clouds. The paper has shown the benefits of being able to monitor in real-time the evolution of the behaviour of existing structures. The proposed procedure exploits the capabilities of Generative Programming, in which the user can interact with the code by modifying and/or implementing new capabilities with the aim to obtain a valid solid model based on point clouds. The workflow includes the definition of a Python script for the real-time interoperability between Rhino3D + Grasshopper and Abaqus CAE. The approach has been applied and validated through a case study: the Church of St. Torcato in Guimarães (Portugal). In this paper, the link between Grasshopper and Abaqus CAE is performed by using LunchBox plugin for Grasshopper along with the mentioned pre-compiled Python code, which enabled the transition of the parametric model to the FE environment for structural engineering purposes. LunchBox allowed to export the full geometry of the church in .stp file format that runs within Abaqus program assembling the FE model. The proposed approach has shown efficiency from the computational point of view, being able to perform the transition from half-raw survey data (point clouds) to geometrical entities in a short amount of time. The calibrated FE model was able to simulate the damage pattern caused by the foundation settlement accurately.

Fregonese et al., 2015 developed a procedure to obtain a 3D model for BIM purposes. Once the model from the 3D survey is obtained, solid model software was recreated directly in Autodesk Revit, where each single element was modelled using a system family or “Model in Place”. This BIM software has allowed to model historical and complex elements in a parametric way which allowed it to be connected with a database. However, due to the limitations of BIM commercial software, the authors have developed software for the management and planning of restoration operations.

Barazzetti et al., 2015 have showed a procedure for BIM generation from point clouds via BIM parameterization of NURBS (non-uniform rational B-spline) curves and surfaces using Revit software. In the case study, the authors suggest a procedure that provides BIM objects of complex elements by using the NURBS surface turned into specific BIM families. Using this approach, some problems were found in the modelling of complex objects and in the building of the layer-based reconstruction.

Eigenraam et al., 2016 presents a method in order to obtain free-form shell structures from point cloud to finite element model. In the paper, special attention is given to the geometric accuracy, considering that shape and force interact. The method was applied to Heinz Isler’s models for reverse engineering purposes.

Furno et al., 2017 compared two different modelling methods: one based on the use of NURBS and the parametric one on BIM objects, using Rhinoceros and Revit software. The “direct” modelling of Rhinoceros made it possible to process the survey data and obtain a model divided into blocks, with the possibility of modifying the intrinsic parameters of the individual elements using the Grasshopper plug-in (included in Rhinoceros). However, the model obtained in this way does not add information of any kind to the elements. For this reason, the modelling of the same structure was also performed with the Revit software and applied to Milan Cathedral in Italy.

León-Robles et. al, 2019 discussed HBIM (Heritage–BIM) applied to a masonry bridge using Revit commercial BIM software, but they encountered great difficulties in doing so because only a few families of libraries are dedicated to the modelling of complex civil constructions such as bridges. Moreover, in this case study, an analysis of the deformations between the designed model of the bridge and that surveyed was carried out.

Bassier et al., 2019 suggest a fast and accurate procedure to capture the spatial information required using FEM. The workflow involves two parallel methods: the former converts the point cloud to a complex FEM mesh (through a series of semi-automated procedures) while the second extracts crack information and enhances the FEM mesh to incorporate the crack geometry.

Pepe, et. al., 2020 presents another efficient pipeline to obtain 3D models for Heritage-BIM and structural analysis purposes from 3D point clouds. The paper reports two study cases: the church San Nicola in Moontedoro and San Cono bridge. After performing geomatics surveys, the obtained point clouds into the Rhinoceros software. It was possible to create detailed profiles in the specific part of the structure and, consequently, to build complex and irregular shapes according to NURBS-type

geometries. For irregular geometries, it was possible to use an additional plug-in developed in Rhinoceros, called “EvoluteTools PRO”, which was able to generate highly complex NURBS surfaces. Each NURBS surface was transformed into a solid through modelling in Rhinoceros. The solid geometric objects were exported into Midas GTS NX software, for the structural mesh to be built.

Angelini, et. al., 2017 suggested that a BIM approach for cultural heritage structure is indispensable when the goals are to achieve: an integrated project, integrate and manage each project phase and management (surveying, architectural design, restoration project, the design of the different installations, the construction project, resource management, management of the result. The paper presents a case study in which the Papal Basilica of Saint Francis in Assisi, Italy was reconstructed in 3D by using LIDAR. The acquisition and the registration of the scans, performed for the individual spaces, was done by means of the Cyclone software, proceeding, at first to the alignment between the different scans referring to each space and, subsequently, to their georeferencing. In order to convert the point cloud into a final 3D model, the scans were exported to “.xyz” format and then imported into “Geomagic” software format. The obtained models were converted into several formats to allow exporting them in open source or CAD software. Firstly, 2D surfaces (planimetric, transverse and longitudinal), were obtained with use of an experimental numerical algorithm, developed in C ++. Then, all the 2D surfaces were exported to “.dxf” format and subsequently, imported into Autodesk RECAP 360. After this step, the unification of the 2D surfaces was performed and then imported in Revit.

4.3 SCAN TO FEM

Hu, et. al., 2012 proposed numerical modelling for landslide analysis based on scans with LIDAR. The paper extends literature on manual and automatic approaches for converting data from point clouds to FEM numerical models. The manual model conversion presented in this work required only an effective software that can export file formats such as “dxf”, “acis”, or “iges” (AutoCAD) but it did not enable fitting to 3D model conversion. The presented automatic model conversion approach consisted in programming a Python code. After successfully reading the “inp” file, the complete numerical model was successfully imported in Abaqus for a comprehensive FEM simulation.

A highly relevant contribution to this field is proposed by Fernandez, et. al., 2016. The paper suggests numerical model development from 3D scans applied to corroded steel bars, in order to investigate the failure process and local effects on the pits, which are responsible of the variation of the mechanical properties in corroded steel reinforcement. 3D models were useful to observe and measure the local effects on the pits. With the application of this method, it was possible to analyse the local effects of steel corrosion produced on the bar by means of the outer surface description with a very high definition. The use of this technique opened a broad range of possibilities such as: statistical analysis of the pitting distribution, 3D solid modelling of the entire bar giving insight to local effects such as stress concentration and multiaxial stress distribution. DIANA finite element

software combined with the pre and post processor GiD were used for the numerical analysis. The 3D scanning of the corroded bars was done by means of an industrial stereo device with two cameras of 5 MP. The technique allowed to describe the imperfections over the steel bar surface due to corrosion. A correction of the measurement inaccuracies and data treatment were done using the post processing software Geomagic Wrap 2014. A 3D model was developed based on the transformation of the triangular outer surface mesh from the 3D scan results into a solid tetrahedral elements mesh. To proceed with the conversion, a data post-processing of the initial mesh was performed. First, a treatment to the surface mesh was done aiming at reducing the initial number of elements at the surface. Once the solid volume was created using the pre-processor GiD, it was possible to create a NURBS surface from which the tetrahedral solid mesh was generated. The 3D study of the bar permitted to understand and identify the corrosion phenomena produced within the bar.

Angjeliu, et. al., 2020 developed a simulation model for Digital Twin applications in historical masonry buildings and presented the integration between numerical and experimental data. For this scope the application of the DT concept in the complex case of Milan Cathedral was considered. The finite element structural model of the Cathedral of Milan was obtained based on photogrammetric geometric measurements, extensive in situ survey (LIDAR) and other archive data. The model considers a parametric geometric modelling procedure, for the most complex parts of the system (the vaults with the arches and ribs, the vault surcharge), and a manual structural modelling for the other simpler elements from the geometric point of view (the piers, the walls, the iron ties). The research concluded that only if a semantic and structured procedure is followed during BIM modelling, is it then possible to extract valuable information for the development of numerical finite element structural models throughout adequate exporting formats (i.e. IFC, SAT, etc.). Otherwise, the geometric model should be developed completely from the beginning, as it is usually done. Another area of interest was represented by the investigation of automatic reconstruction procedures, for the more complex parts of the structure. The analysis provided information on the distribution of the internal forces, displacements, and damage.

Barazzetti, et. al., 2015 proved that geometry encapsulated into dense point clouds can be accurately taken into consideration for FEA. The case study presented in this paper was Castel Masegra, a castle located in Sondrio, Italy. Complex elements (such as vaults) and structural anomalies (e.g. verticality) are turned into 3D surfaces by an intelligent node-to-node connection, obtaining models that can be used for static analysis. A set of tetrahedral meshes were generated to guarantee an adequate representation of the stress/strain distribution. Several problems were taken into consideration, such as the node-to-node correspondence (compatibility of the mesh), very distorted or small elements, and local imprecisions. These effects were successfully removed to obtain a consistent model for FEA. The paper proves that small errors and local inconsistencies lead to a failure during the simulation, as the continuity of the model is not guaranteed. The methodology for parametric model generation used for the castle was based on a

preliminary separation between simple and complex shapes. In the case of simple objects, the tools of most commercial software (Revit or Archicad) were shown sufficient. For the more complex shapes, vector profiles made up of NURBS were used to provide a curve network for NURBS surfaces, which were then turned into parametric BIM objects. Then, a rationalization of the BIM was carried out to generate a robust and reliable finite element model for structural simulation in Midas FEA.

Castellazzi, et. al., 2015 proposed a new semi-automatic procedure, called CLOUD2FEM, to transform three-dimensional point clouds of complex objects to finite element models. Cloud2FEM is a Python-based software. Its graphics were developed with the help of the PyQt5 library, supplemented by the PyQtGraph library, for 2D plotting and editing, and by the VisPy library for 3D visualization. A laser scanner survey of a complex building has been presented and applied to study a fortress damaged by the 2012 Emilia earthquake. The described procedure begins with a 3D analysis divided into sequential steps. At the end of this first part, the building is described with a dataset of slices, each containing bi-dimensional points. These are subsequently analysed in a 2D environment individually, and this phase includes some semi-automatic or manual analysis. Each pixel grid, obtained from the corresponding slice, contributes to the creation of the voxel model. The voxelized volume is then exported into 3D solid hexahedron-based FE meshes („inp.”file format). To assess the accuracy of the proposed FE model, a linear natural frequency analysis was performed.

Zhao, et. al., 2017 presents a procedure for processing three-dimensional point clouds that are generated from laser-based scanning of a cold-formed steel member into useful measurements of cross-section dimensions and imperfections, as well as for use in finite element simulations of the as-measured geometry. Multiple passes on the target cold-formed steel specimen using a line laser were registered with an iterative closest point algorithm to develop the initial three-dimensional point cloud. A novel feature recognition method was proposed to distinguish and extract geometric characteristics such as corners and flats in the targeted specimen. Post-processing was divided in two steps: surface registration, and feature recognition. Surface registration was shown critical in reconstructing the 3D models of the cold formed steel elements. The used method for this step was the iterative closest point algorithm. For the feature recognition step (corners, flat portions) the Harris detector was implemented. The concept of iterative closest point algorithm relies on matching some reference data (assumed correct) with target data. Based on the mentioned algorithm the 3D shell models were obtained successfully. The feature recognition presented an important role in removal of outlier points, corner point detection and determination of corner regions. The paper demonstrated the use of laser scans for dimension control providing comparisons to manual measurements and nominal manufactured specifications, in case of cold formed elements. Another important application identified by the authors included geometric imperfection measurement and shell finite element modelling in Abaqus. For this scope, a centreline model was created by projecting it on the registered point cloud through normal vectors.

Xu, et. al., 2023 proposed a novel method and modelling technique for determining the initial geometric imperfection of steel members using 3D scanning. A handheld 3D laser scanner was employed to generate 3D point-cloud model, and a computer software of data processing algorithm (3D Pr.) was developed to convert the 3D point-cloud model to actual digital geometric model. The presented algorithm (3D Pr.) has proven able to convert the initial point cloud into slices of sections before directly evaluating the local and global imperfection modes. After that, the geometric models were imported in a FE analysis software (ANSYS) as regenerated nodes obtained with another developed algorithm (CRSC). The nodes were found valid for generating solid and shell elements in ANSYS. Upon comparison, it was found that the results determined from the new modelling method were close to those values obtained from the experimental test, while the traditional modelling method (first-order mode from buckling analysis) was found to be more conservative.

5 INITIAL GEOMETRIC IMPERFECTIONS OF STEEL ELEMENTS: METROLOGY AND NUMERICAL MODELLING

As shown in the previous chapter, a relative novel application for 3D scans is the acquisition of initial geometric imperfections of steel elements (Zhao, et. al., 2017 and Xu, et. al., 2023). The above-mentioned application was also one of the main study objectives of the current thesis and will be presented also in the framework of an own study-case. Generally, it is well known that initial geometric imperfections can significantly affect the strength and stability of steel members.

Accounting global and local imperfections in the analysis stage of a numerical model can be done by either:

- Modelling the global and/or local imperfections explicitly in the model;
- Applying equivalent geometric imperfections;
- Using the buckling mode shapes as initial geometry.

The European norm **EN 1993-1-1: Design of steel structures - Part 1-1: General rules and rules for buildings** (EN 1993-1-1: Design of steel structures - Part 1-1: General rules and rules for buildings) requires frame and member imperfections (global and local) to be accounted for either in the analysis stage or in the design stage.

For global analysis of steel structures, the first critical buckling mode may be investigated and applied as imperfection shape for GNIA (geometrically non-linear analysis with imperfections). The amplitude of the shape (e_{0d}) shall be determined from EN 1993-1-1, equation 5.10, securing required reliability in most axially stressed cross section. The global imperfection in sway mode (Φ) and local geometric imperfections (e_{0d}) of individual members are introduced as:

- Global sway imperfections Φ (Figure 48);

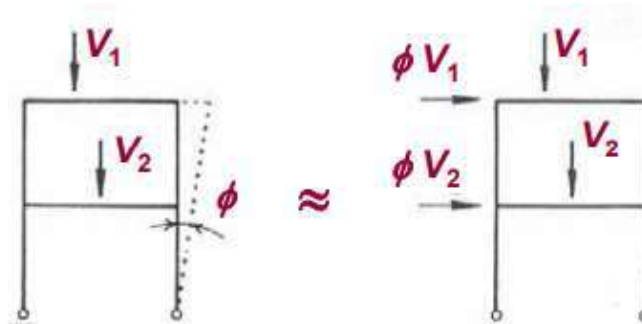


Figure 48 – Global sway imperfections

The values of Φ are given in equation 5.5. The global sway imperfections are introduced into analysis as corresponding horizontal loads as depicted in Figure 48.

- Referring to local imperfections, these are defined in EN 1993-1-1 as **bow imperfections** (they consider the local effect of member imperfections on a single element, column and/or beam).

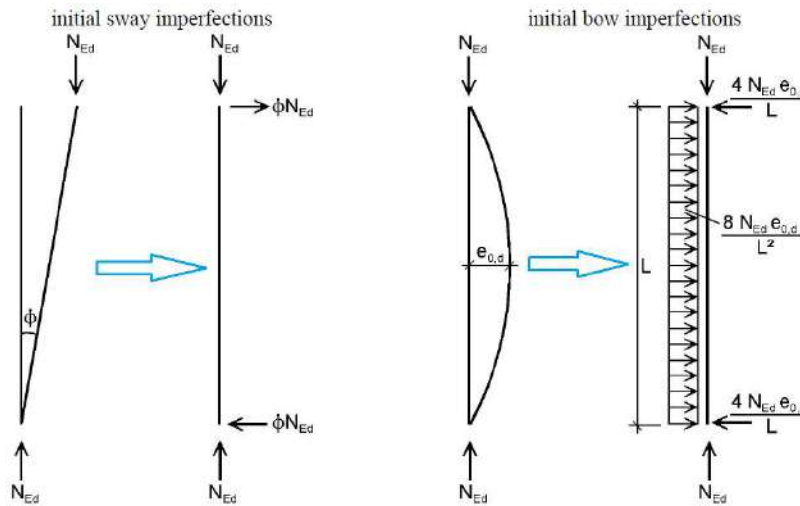


Figure 49 – Local imperfection assessment for columns (EN 1993-1-1)

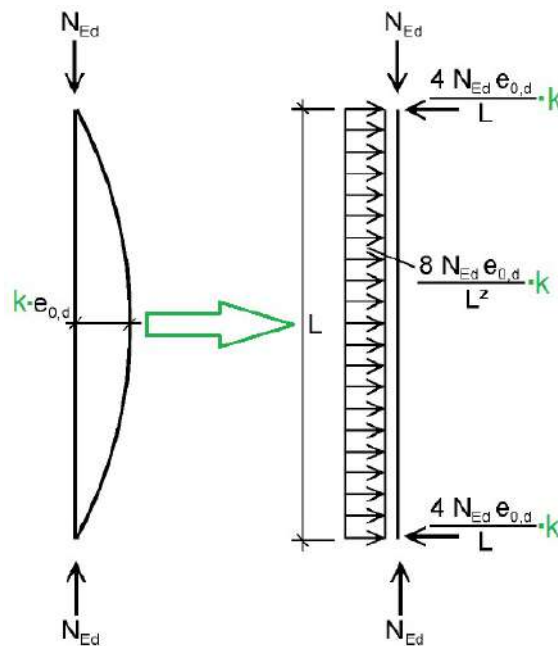


Figure 50 – Local imperfection assessment for beams (EN 1993-1-1)

In the case of columns, the equivalent horizontal forces applied to simulate the effects of imperfections are proportional to the compression force N_{Ed} . If N_{Ed} is a traction force for a given combination, then there are no local bow imperfections on this column for that combination. The equivalent static forces simulating the local bow imperfections on beams are computed similar to the columns, based on the axial force, and affected by the coefficient k . The e_0/L values are given in Table 5.1 of EC3, which depend on the buckling curve of the cross section. Furthermore, the effects of the deformed geometry of the structure may be considered by means of non-linear analysis with large displacements (2nd order analysis).

In case of member imperfections, their influence is generally covered by reduction factors (in columns and beams by χ , respectively χ_{LT}). In the case when a GNIA (geometrically nonlinear analysis with imperfections) is used, the imperfections or critical shape must be considered with amplitudes.

The new **prEN 1993-1-14: Design of steel structures — Design assisted by finite element analysis** (prEN 1993-1-14: Design of steel structures — Design assisted by finite element analysis) purposes that where imperfections are included in a FE model, they should account for the effects of geometric deviations from the perfect shape, residual stresses, and boundary condition defects. The pre-normative document presents the following types of imperfections that may be applied:

- **geometric imperfections** (section 5.4.2) and **additional residual stresses due to fabrication** (section 5.4.3);
- **equivalent geometric imperfections** (section 5.4.4) by modification of the perfect shape of the structure.

The equivalent imperfections are intended to cover the effect of both the geometric imperfections and the residual stresses and have larger magnitudes than solely geometric imperfections. Geometric imperfections or equivalent geometric imperfections may be defined in the FE model in the following ways:

- a) **measured imperfection shape of the structural element** (only permitted for geometric imperfections),
- b) **imperfection shapes** based on the functions defined in section 5.4.4, or modification of the perfect shape by a **predefined displacement** (permitted for both geometric and equivalent geometric imperfections),
- c) **imperfection shape based on linear bifurcation analysis** (LBA) corresponding to the **eigenmode** (shape) associated with the **expected failure mode** or to a **combination of eigenmodes** (permitted for both geometric and equivalent geometric imperfections).

The pre-normative document also states that, if geometric or equivalent geometric imperfections are used in a non-linear analysis, imperfections corresponding to each investigated buckling mode should be adopted. The most detrimental imperfection (that could realistically occur) should be chosen in calculating each potential failure mode. If the choice of this mode is not clear, several imperfection shapes and combinations should be investigated.

If more than one geometric or equivalent geometric imperfection form is used, combinations of these forms should additionally be considered. Rules for the Formulation of such combinations depend on the type of structure: frames, plated structures, cold-formed or shell structures. Rules are defined in section 5.5 of the document.

The equivalent geometric imperfections are classified into the following sub-groups:

- equivalent geometric imperfections for global structures (e.g. frames),
- equivalent geometric imperfections for structural members,
- equivalent geometric imperfections for cross-sections (plates),
- equivalent geometric imperfections for shell structures.

These equivalent imperfections may be used, unless a more refined analysis of both the member geometric imperfections and the full structural imperfections is performed. Equivalent geometric imperfections for use in geometrically and materially non-linear analysis (GMNIA) of structural members for flexural buckling may be determined from the following formula:

$$e_0 = \alpha \times \frac{L}{150} \text{ but } e_0 \geq L/1000 \quad (14)$$

where:

- L is the member length;
- α the imperfection factor, taken from EN 1993-1-1 or EN 1993-1-4

The equivalent imperfection shape may be either a bow (half-sine wave) or buckling mode. Equivalent geometric imperfections for use in geometrically and materially non-linear analysis (GMNIA) of structural members for lateral torsional buckling may be determined from the next formula:

$$e_0 = \alpha \times \beta_{LT} \text{ but } e_0 \geq L/1000 \quad (15)$$

where:

- α is the imperfection factor for minor axis flexural buckling, taken from EN 1993-1-1 or EN 1993-1-4,
- β_{LT} is the reference relative bow imperfection for lateral torsional buckling according to Table 5.4 to be applied lateral to the plane of bending.

In Figure 51 and Figure 52 are shown the equivalent geometric imperfections for structural members for lateral torsional buckling, respectively the equivalent geometric imperfections for cross-sections of plated structures.

Shape	β_{LT}
bow	combination of 1/150 (half-sine wave) and 1/215 (full sine wave)
buckling shape	1/150

Figure 51 – Equivalent imperfections for lateral torsional buckling

Component/type of imperfection	Shape	Magnitude
longitudinal stiffener with length a	bow	$\min(a/400, b/400)$
panel or sub-panel with short span a or b	buckling shape	$\min(a/200, b/200)$
stiffener or flange subject to twist	bow twist	$1 / 50$
outstand elements for cold-formed structures – local	buckling shape	$b / 125$
outstand elements for cold-formed structures – distortional	buckling shape	see Formula (5.17)

Figure 52 – Equivalent imperfections for cross-sections of plated structures

For distortional buckling mode, the imperfection magnitude mode may be determined by:

$$e_{0,dist} = 0.3 \times t \times \sqrt{f_{yb} \times \sigma_{cr,d}} \quad (16)$$

where:

- t is the thickness;
- f_{yb} is the basic yield strength according to EN 1993-1-3;
- $\sigma_{cr,d}$ is the elastic critical distortional buckling stress.

The pre-normative document suggests that equivalent geometric imperfections may also be substituted by appropriate equivalent forces acting on the member. The equivalent force for a frame imperfection and for a member bow imperfection may be chosen according to EN 1993-1-1.

There are also given recommendations for design by GNIA analysis in combination with LBA analysis and design by GMNIA analysis. The design by GNIA analysis in combination with LBA method involves a global stability check of the complete structure using global equivalent geometric imperfections and performing a GNIA analysis. If the geometrically non-linear – second order – effects in individual members or certain individual member imperfections are not fully included in the global analysis, the individual stability of members should be checked according to the relevant criteria given in EN 1993-1-1.

GMNIA (geometrically and materially non-linear analysis with imperfections) may be used to determine the behaviour of the structure represented by a load-displacement path related to the chosen boundary conditions and analysed load case combination. In a GMNIA analysis, the effects of geometric imperfections and also residual stresses should be considered. Geometric imperfections and residual stresses may be separately applied to the FE model or covered together by equivalent geometric imperfections. Eigenmode-affine equivalent geometric imperfection may be also used.

Generally, as depicted above from the two standards, the traditional modelling methods may lead to unreliable results. An alternative is represented by modelling the real geometric imperfections. The real geometric imperfections need to be measured directly on the steel member. In the past, imperfection measurements were generally carried out with contact instruments, such as a dial gauge, and dimensions were manually measured with callipers and micrometres. These modes of measurement can only provide a sparse

representation of the actual imperfect geometry. Statistical summaries of available imperfection data from these methods focus only on maximum imperfections and due to these limitations, it is necessary to investigate other methods of acquiring the real geometric imperfections.

A relative novel method for obtaining the full-filled initial geometric imperfection of steel members was investigated in this thesis, based on 3D non-contact scanning techniques, and applied in the case study presented in the following chapter.

6 IMPERFECTION MEASUREMENTS OF STAINLESS-STEEL LINKS

6.1 GENERAL DESCRIPTION

The following case study is part of the HYLINK research project that aimed to develop and experimentally validate a stainless steel replaceable link solution for eccentrically braced frames with self-centring capability.

High-intensity seismic events can cause major human and financial losses, the latter including damage of structures, whose rehabilitations costs are exaggerated compared to the initial construction investment. A possible solution is represented by "damage-limitation" systems, characterized by controlled structural damage that can be easily repaired. In recent decades, several strategies have been developed to reduce the economic losses due to earthquakes, an approached concept being represented by the dual structures with eccentrically braced frames and replaceable links (EBF) combined with moment resisting frames (MRF). This system, proposed by Stratan, 2003, investigated experimentally by Stratan, et. al., 2004 and numerically by Dubina, et. al., 2008 at the Politehnica University Timișoara, ensures the concentration of residual deformations in the replaceable links. Thus, the post-earthquake repair and consolidation works are limited to the replacement of the links, and the re-centring of the structure takes place through the elastic forces in the MRF's. Among the advantages of dual hysteretic structures are worth mentioning the intrinsic stability, relatively low costs of design, implementation, and maintenance. However, the solution with removable links is not perfect. According to studies conducted by a group of researchers of the Department of Steel Structures and Structural Mechanics from Politehnica University Timisoara, short-link structures made from conventional steel grades, have the disadvantage represented by a very high ductility demand, and an increased over-strength factor due to the link consolidation phenomenon, imposing time-consuming design calculations for the non-dissipative elements of the structure (Chesoan, et. al., 2018; Stratan et al., 2004). To eliminate these limitations induced by the mentioned disadvantages and to ensure economic efficiency of the solution, it was proposed to introduce a new typology of links, which could extend their scope by exploiting the advantages of stainless steel.

Within the HYLINK research project, an innovative link solution was developed for seismically resilient metal structures with re-centring capacity. The investigated solution exploits the potential of using stainless steel in the manufacture of replaceable links, which stand out for their superior ductility and tenacity characteristics in comparison with common steel used in construction. Although stainless steel is considerably more expensive than ordinary steel, due to its use in a limited number of components (links), the total price of the construction does not increase significantly. The replaceable stainless-steel link, developed and validated numerically and experimentally in the mentioned project, is the key component of a seismically resilient construction and has the potential for superior seismic performance.

In the framework of this research program, and for the scope of this thesis, it was proposed to investigate the initial geometric imperfections with the use of 3D scanning technology and implementing them in the numerical modelling of the links for validation of the experimental tests.

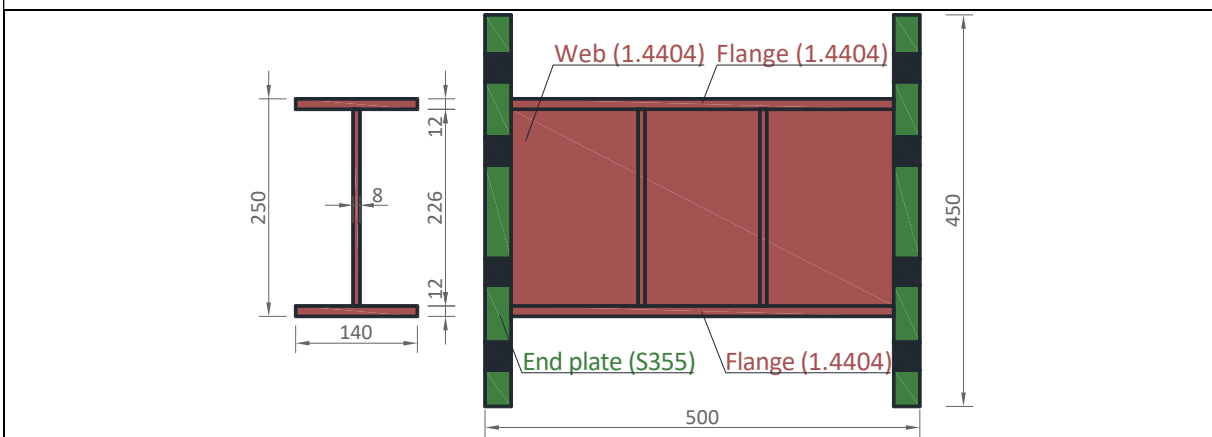
6.2 EXPERIMENTAL SPECIMENS AND TEST SETUP

The test specimens that were investigated are presented in Table 6. A total number of 3 links, with and without stiffeners were subjected to cyclic tests. A schematic and a typical longitudinal section view of a link is illustrated below.

Table 6 – Nomenclature of the links tested in the experimental program

Nomenclature	Stiffened sides	Steel grade	Dimensions	Loading protocol	No. of specimens
S-C	0	1.4404	250x140x12x8	Cyclic	1
S-2DS-C1	2	1.4404	250x140x12x8	Cyclic	1
S-2DS-C2	2	1.4404	250x140x12x8	Cyclic	1

Cross-section illustration



6.2.1 EXPERIMENTAL SETUP

The experimental test setup consists of several subassemblies:

- the **experimental rig** itself, i.e. eccentrically braced frame with replaceable links. This EBF comprise 2 bottom-pinned columns, the upper hinged beam, and the rigid beam with braces,
- the **reaction wall** which allows performing quasi-static testing by supporting actuators which apply load on the structure. This reaction wall has a considerably higher resistance than the tested structure, while its deflections are several orders of magnitude lower than those measured on the structure itself;
- the **servo-controlled hydraulic actuator** of ~1000 kN, equipped with hydraulic unit, controller and spherical hinges which prevent any equipment failure caused by exerting additional forces in the piston rod. The actuator imposes the displacement at the top of the left column of

- the EBF by means of a steel transfer piece. The actuator has a stroke of $\pm 375\text{mm}$ for cyclic loading, respectively 750mm for monotonic loading.;
- the **strong floor** which serves to support the structure itself. This strong floor is provided with a system of holes located in a rectangular pattern at intervals between 0.25 and 1.0 m;
 - the **system of guide girders**, columns, braces and slipping bearings, which ensure the stability of the experimental rig by allowing in-plane displacement and restraining out-of-plane displacements of the structure.

The experimental setup is presented in Figure 53.

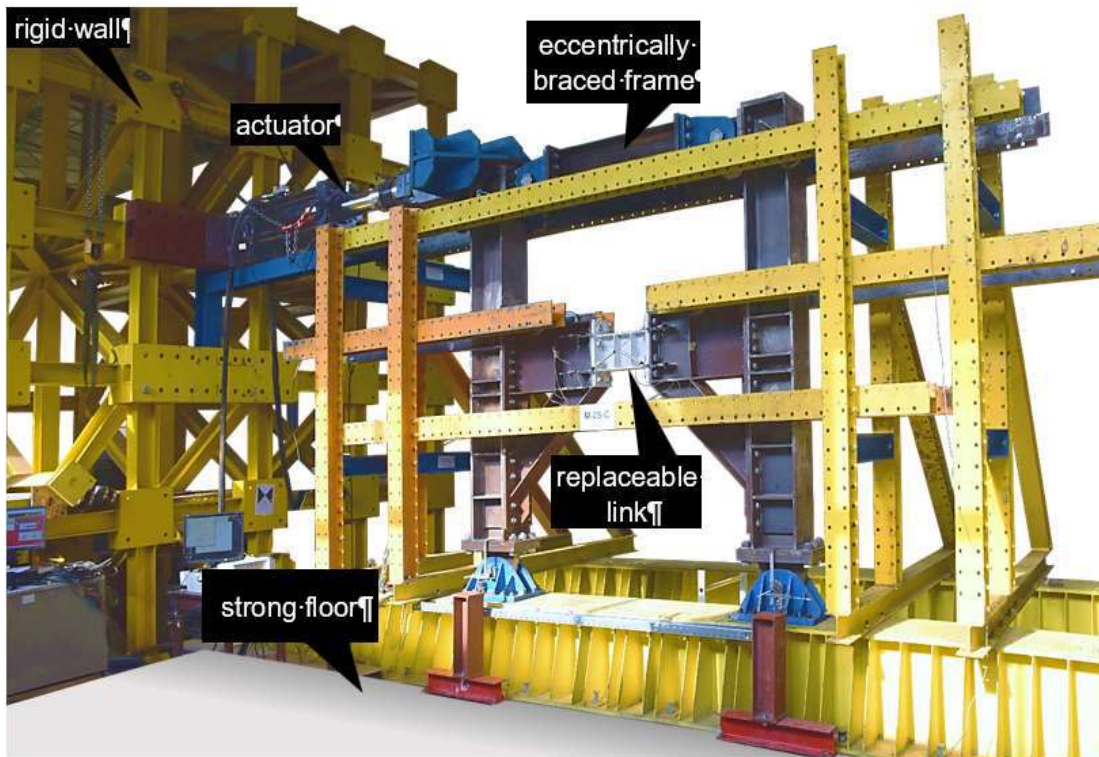


Figure 53 – Cyclic loading protocol for replaceable links

6.2.2 CYCLIC LOADING PROTOCOL

The requirements for performing cyclic tests on links are provided in the section K2.4c of the American National Standard ANSI/AISC 341-16 „Seismic provisions for structural steel buildings”. It is specified that the cyclic tests on links shall be conducted by controlling the total link rotation angle γ_{total} , imposed on the test specimen, as follows:

- 6 cycles at $\gamma_{\text{total}} = 0.00375$ rad
- 6 cycles at $\gamma_{\text{total}} = 0.005$ rad
- 6 cycles at $\gamma_{\text{total}} = 0.0075$ rad
- 6 cycles at $\gamma_{\text{total}} = 0.01$ rad
- 4 cycles at $\gamma_{\text{total}} = 0.015$ rad
- 4 cycles at $\gamma_{\text{total}} = 0.02$ rad
- 2 cycles at $\gamma_{\text{total}} = 0.03$ rad

- 1 cycle at $\gamma_{total} = 0.04$ rad
- 1 cycle at $\gamma_{total} = 0.05$ rad
- 1 cycle at $\gamma_{total} = 0.07$ rad
- 1 cycle at $\gamma_{total} = 0.09$ rad
- continue loading at increments of $\gamma_{total} = 0.02$ rad, with one cycle of loading at each step.

Consequently, the cyclic loading protocol involves several deformation-controlled cycles to failure. The applied protocol is plotted in absolute values of link rotation γ_{total} in Figure 54.

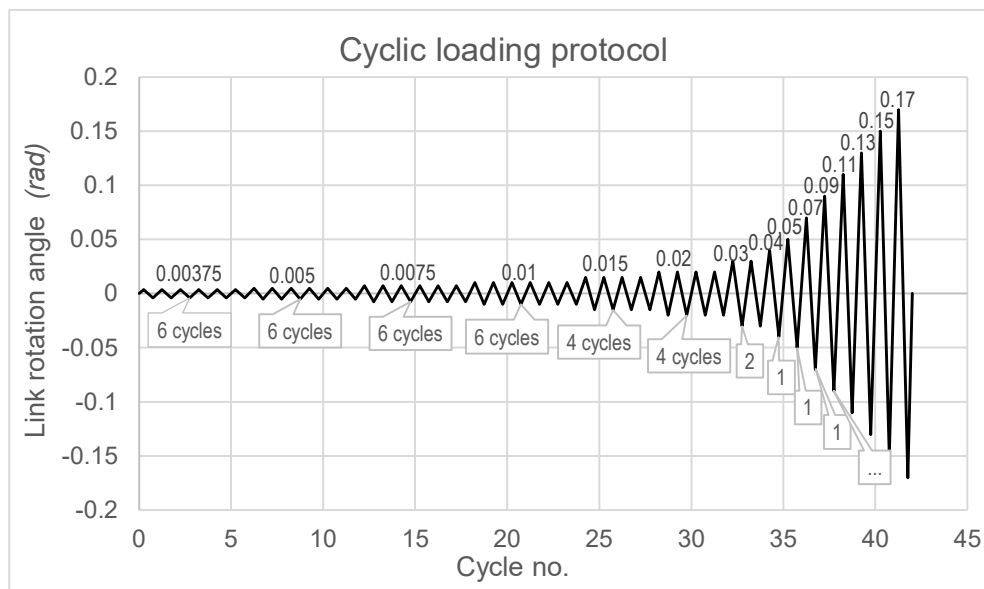


Figure 54 – Cyclic loading protocol for replaceable links

6.2.3 TIGHTENING OF THE PRELOADED BOLTS

According to §8.5 from EN 1090-2:2008, for the bolts quality class HV with bolt diameter equal to 27 mm and calibration condition of K1 class, a combined tightening method should be applied, method which comprises two steps:

- 1) initial tightening step, using a torque wrench, set to a torque value of about $0,75 M_{r,i}$ with $M_{r,i} = M_{r,2}$ or $M_{r,1}$ or $M_{r,test}$. This first step shall be completed for all bolts in one connection prior to commencement of the second step. When using $M_{r,1}$, for simplification:

$M_{r,1} = 0,13 \cdot d \cdot F_{p,C}$ may be used, unless otherwise specified.

For these bolts, the nominal minimum preloading force is $F_{p,C} = 321$ kN.

$M_{r,1} = 0,13 \cdot d \cdot F_{p,C} = 0,13 \times 27 \times 321 \times 1000 = 1126710$ Nmm = 1.126.71 Nm

$0,75 \times M_{r,1} = 0,75 \times 1126,71 = 845,032$ Nm

- 2) a second tightening step in which a specified part turn is applied to the turned part of the assembly. The position of the nut relative to the bolt threads shall be marked after the first step, using a marking crayon, or marking paint, so that the final rotation of the nut relative to the thread in this second step can be easily

determined. The second step shall be in accordance with the values given in Figure 55, unless otherwise specified. Hence, the nominal thickness of the parts to be connected (including all packs and washers) is $t = 25+25+5+5 = 60 \text{ mm}$, and bolt diameter is $d = 27 \text{ mm}$.

EN 1090-2:2008 (E)

**Table 21 — Combined method: additional rotation
 (8.8 and 10.9 bolts)**

Total nominal thickness "t" of parts to be connected (including all packs and washers) $d = \text{bolt diameter}$	Further rotation to be applied, during the second step of tightening	
	Degrees	Part turn
$t < 2d$	60	1/6
$2d \leq t < 6d$	90	1/4
$6d \leq t \leq 10d$	120	1/3

NOTE Where the surface under the bolt head or nut (allowing for taper washers, if used) is not perpendicular to the bolt axis, the required angle of rotation should be determined by testing

Figure 55 – Combined tightening method parameters, acc. to EN 1090-2:2008

6.2.4 INSTRUMENTATION AND DATA ACQUISITION

As shown in Figure 56 the instrumentation for the experimental setup comprises 2 types of transducers, as required by data acquisition for an exhaustive engineering understanding of the motion of the entire setup, as well as of the local response of the dissipative zones particularly:

- 1) the **local instrumentation** of the experimental specimens comprises 10 local displacement transducers: DT1 and DT2 to monitor the total link deformations, D1 and D2 to monitor only web panel deformations, DC1 to DC4 to monitor connections' rotations and DS1 and DS2 to monitor slips in connections (Figure 57);
- 2) the **global instrumentation** consists of 6 global displacement transducers to monitor the global displacements of the setup: horizontal (DH1 and DH2) and vertical (DV1 and DV2) slips in both columns' bottom pins, lateral top displacement of the setup (DHT) and relative horizontal top displacement between the two columns (DHR).

It is worth mentioning that the links, as potential dissipative areas, were white painted in order to visually capture the yielding process. Additionally, on the upper flange of the links were also black speckles applied for VIC measurements (Figure 58).

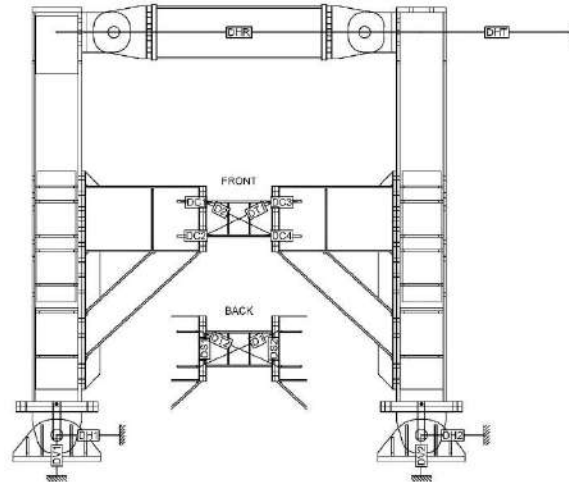


Figure 56 – Instrumentation of the experimental setup

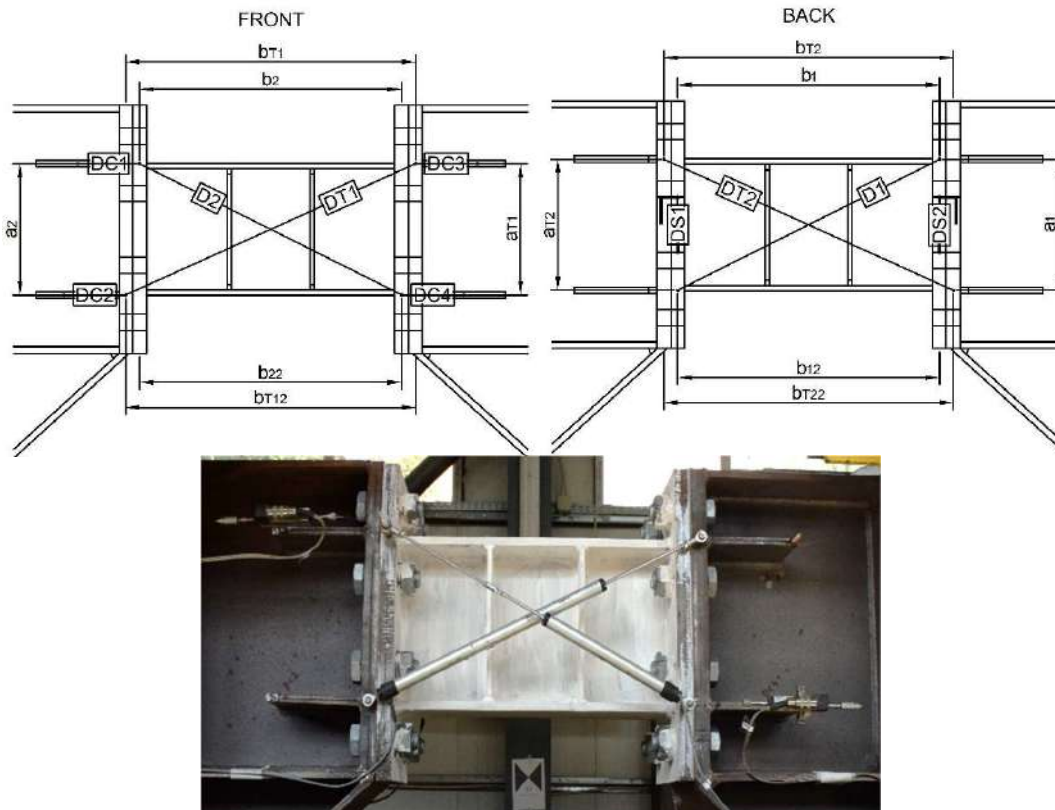


Figure 57 – Local displacement transducers layout on the link

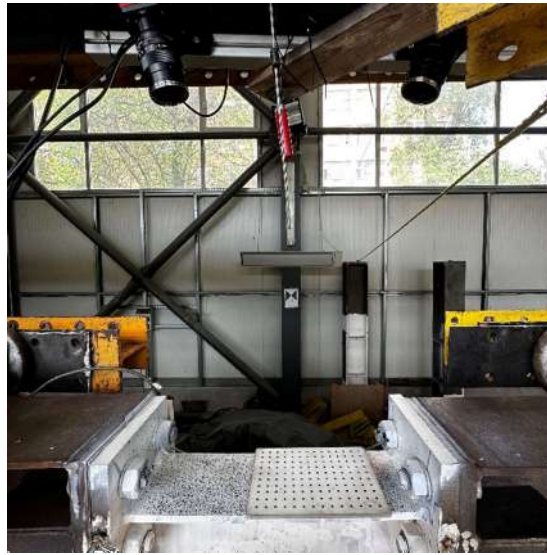


Figure 58 – VIC system setup

6.2.5 EXPERIMENTAL DATA PROCESSING

The experimental program output data are expressed through the relationship between two parameters: link shear force and link rotation. The **shear force** in links can be processed using the following relationship:

$$V = FA \cdot \frac{H}{L} \quad (17)$$

where:

FA is the actuator force,

H and L are the dimensions of the eccentrically braced frames, according to Figure 59.

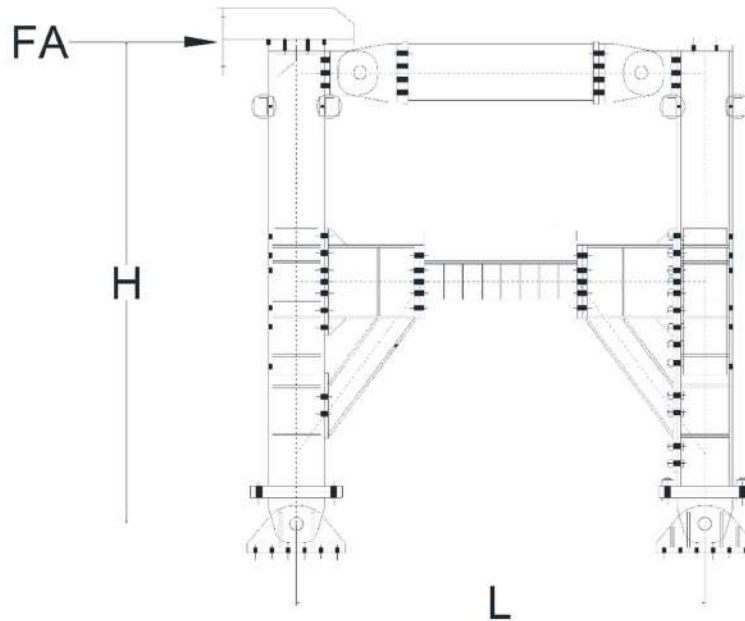


Figure 59 – Geometry of the test setup

The **total link rotation** γ_T was computed directly based on the link instrumentation recordings (Raport științific și tehnic, Etapa 3: Încercări experimentale pe îmbinări sudate și linkuri, și elaborare recomandări de proiectare pentru linkuri hibride “HYLINK”, 2022):

$$\gamma_T = \frac{2 \cdot \sqrt{a_T^2 + b_T^2} \cdot (DT2 - DT1) + (DT2^2 - DT1^2)}{4 \cdot a_T \cdot b_T} \cdot \frac{b_T}{e} \quad (18)$$

where:

$DT1$ and $DT2$ – total link deformations;

e - link length

a_T and b_T – relative distance for local displacement transducers, according to Figure 57.

To simplify the digital input and output computation, the previous relationship could be expressed as:

$$\gamma_T = \frac{x_T \cdot (DT2 - DT1) + (DT2^2 - DT1^2)}{y_T} \quad (19)$$

where:

$$x_T = 2 \cdot \sqrt{a_T^2 + b_T^2}$$

$$y_T = 4 \cdot a_T \cdot e$$

These parameters were determined for each specimen individually based on the setup measurements.

6.3 GEOMETRIC DIMENSION AND IMPERFECTION MEASUREMENTS

6.3.1 TRADITIONAL GEOMETRIC DIMENSION MEASUREMENTS

As in every experimental program, the first measurements that need to be done before the testing of the specimens are the geometric dimension measurements. Firstly, the specimens were measured manually with a tape measure, a calliper, and an ultrasonic thickness gauge (Figure 60). In Figure 61 are depicted the dimensions that were measured for the three specimens and the results are depicted in Table 7-9.



Figure 60 – Tools used for manual geometric dimension measurements

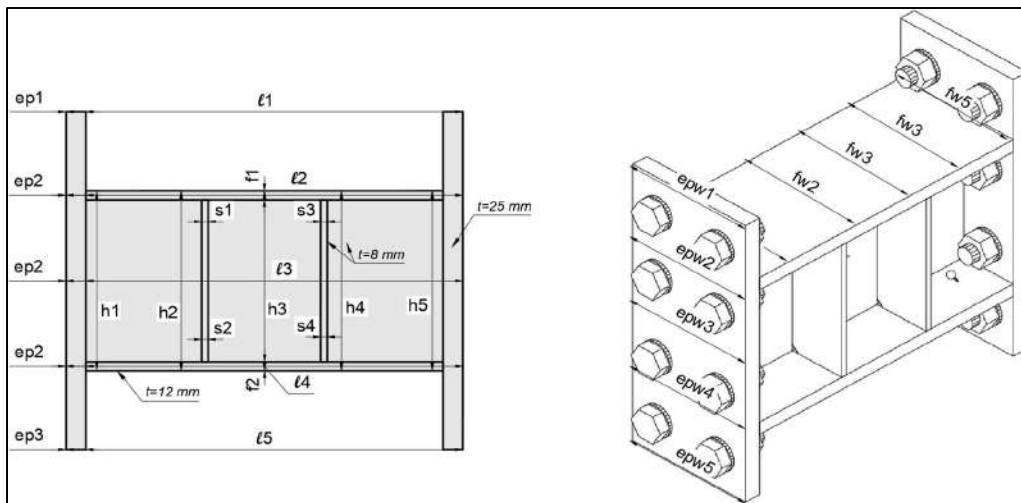


Figure 61 – Measured dimensions of the specimens

Table 7 – Dimensions of specimen S-C

ID	f1	f2	s1	s2	s3	s4	ep1	ep2	
S-C	front	12.01	12.02	-	-	-	-	25.00	25.01
	back	12.03	12.00	-	-	-	-	25.02	25.02
		I1	I2	I3	I4	I5			
	front	496	498	499	499	498			
	back	495	497	498	497	496			
		h1	h2	h3	h4	h5			
	front	249	244	242	242	248			
	back	249	245	244	246	248			
		epw1	epw2	epw3	epw4	epw5			
	left	200	200	200	200	200			
	right	198	198	198	197	197			
		fw1	fw2	fw3	fw4	fw5			
	top	140	140	140	140	139			
	bottom	139	140	140	140	139			
		w1	w2	w3	w4	w5			
		8.27	8.26	8.26	8.28	8.25			

Table 8 – Dimensions of specimen S-2DS-C1

D	f1	f2	s1	s2	s3	s4	ep1	ep2	
S-2DS-C1	front	12.01	12.01	8.03	8.03	8.05	8.06	25.02	25.02
	back	12.00	12	8.01	8.01	8.00	8.01	25.02	25.02
		I1	I2	I3	I4	I5			
	front	496	496	497	497	497			
	back	496	497	497	497	497			
		h1	h2	h3	h4	h5			
	front	250	248	248	249	250			
	back	250	249	249	249	250			
		epw1	epw2	epw3	epw4	epw5			
	left	198	199	198	198	198			
	right	198	198	198	198	198			
		fw1	fw2	fw3	fw4	fw5			
	top	139	139	139	139	139			
	bottom	139	139	139	139	139			
		w1	w2	w3	w4	w5			
		8.24	8.23	8.24	8.24	8.24			

Table 9 – Dimensions of specimen S-2DS-C2

ID		f1	f2	s1	s2	s3	s4	ep1	ep2	
S-2DS-C2	front	12.01	12.03	8.00	8.00	8.00	8.01	25.03	25.01	
	back	12.01	12.02	8.04	8.02	8.01	8.01	25.01	25.01	
		I1	I2	I3	I4	I5				
	front	495	497	496	496	495				
	back	497	498	499	498	498				
		h1	h2	h3	h4	h5				
	front	249	249	249	249	249				
	back	249	249	249	249	250				
		epw1	epw2	epw3	epw4	epw5				
	left	198	199	199	199	198				
	right	200	200	200	200	200				
		fw1	fw2	fw3	fw4	fw5				
	top	139	139	139	139	139				
	bottom	140	139	140	140	140				
		w1	w2	w3	w4	w5				
			8.28	8.24	8.25	8.2	8.21			

6.3.2 3D SCANNING FOR DIMENSION AND IMPERFECTION MEASUREMENTS

For the aim to measure the real geometric imperfections and the dimensions of the specimens, 5 different scanners based on 3 scanning principles (LiDAR, blue laser, and white structured light) were selected and applied to compare their workflow, accuracy, and time demand for obtaining the measurements. Two of the selected scanning devices were handheld (Creaform HandyScan3D, EinScan Pro HD) and implied to attach reflective targets on the specimens, one of the devices was equipped with a measuring arm and worked without targets (Hexagon Absolute Arm), and the last two were LiDAR based – a Terrestrial Laser Scanner (Z+F IMAGER 5010C) and a Smartphone (Iphone 14 Pro). In Table 10 are presented the applied scanners / specimen and in Table 11 are shown the principal technical specifications of each device.

Table 10 – Applied scanners / Specimen

Applied scanning device/ Specimen	S-C	S-2S-C	S-2S-C2
Z+F IMAGER 5010C	✓	✓	✓
HEXAGON Absolute Arm	✓	✗	✗
EinScan Pro HD	✗	✓	✓
CREAFORM HandySCAN3D	✗	✓	✓
IPHONE 14 PRO	✓	✓	✓

Table 11 – Technical specifications of the used scanners

Data acquisition device	Scanning technology	Scanner type	Accuracy (mm)	Data acquisition rate (pts/sec)	Stand-off distance (mm)
Z+F IMAGER 5010C	LIDAR	static	0.1	1.016 mill.	500
HEXAGON Absolute Arm	Blue laser	measuring arm	0.01	1.2 mill.	115
EinScan Pro HD	White light	handheld	0.04	3 mill.	500
CREAFORM HandySCAN3D	Blue laser	handheld	0.04	0.48 mill.	300
IPHONE 14 PRO	LIDAR	smartphone	10	-	100

To facilitate the scanning process from as many angles as possible, and to have access to the lower part of the specimens, the links were positioned on a work platform at an approximate height of 1.5 m. Next, the measurements performed with each scanner are presented below.

6.3.2.1 Hexagon Absolute Arm

The 7-axis blue laser scanner **Absolute arm (85 series)** from **Hexagon** used in this experiment, has a measurement volume of 1.2 m, an accuracy of 0.01 mm and is Laser class 2 (eye-safe).

The set-up of the device consists of:

- Laser scanner;
- Coordinate measuring arm (that calculates the exact position of the probe at each point through embedded encoders on each axis in the arm);
- Camera;
- Software (**Inspire**) that enables real time display of the scanning process on a connected laptop.

The measuring process can be mainly divided into 3 steps:

1. **Scanner calibration;**
2. **Moving the 3D scanner at a stable speed to obtain data points at all locations on the specimen;**
3. **Transmitting the data points to the post-processing software (Inspire).**

First, the device was manually calibrated, following which the accuracy of the calibration was verified on the specimen. To account for the different reflection behaviour of surfaces the camera exposure time was adapted. During the measurements it was mandatory to not change the initial position of the specimen and it is important to mention that the arm allows to measure just from a single station. The scanning time of one

specimen was evaluated at approximately 25 minutes. Because of the measuring arm that calculates the position of the laser probe in real time, it was not necessary to apply reflective targets on the specimens. In Figure 62 are presented some footages taken during the measurements.



Figure 62 – 3D Measurements with the Absolute Arm

As depicted in Figure 63 the laser probe needs to be positioned under an angle (not parallel) when scanning the edges of the specimens.



Figure 63 – Positioning of the laser probe for scanning the edges

It is worth mentioning that no special lighting or laboratory conditions are needed for this type of scanning.

Besides the post-processing functions of the **Inspire** software, it also facilitates during the measurements real-time display of the specimen. This was useful to identify unscanned areas or areas that required a rescan (Figure 64).

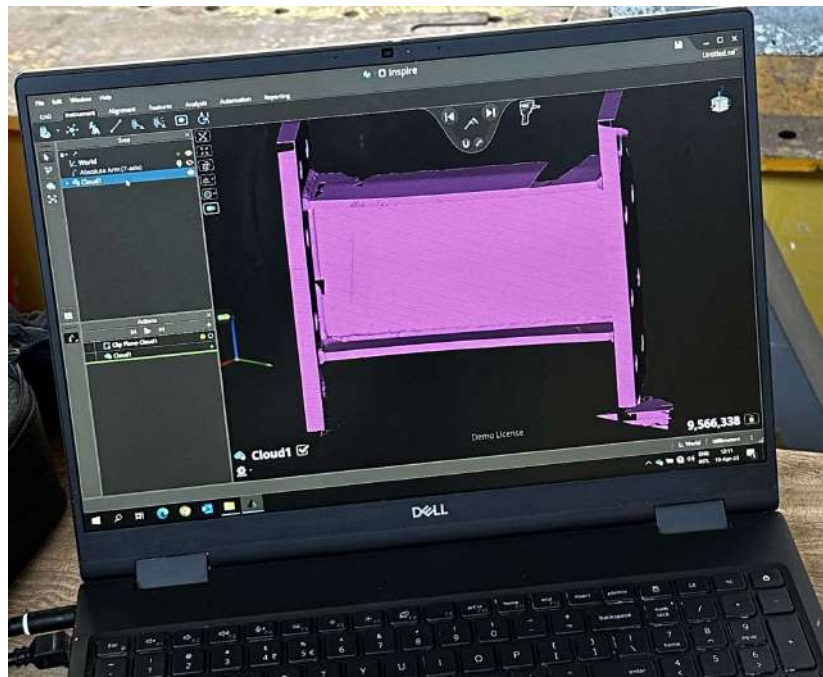


Figure 64 – Post-processing software and real-time display of the specimen (Inspire)

6.3.2.2 EinScan Pro HD

The EinScan Pro HD is a 3D handheld scanner that uses structured white light as measuring principle and has an accuracy of 0.045 mm. The set-up of the device consists of:

- Handheld white light scanner;
- Software (**Solid Edge SHINING 3D**) that enables real time display of the scanning process on a connected laptop.
- Reflective targets.

A schematic representation of the set-up is presented in Figure 65. The measuring process can be mainly divided into 4 steps: **scanner calibration**, **applying** randomly distributed **targets on the specimen**, **moving the 3D scanner** at a stable speed to **obtain data points** at all locations on the specimen surface, and **transmitting data points to the post-processing software**.

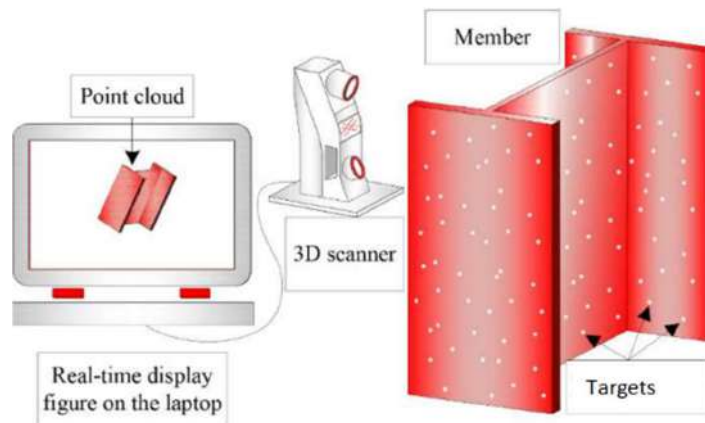


Figure 65 – Schematic representation of the EinScan Pro HD set-up

First, the device was manually calibrated with the calibration targets, following which the accuracy of the calibration was verified also on the specimen (Figure 66).

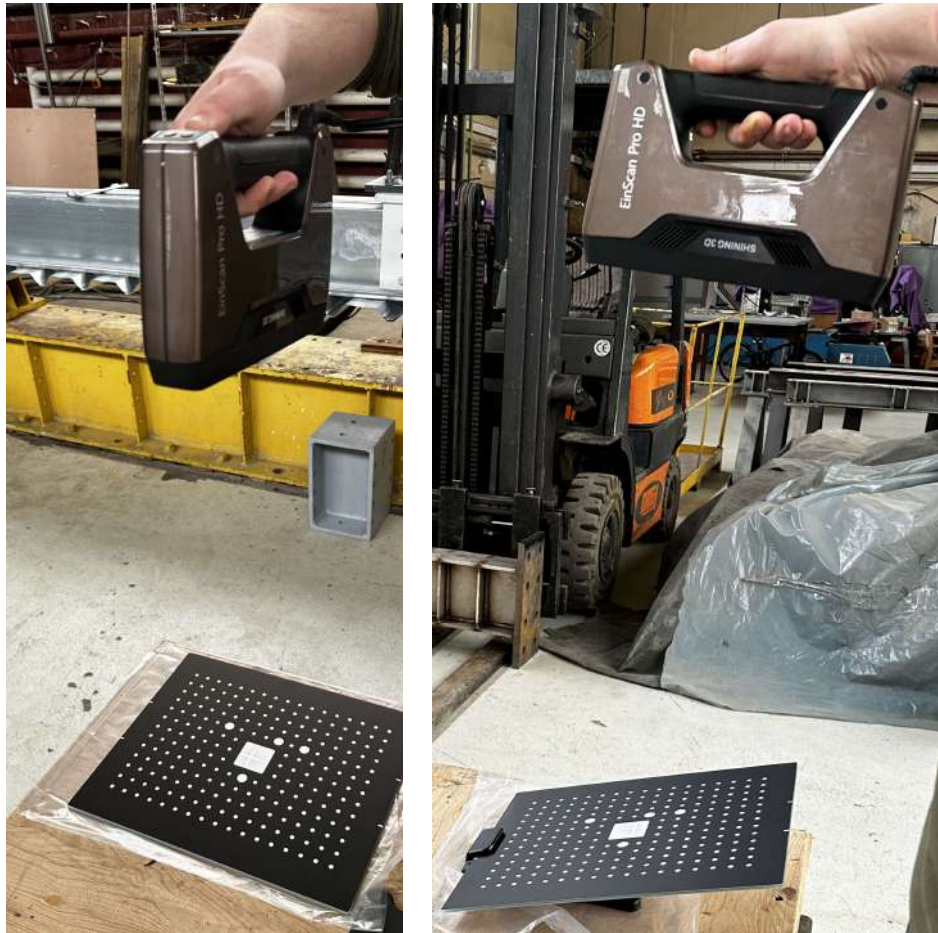


Figure 66 – Calibration of the structured light scanner

To account for the different reflection behaviour of surfaces on the specimens the brightness of the light source was adapted. The second step that was done before the actual scan is applying the reflective targets on the specimens to increase accuracy and repeatability of 3D data. The targets have also an important role in the final point cloud alignment and to facilitate a high precision measurement in case of reflective surfaces. The embedded software recognizes and then analyses each target in real time in every frame at up to 10 frames per second. It records the exact location of each target as they relate to each other and using that information aligns each frame to the following one. At any given time during scanning, the scanner needs to “see” minimum 3 markers in every frame. When it doesn't, scanning will automatically stop. Another important advantage of the use of targets, is that it allows to change the initial position of the specimen during the measurements and can lead to a more complete scan, although, applying tens of targets is time consuming. The user is able in this way to scan all the faces of the specimen, being one of the most important advantages of this technology. The scanning time of one specimen was evaluated at approximately 90 minutes, representing one of the major drawbacks of this technology. In Figure 67 is presented the scanning process with structured light.



Figure 67 – Scanning process with structured light

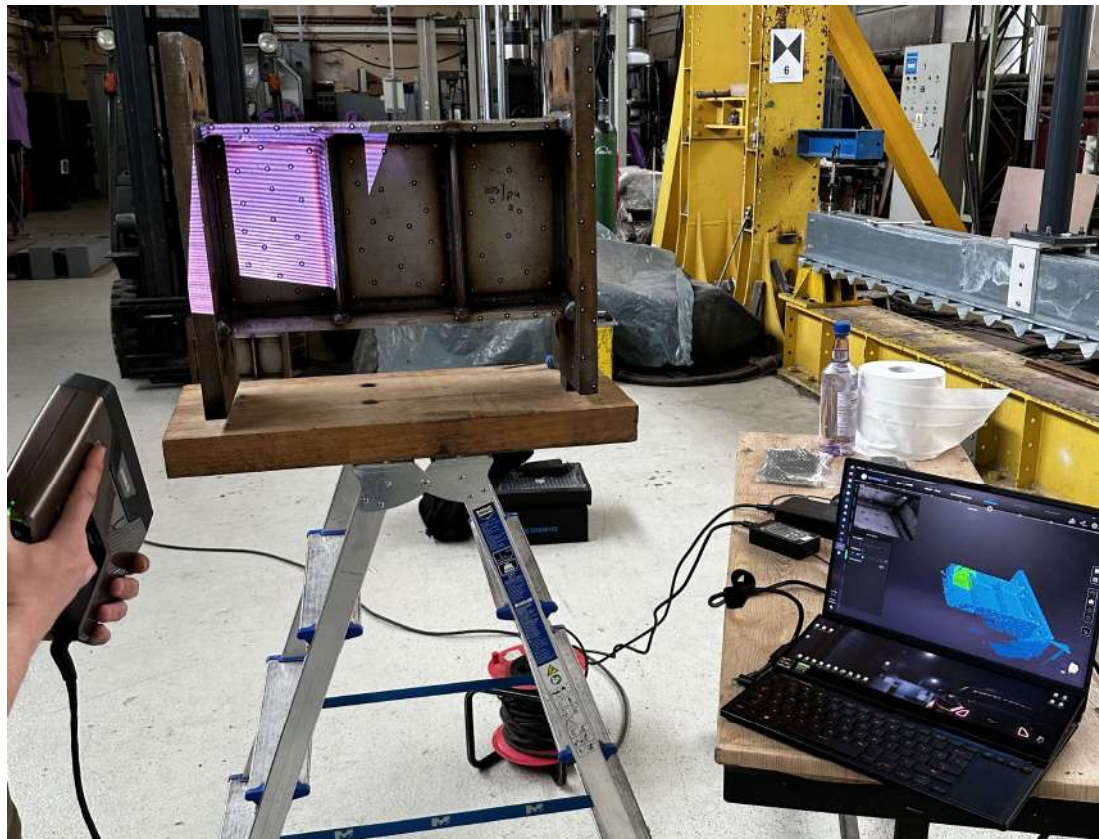


Figure 68 – Positioning of the structured light scanner towards the specimen

As depicted in Figure 68 the scanner needs to be positioned under an angle (not parallel) when scanning the edges of the specimens.

This type of scanner employs special lighting conditions, and it was mandatory to avoid direct sunlight on the specimens. Also, because the links have a highly reflective surface, the scanning process was more time-consuming and there were several areas that the scanner could not measure.

Besides the post-processing functions of the **Solid Edge SHINING 3D** software, it also facilitates during the measurements real-time display of the specimen. This was useful to identify unscanned areas, or areas that required a rescan and to control the brightness of the light source.

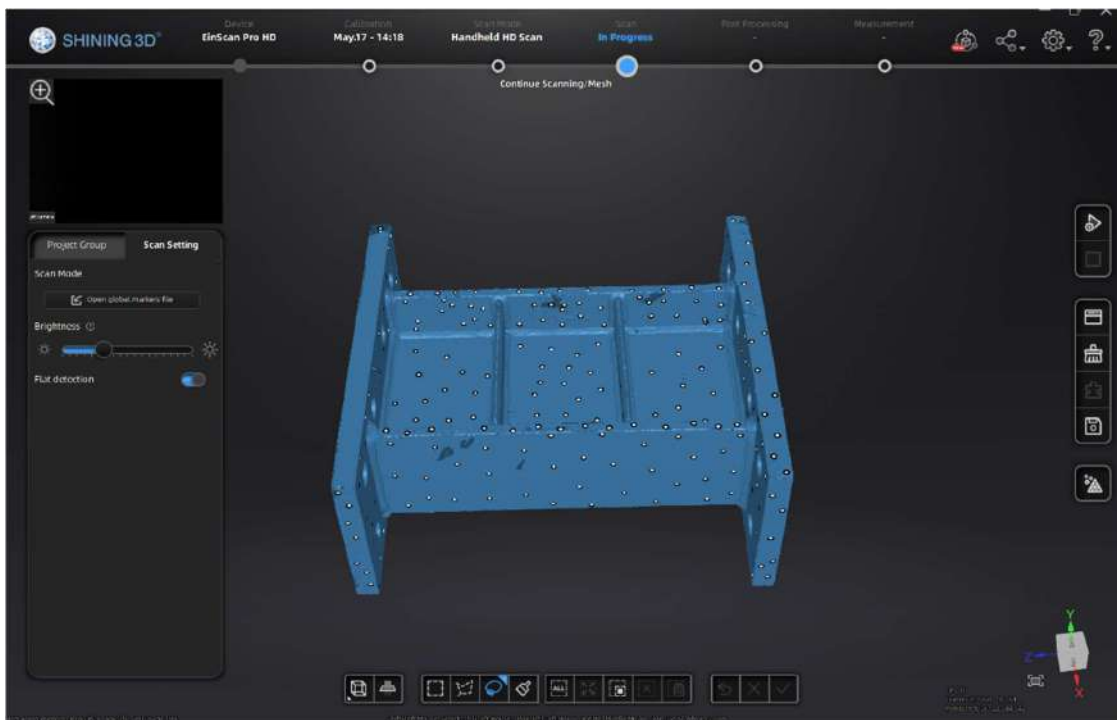


Figure 69 – Post-processing software and real-time display of the specimen (Solid Edge)

6.3.2.3 Creaform HandySCAN3D

The second handheld 3D scanner used in the experimental investigation is the HandySCAN3D Silver series from Creaform. This scanner uses the blue laser technology (laser class 2M – eye safe) and has an accuracy of 0.04 mm. Another important feature is the stand-off colour indicator that enables a higher scanning performance. The set-up of the device is similar to that presented for the handheld structured light scanner and consists of:

- Handheld blue laser scanner;
- Software (**VXelements**) that enables real time display of the scanning process on a connected laptop.

- Reflective targets.

The measuring process is also similar and is divided into 4 steps: **scanner calibration, applying** randomly distributed **targets on the specimen** (fewer targets are implied in comparison with structured light), **moving the 3D scanner** at a stable speed to **obtain data points** in all zones of the specimen and **transmitting data points to the post-processing software**.

After the manual calibration, the second step that was done before the actual scan is applying the reflective targets on the specimens. In this case, because of the performances of the blue laser technology, fewer targets were needed and an interesting method to facilitate the re-use of these was implemented as depicted in Figure 70. The targets were used in this case just in the final point cloud alignment, because the blue laser is not sensitive to reflective surfaces, representing an important advantage of the technology. As mentioned before the targets are allowing regardless of the technology (laser or structured light) to change the initial position of the specimen during the measurements leading to a more complete scan (Figure 71). In this case, the scanning time of one specimen was shorter and evaluated at approximately 40 minutes.



Figure 70 – Re-usable targets for multiple scans



Figure 71 – Changed position of the specimen for a more complete scan

6.3.2.4 Z+F IMAGER 5010C

The Z+F IMAGER 5010C used for the experimental measurements is a LiDAR based, static, Terrestrial Laser Scanner, has a resolution of approximately 0.1 mm and is capable of acquiring data points with a vertical FOV of 320° and a horizontal FOV of 360°. The Z + F IMAGER 5010C is mounted on a rigid tripod and has a fixed position throughout the data acquisition. To determine the position of the laser dot emitted on the scanned object, the integrated HDR camera is used. This integrated HDR camera has a resolution of 60-megapixel and was also used to automatically capture the colour information in each station point. The maximum scanning speed of the device is evaluated at 1,016,000 points per second. The measuring process consists of:

- 1) Mounting the scanning unit on a tripod;
- 2) Placement of paper targets in the working area around the measured specimen;
- 3) Automatic calibration of the laser scanner;
- 4) The actual scanning from different station points ;
- 5) Alignment of the data obtained in each station in the **Z+F LaserControl** software.

Four different quality levels can be set with the used instrumentation, depending on the resolution and measurement. For the measurement of the links, the resolution for the laser scanner was set to “High” (6 mm at 10 m), with quality balanced and normal (Figure 72). To scan the entire geometry of the links, 6 scans / specimen were carried out from 6

different scan stations. The calibration of the scanner was done automatically before every scan.



Figure 72 – Setting the resolution level (left) and calibration (right) of the LiDAR scanner

The position of the laser scanner has been this way constantly corrected, so that the maximum offsets do not exceed $\pm 2^\circ$, resulting in very high accuracy measurements. Before the actual scan, the positioning of the paper targets in the working area around the measured specimen was also done. The paper targets are made of two black triangles attached to the centre of the paper, which is the coordinate point to be considered in the post-processing stage. It was observed that choosing the positioning of the scanning stations and the positioning of the targets has a key role in optimizing and rationalizing the measurement phase, and in obtaining relatively small sized point cloud so that the post-processing of the data is less time-consuming. To determine the optimal position of the scan stations, it is important to consider the range of the scanner, the maximum distance to which the scanner ensures maximum accuracy and coverage relative to the position of the specimen. With a view to optimize the number of stations, the distance between the stations should not be too short, as it would result in a very high percentage of overlapping data (the same points seen from several stations) which would be useless and inefficient. It is also necessary to determine the positions that are providing the largest possible coverage area of interest, without any obstruction on the laser beam path. The scan positions of the scanner were chosen so that the emitted laser beam intersects the scanned surface in a perpendicular direction, as the scanned surfaces of the specimens were highly reflective. If the angle of intersection is too sharp, the accuracy of determining

the point would decrease considerably. Figure 73 presents the paper targets positioned around the scanned specimen.

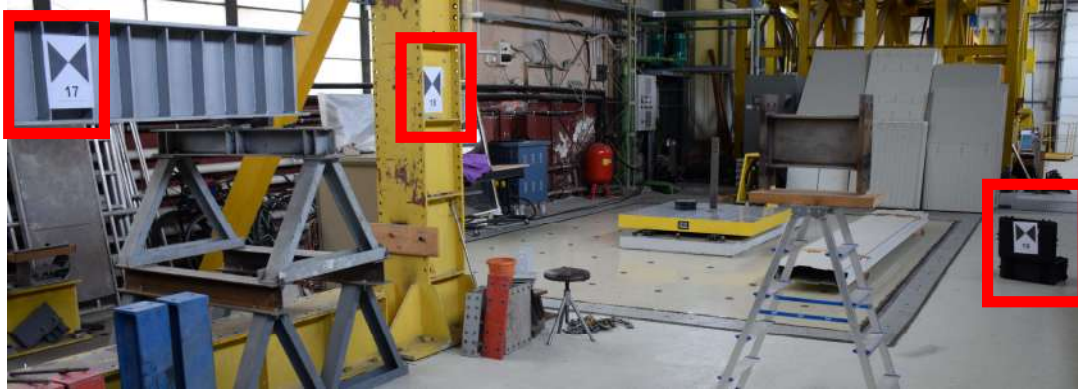


Figure 73 – Positioning of the targets for the LiDAR scanning

As mentioned, for the measurement of the links, it was proposed to choose 6 scan stations on each side of the specimen, at different heights and at an approximative distance of 1-1.5 metres from the measured objects to obtain accurate data and less overlapping. The LiDAR was shown not sensitive to the highly reflective surfaces of the specimens and no special laboratory conditions were needed.

The relatively small dimension of the scanned specimens has also not affected the outcome of the measuring process. Different scan stations from the actual scanning process are presented in Figures 74-75.



Figure 74 – General view of the LiDAR measurement set-up (a)



Figure 75 – General view of the LiDAR measurement set-up (b)

Each scan had a duration of 6 minutes leading to a total scan time of approximately 40 minutes. The raw data from the measurements is stored in ASCII format. The initial post-processing was performed using the **Z + F LaserControl** software; the scans were aligned manually using the targets as reference points that had been accurately positioned within the working area. As shown in Figure 76, based on the software outputs, the alignment of the scans was successful, the average deviation being evaluated at 0.8 mm.

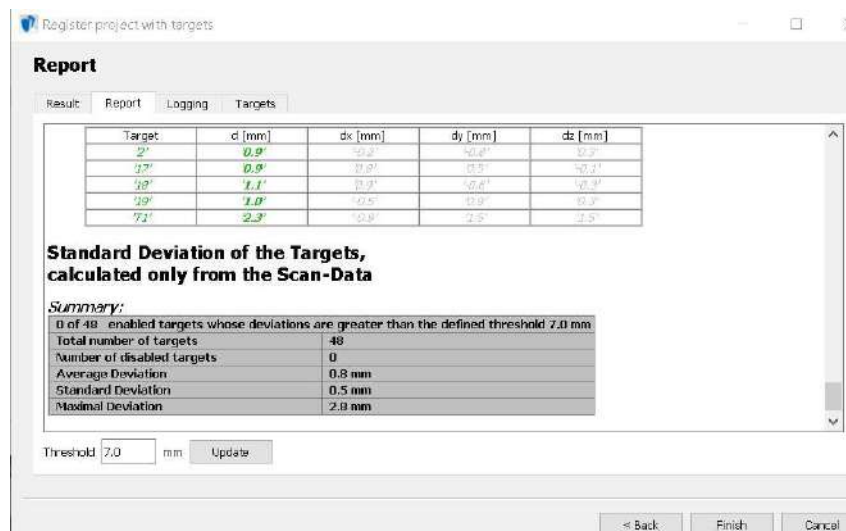


Figure 76 – Scan alignment precisions

6.3.2.5 IPHONE 14 Pro

As a last measurement method, it was proposed to investigate the capabilities of an unconventional 3D scanner - the relative novel Smartphone LiDAR. Traditionally, LiDAR systems and laser scanners are expensive and large pieces of equipment. Since 2020, Apple Inc. have introduced a LiDAR sensor in some iPhone and iPad models, facilitating in this way a more affordable alternative. The model used in the experimental measurements is the iPhone 14 PRO. The Apple LiDAR Scanner can measure the distance to surrounding objects up to 5 meters away, and can scan objects with a side length > 10 cm with an absolute accuracy of ± 1 cm.

For the actual 3D measurements, it was necessary to purchase and download the **Polycam** application from the AppStore (Figure 77). The application uses the LiDAR sensor and cameras of the smartphone to proceed the 3D scanning of the studied objects. The user-friendly interface of the app enables, besides LiDAR captures, photogrammetric measurements.



Figure 77 – Polycam – 3D scanning app

Measuring with the smartphone, the set-up also implied the use of a hand tripod for more stability and longer exposure (Figure 78). This method does not require any initial calibration or reflective targets. The actual scanning process is based on starting the data point acquisition in the Polycam app and moving the smartphone at a stable speed to obtain data points in all zones of the specimen. The data points are saved in the app and after the scanning procedure is completed, the Polycam app does the alignment of the point clouds automatically using his own embedded algorithms.



Figure 78 – Smartphone LiDAR measurement set-up

The duration of each scan was evaluated at 15-20 minutes, being the fastest measurement method of all. After the alignment step, the app enables to crop the point cloud to keep only the relevant data and obtain the final cleaned point cloud (Figure 79).

An important disadvantage observed during the scans is the sensitivity of the LiDAR sensor to sunlight and to the reflective surfaces of the measured specimens. As shown in Figure 80, the reflective areas could not be measured correctly with a single scan, but an important function of the Polycam application is that it enables the possibility to return to the scanning process through the **Extend** command. Due to the relatively small size of the specimens, the **Object Masking** command was also used for detailed processing.

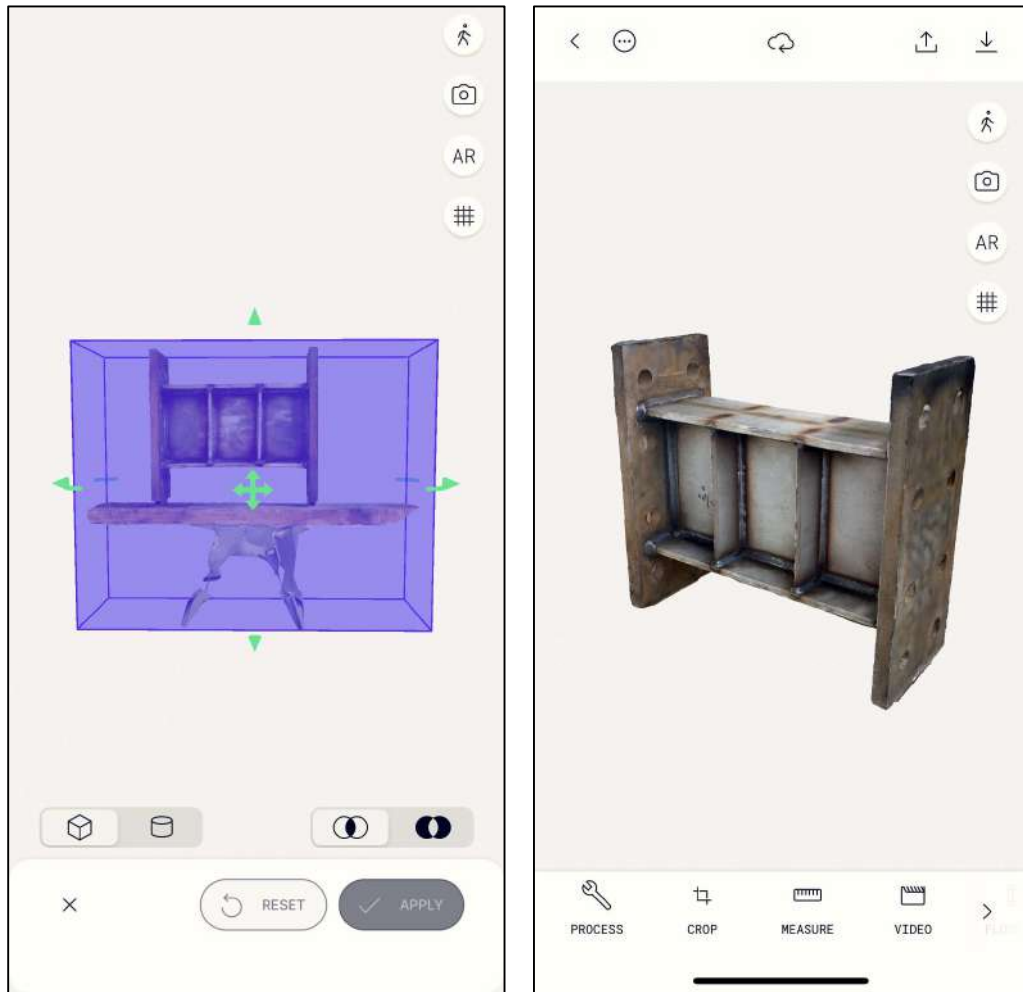


Figure 79 – Point cloud crop and final result in Polycam

Another important aspect observed during the measurements was the exaggerated overlapping effect due to the prolonged exposure of certain zones of the specimen to the LiDAR sensor. The overlapping of data points was an important factor in obtaining distorted and less accurate point clouds.



Figure 80 – Incomplete point cloud due to reflective surfaces of the specimens

Overall, the LiDAR sensor introduced by Apple Inc. in 2020 for the iPad Pro and iPhone Pro models presents a novel, cost effective and time efficient alternative to established methods of 3D scanning. Although accuracy and precision of the iPhone LiDAR models do not reach state-of-the-art standards, improvements in raw point cloud export, maximum scan size and range are only a matter of time for the still novel software applications.

6.3.3 RESULTS

At the end of the investigation campaign that targeted the 5 types of 3D scanners used in the actual laboratory geometric dimension and imperfection measurements, a comparison chart was made to identify the advantages and disadvantages observed during the scans. As shown in Table 12, each technology has positive and negative aspects that influence the final raw product of the scans - the point cloud. In case of three (Z+F, Hexagon, Iphone) out of the five scanners, the technology implies that the measured specimen keeps its initial position, which leads to unscanned areas. The measurement time varies between 15-20 minutes in the case of the smartphone and up to 90 minutes for the structured light scanner. Most technologies require manual pre-measurement calibration, excepting the TLS and the smartphone. Reflective targets are also demanded excepting the Hexagon Absolute Arm and Iphone. Sensitivity to reflective surfaces is an aspect observed during the scans just in the case of the structured light scanner and smartphone.

Table 12 – Comparison between the five scanner systems

Data acquisition device	Complete 360° scan capability	Duration/ scan (min.)	Calibration	Targets	Special lighting conditions	Sensitivity to reflective surfaces
Z+F IMAGER 5010C	✗	30-40	automatic	✓	✗	✗
HEXAGON Absolute Arm	✗	20-25	manual	✗	✗	✗
EinScan Pro HD	✓	80-90	manual	✓	✓	✓
CREAFORM HandySCAN3D	✓	30-40	manual	✓	✗	✗
IPHONE 14 PRO	✗	15-20	✗	✗	✓	✓

In terms of measured dimensions of the specimens (see Tables 13-18), the scanners show close values to the manual measurements, except the Iphone whose precision of one centimetre stated in the literature is demonstrated also in this case.

Table 13 – Comparison between manual measurements and 3D scans of specimen S-C

S-C		Flange thickness (mm)	End plate thickness (mm)	Length (mm)	Web height (mm)
Manual	front	12.02	25.01	498	246
	back	12.02	25.02	496	247
Hexagon	front	11.94	24.94	497	246
	back	11.95	24.96	496	246
Z+F	front	11.94	24.96	496	246
	back	11.95	24.98	495	246
14 PRO	front	13.04	25.64	507	253
	back	13.07	25.68	507	255

Table 14 – Comparison between measurements of specimen S-C (continuation)

S-C		End plate width (mm)		Flange width (mm)	Web thickness (mm)
Manual	left	200	top	140	8.26
	right	198	bottom	139	
Hexagon	left	200	top	139	8.23
	right	197	bottom	139	
Z+F	left	199	top	138	8.23
	right	197	bottom	137	
14 PRO	left	202	top	145	8.32
	right	202	bottom	142	

Table 15 – Comparison between measurements of specimen S-2DS-C1

S-2DS-C1		Flange thickness (mm)	End plate thickness (mm)	Length (mm)	Web height (mm)	Stiffener thickness (mm)
Manual	front	12.01	25.02	497	249	8.04
	back	12.00	25.02	497	249	8.01
Creaform	front	11.94	24.88	497	249	7.96
	back	11.95	24.88	497	249	7.91
Z+F	front	11.94	24.87	495	248	7.97
	back	11.94	24.85	496	249	7.94
EINSCAN	front	11.94	24.86	496	249	7.89
	back	11.96	24.88	496	248	7.87
14 PRO	front	12.80	25.97	515	257	9.29
	back	13.46	26.16	515	258	9.32

Table 16 – Comparison between measurements of specimen S-2DS-C1 (continuation)

S-2DS-C1		End plate width (mm)		Flange width (mm)	Web thickness (mm)
Manual	left	198	top	139	8.24
	right	198	bottom	139	
Creaform	left	198	top	139	8.21
	right	199	bottom	139	
Z+F	left	198	top	138	8.22
	right	196	bottom	138	
EINSCAN	left	198	top	139	8.22
	right	197	bottom	139	
14 PRO	left	206	top	144	8.33
	right	206	bottom	145	

Table 17 – Comparison between measurements of specimen S-2DS-C2

S-2DS-C2		Flange thickness (mm)	End plate thickness (mm)	Length (mm)	Web height (mm)	Stiffener Thickness (mm)
Manual	front	12.02	25.02	496	249	8.01
	back	12.02	25.01	498	249	8.02
Creaform	front	11.92	24.93	496	248	7.94
	back	11.94	24.89	497	248	7.95
Z+F	front	11.88	24.89	496	248	7.91
	back	11.90	24.92	496	248	7.93
EINSCAN	front	11.92	24.90	496	247	7.96
	back	11.94	24.93	497	247	7.94
14 PRO	front	12.82	25.12	513	258	8.40
	back	12.73	25.27	514	257	8.61

Table 18 – Comparison between measurements of specimen S-2DS-C2 (continuation)

S-2DS-C2		End plate width (mm)		Flange width (mm)	Web thickness (mm)
Manual	left	199	top	139	8.24
	right	200	bottom	140	
Creaform	left	197	top	139	8.21
	right	200	bottom	140	
Z+F	left	196	top	138	8.19
	right	198	bottom	139	
EINSCAN	left	197	top	139	8.21
	right	198	bottom	139	
14 PRO	left	205	top	145	8.35
	right	204	bottom	146	

6.4 POST-PROCESSING OF THE SCANNED DATA AND 3D MODELLING OF THE GEOMETRIC IMPERFECTIONS

From the structural perspective, point clouds cannot be used directly for 3D modelling and for numerical analyses because they are formed by many discrete points defined by three-dimensional coordinates. In order to effectively use the geometric data derived from the 3D scanning measurements, it is necessary to perform operations that transform the point cloud into a 3D model. As shown in Figure 81, the procedure to obtain a solid model compatible with a FEA software (for example Abaqus) from point clouds is not straight-forward.

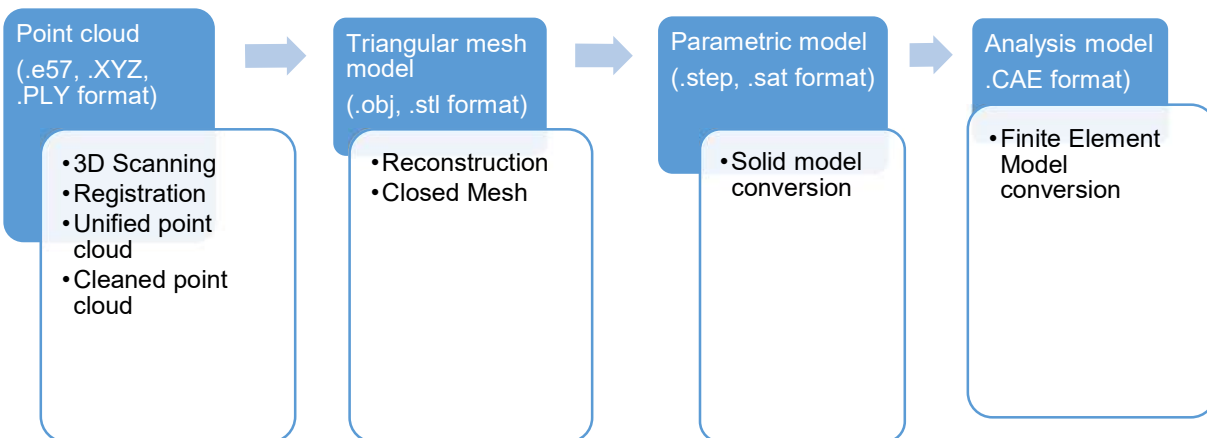


Figure 81 – Workflow of obtaining solid models from point clouds

Fortunately, the current features of most of the post-processing software which are offered besides the 3D scanners, also include the possibility to convert in a semi-automatic manner the point cloud into a mesh model, reducing the time spent for processing purposes. Currently only the LiDAR terrestrial laser scanners remain the last devices that do not have embedded such a software. As shown in Table 19, in comparison with the other selected scanners, the Z+F LaserControl software facilitates just the point cloud alignment, and the exported formats are also point clouds. Other third-party software, such as **CloudCompare** need to be used for specific post-processing steps to obtain a mesh model.

Table 19 – Post-processing capabilities of the software that comes with each scanner

Scanning device	Initial post-processing software	Features	Exported formats
Z+F IMAGER 5010C	Z+F LaserControl	point cloud alignment	.xyz, .e57, .asc, .rcs
HEXAGON Absolute Arm	Inspire	point cloud alignment and cleaning, mesh generation, deviation measurement analysis	.dxf, .acis, .stl, .iges, .3dpdf, .smx, .vda
EinScan Pro HD	Solid Edge	point cloud alignment and cleaning, mesh generation, deviation measurement analysis	.obj, .asc, .ply, .stl, .p3, .3mf
CREAFORM HandySCAN3D	VXelements	point cloud alignment and cleaning, mesh generation, deviation measurement analysis	.dae, .fbx, .ma, .obj, .ply, .stl, .txt, .wrl, .x3d, .x3dz, .zpr, .3mf
IPHONE 14 PRO	Polycam	point cloud alignment and cleaning, mesh generation	.fbx, .obj, .ply, .stl, .las, .pts, .xyz, .dxf

6.4.1 MANUAL MESH GENERATION FROM POINT CLOUDS

In case of the point clouds obtained from the TLS, several steps were taken to obtain a mesh model. First, the aligned point cloud was exported from Z+F LaserControl as .e57 file format and imported in the open-source software CloudCompare. The Z+F IMAGER 5010C was positioned at six distinct scan stations. This led to six distinct point clouds. The data acquired during the scans was imported successively in Cloud Compare. The first imported point cloud is shown in Figure 82. An interesting aspect is that the scanner captured not only the specimens, but also the whole structure of the laboratory where the measurements were done. This demonstrates the capabilities of the laser scanner when it comes to total measuring range.

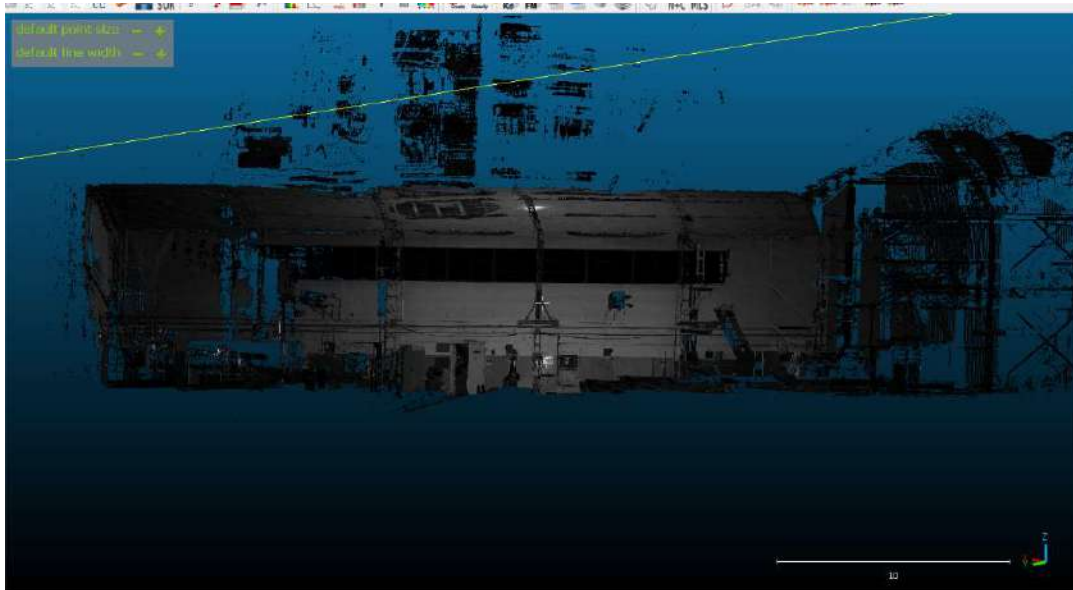


Figure 82 – Imported point cloud of the laboratory building

The first step that was taken is to check if the scans were properly aligned in the LaserControl software. In Figure 83 is presented a case when two consecutive scans are not aligned.



Figure 83 – Imported point cloud before proper alignment

After the alignment verification, the next step consists of identifying the measured specimen (Figure 84) in the dense point cloud. To remove the redundant data, the *Segment* command is used, as shown in Figure 85. This tool allows the user to interactively segment the selected entities by defining a 2D polygon or a rectangle on the

screen. This process can be repeated multiple times, changing the orientation of the entities each time, so as to properly segment the entities in 3D.

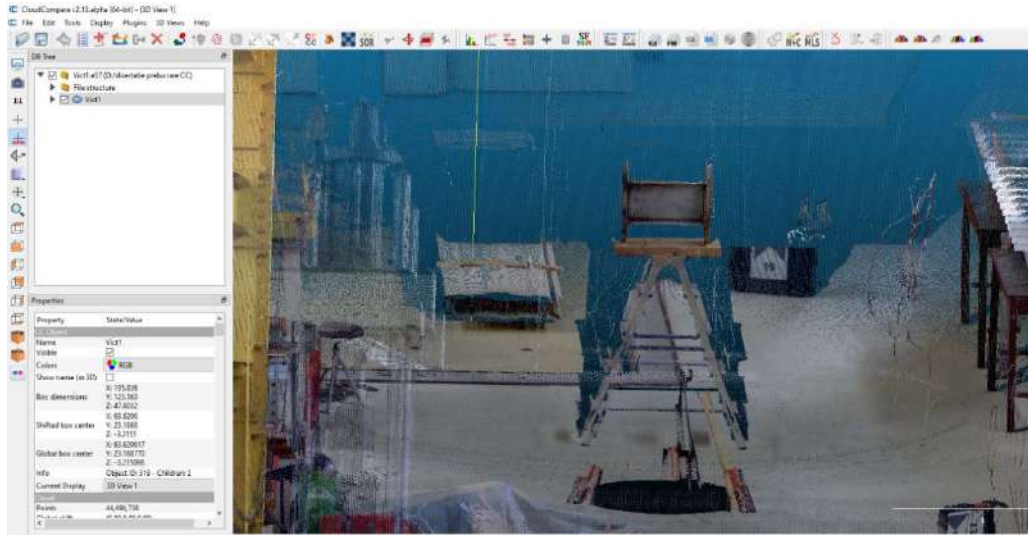


Figure 84 – Identifying the measured specimen

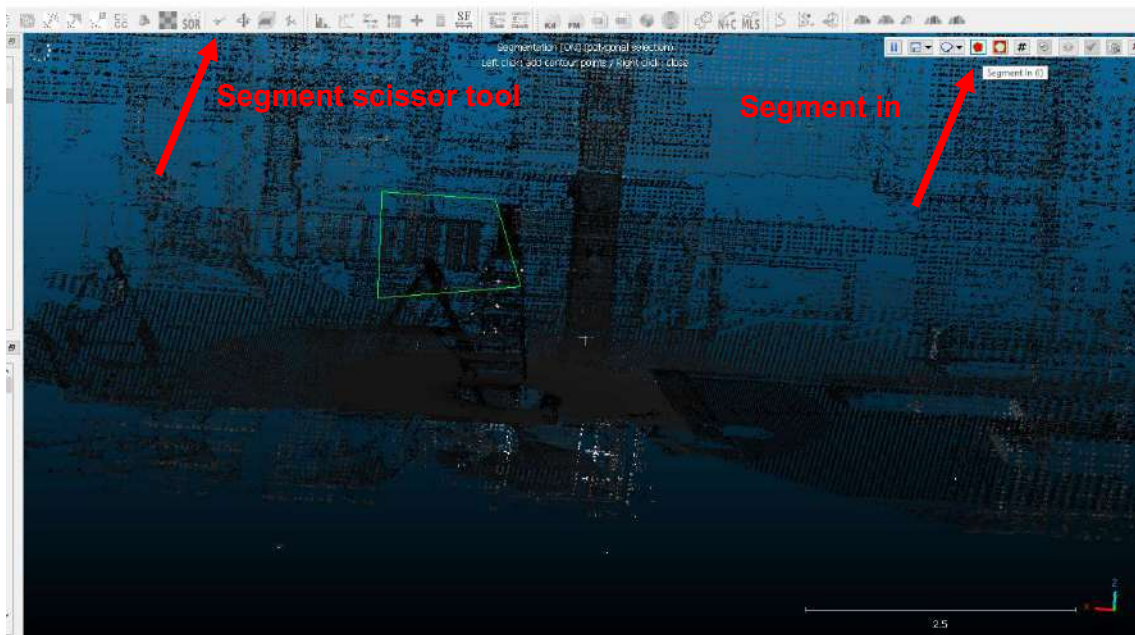


Figure 85 – Point cloud segmentation

After segmenting each of the point clouds, the command *Merge multiple clouds* was used to generate a single entity (Figure 86). In the last step, the point cloud was cleaned again of redundant points and coloured RGB. The final result can be seen in Figure 87.

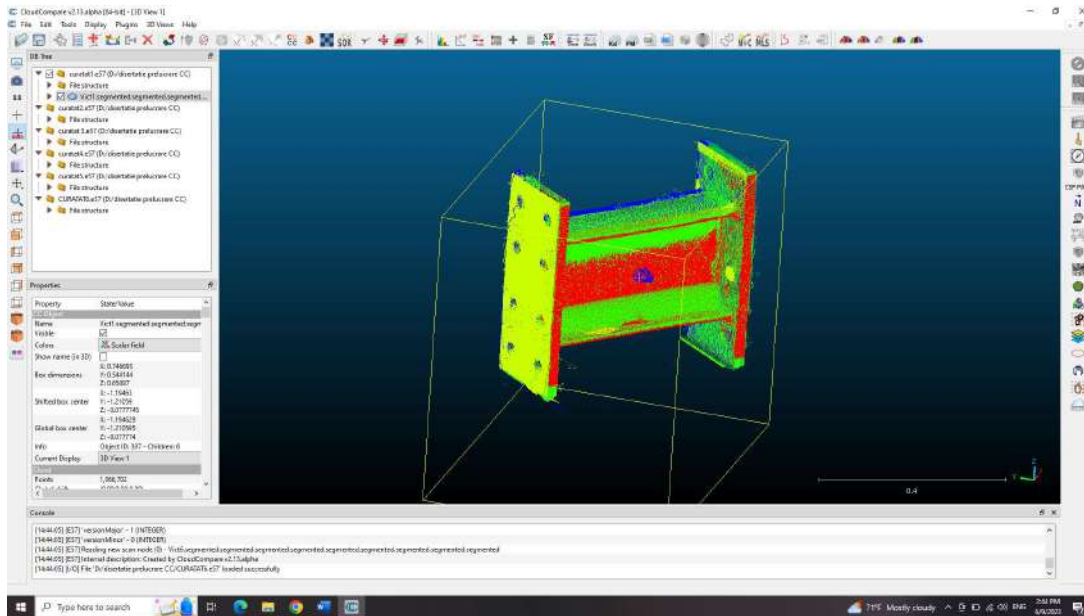


Figure 85 – Merging the six point clouds

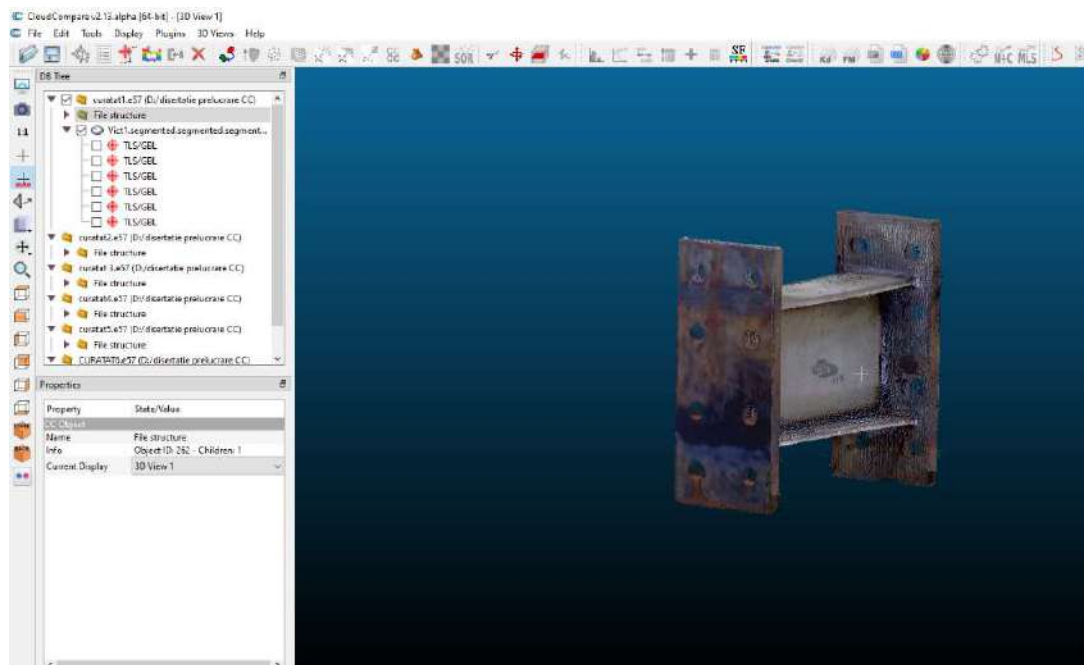


Figure 86 – The final cleaned and coloured point cloud

In order to obtain the mesh model of the link, the next step was to compute normals on the point cloud (Figure 87). The normal vector to a surface is a vector which is perpendicular to the surface at a given point. When normal vectors are considered on closed surfaces as in this case, the inward-pointing normal (pointing towards the interior of the surface) and outward-pointing normal needed to be distinguished. After the normals

were computed properly, the **Poisson surface reconstruction method** was used to create the mesh model (Kazhdan, et. al., 2006) as shown in Figure 88.

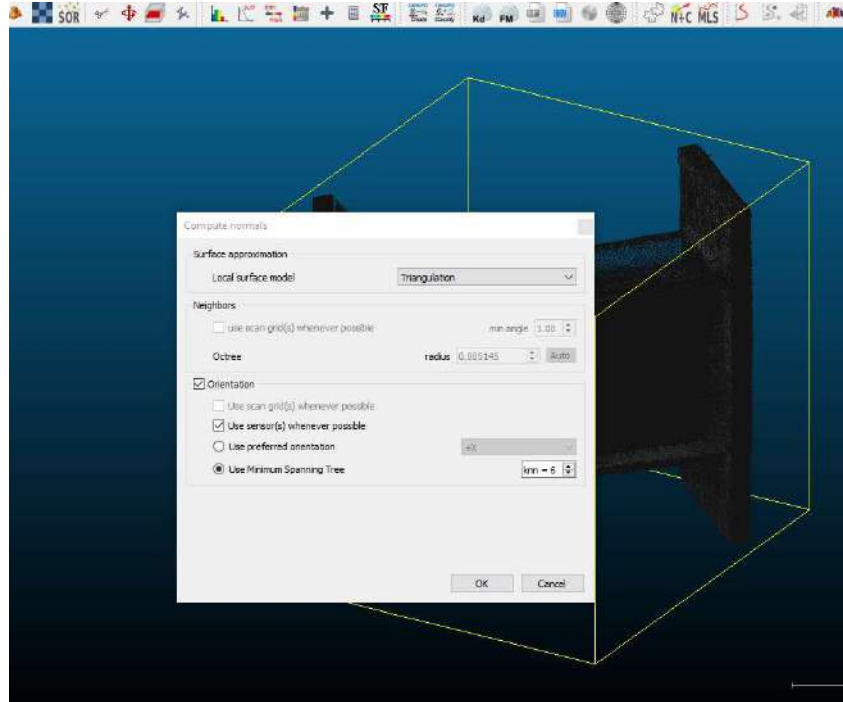


Figure 87 – Computing normals on the point cloud

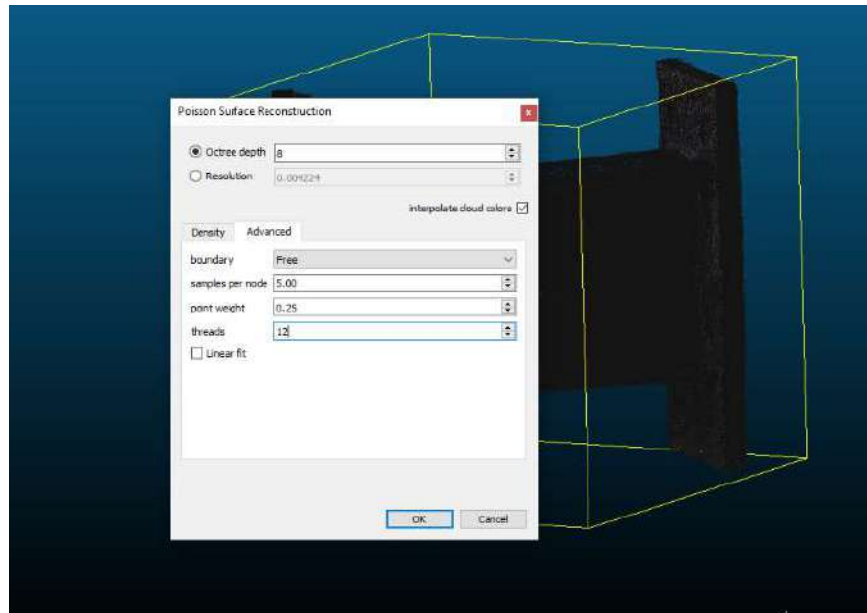


Figure 88 – Poisson surface reconstruction

The final mesh model (Figure 89) can be then exported to other programs such as Meshlab, FreeCad, Autodesk Fusion 360, and even Abaqus, as .stl file format.

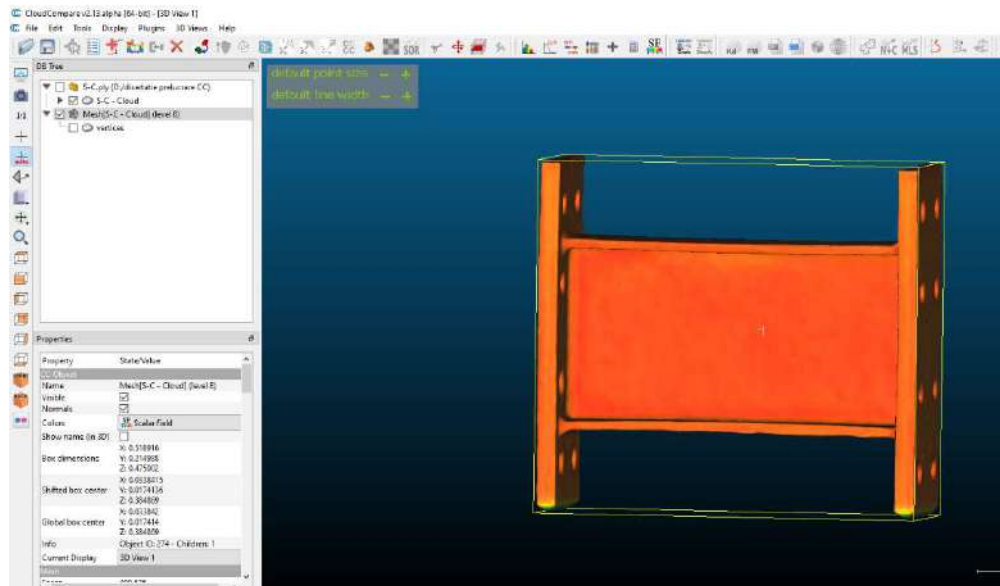


Figure 89 – Obtained mesh model from the point cloud

As shown previously in Table 13, the four other used scanning devices (EinScan, Creafom, Hexagon Absolute Arm, Iphone 14 PRO) enabled a more straight-forward procedure to obtain the .stl file format and can directly export the mesh model from the embedded software (VXelements, Polycam, Solid Edge, Inspire).

Next, it was investigated if the unprocessed .stl files exported from these programs can be used in the FEM software Abaqus to directly obtain the geometry model within it. First, the mesh models were imported into Abaqus with the following command from the main menu bar: **Plug-ins->Tools->STL Import**. It was observed that the stl file is imported into Abaqus as an **orphan mesh**. This means that once the model has been imported into Abaqus/CAE, the mesh is not editable. An orphan mesh part contains no feature information and is basically a collection of nodes, elements, surfaces, and sets with no associated geometry. Abaqus/CAE enables the conversion of an orphan mesh to editable geometry by using the command: **Plug-ins->Create geometry from mesh** (Figure 90).

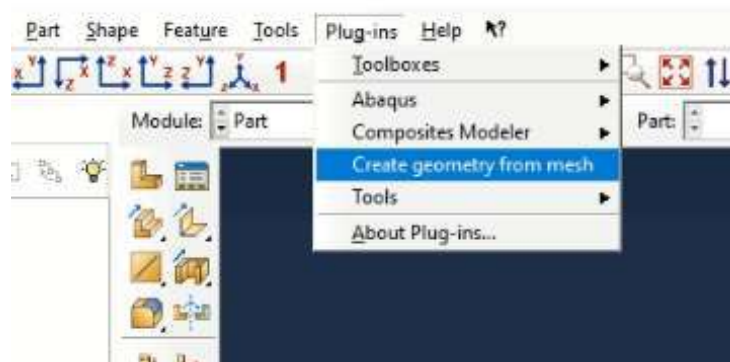


Figure 90 – Geometry from mesh plug-in in Abaqus

During the conversion process, it was shown that the models have missing elements and failed to be completed (Figure 91). This issue is related to the fact that the raw .stl files contain mesh models that are not closed properly.

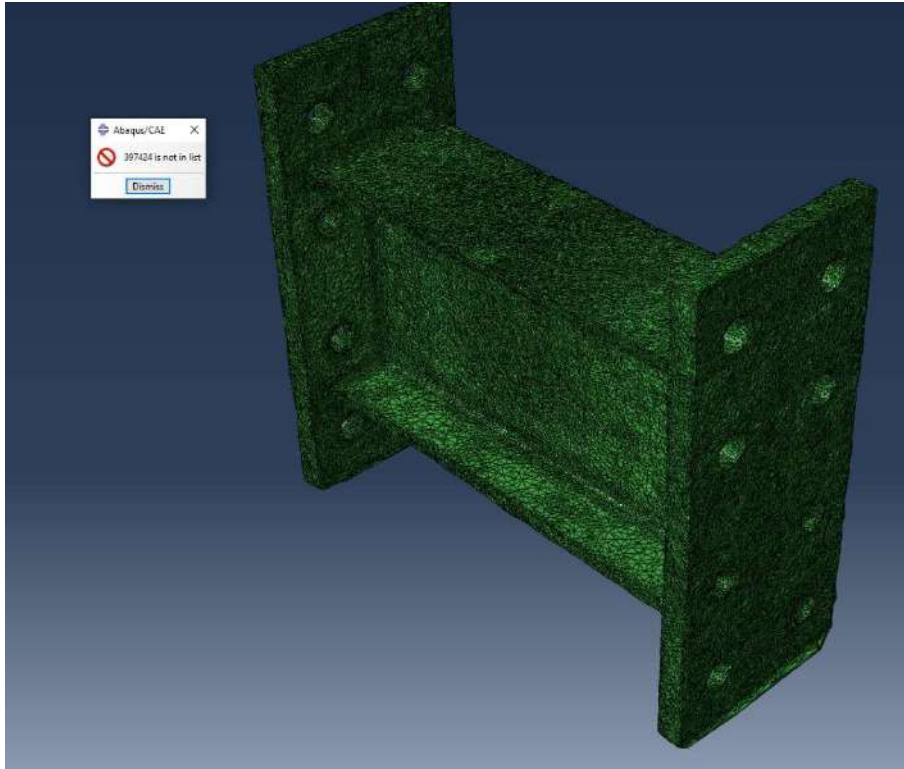


Figure 91 – Abaqus error during conversion from mesh to geometry

6.4.2 GENERATING SOLID MODELS FROM 3D SURFACE MODELS

Abaqus CAE requires the imported model to be a 3D solid that is able to be assigned with volume and weight. These 3D solids are called manifold 3D solids. The 3D models, directly constructed by the programs (Vxelements, Solid Edge, Polycam) that are offered for post-processing besides the presented scanners, are only individual triangular 3D surfaces.

Thus, it was necessary to identify a third-party software in which the 3D surface models (mesh models) can be imported for repairing and improvement of the mesh and eventually to obtain the editable geometry (solid model).

A 3D surface model or simply stated as mesh model is generally a collection of multiple individual triangular planes formed by connecting points in the point cloud. As the number of points increases, the point cloud is more likely to have individual planes that are intersecting each other, which can cause issues for the later processes. Another issue is that holes are also expected to be present at gaps with sharp angles or in areas without enough data points. These surfaces are defined as **non-manifold surfaces**.

Manifold 3D surface is defined as a 3D surface that encloses itself and does not have any gaps and self-intersection. Therefore, to ensure that the 3D surface model can be transformed into 3D solid, any holes in the 3D surface model need to be closed. Repair of non-manifold 3D models after the initial construction of the 3D model is important because it will directly affect whether or not the model is able to be analyzed in FEM software packages.

The capabilities of three open-source programs that are supporting automatic repair solution for non-manifold 3D models were investigated: Autodesk Fusion 360, FreeCad, Meshlab. The three programs were all successful in repairing the models, but the solid conversion was only managed in Autodesk Fusion 360. Next, the sequence of steps that was carried out in Fusion 360 to obtain the final solid model is presented below.

After importing the .stl files, the *Close Holes* tool (see Figure 92) can be used to repair the continuity issue in the 3D surface model. However, some holes may not be fixed by this tool if there are self-intersected surfaces. This is more likely to happen when the 3D surface model is constructed based on a dense point cloud with too many points.

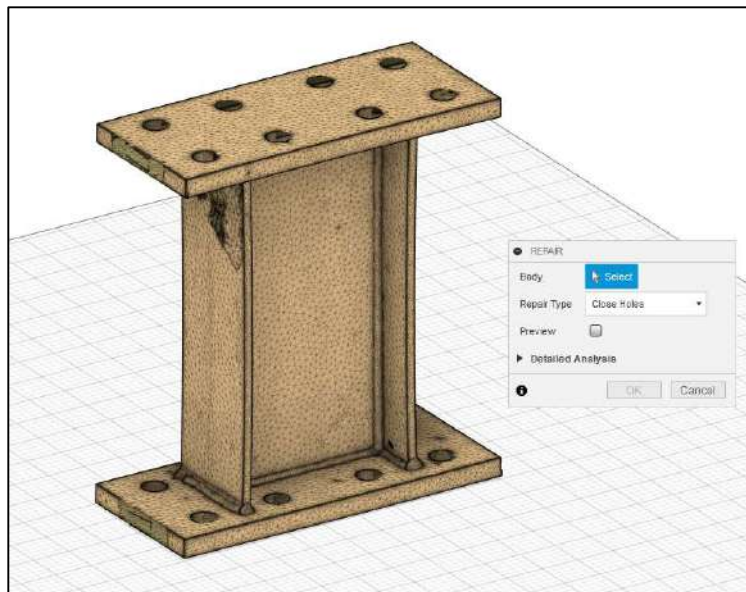


Figure 92 – Close Holes tool in Autodesk Fusion 360

The next used tool was *Stitch and Remove*, that basically stitches triangles, removes double triangles, removes degenerated faces, and removes tiny shells (Figure 93).

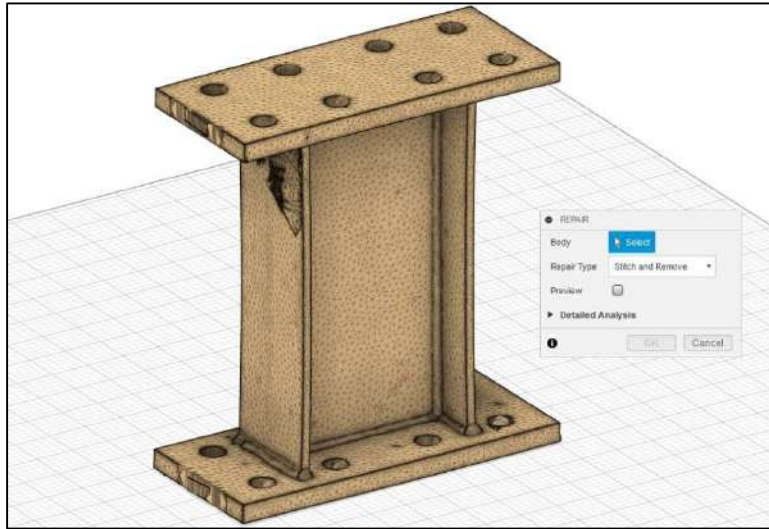


Figure 93 – Removing degenerated faces

The *Wrap* tool was applied on the surface of the mesh body, and all inner structures were in this way destroyed (Figure 94).

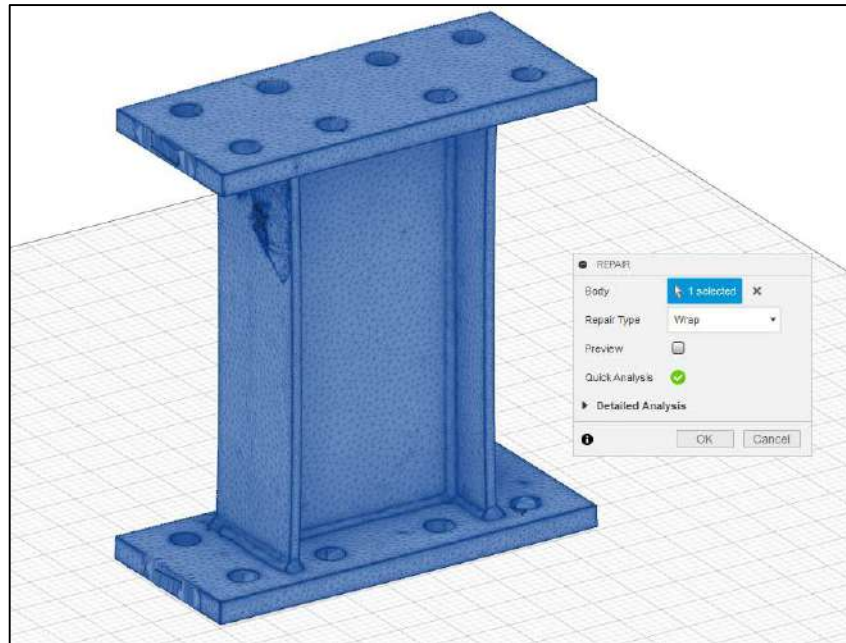


Figure 94 – Wrap tool used for deleting all inner structures

The last repair tool used on the model is the *Rebuild* function, that rebuilds the mesh body while preserving sharp edges (Figure 95).

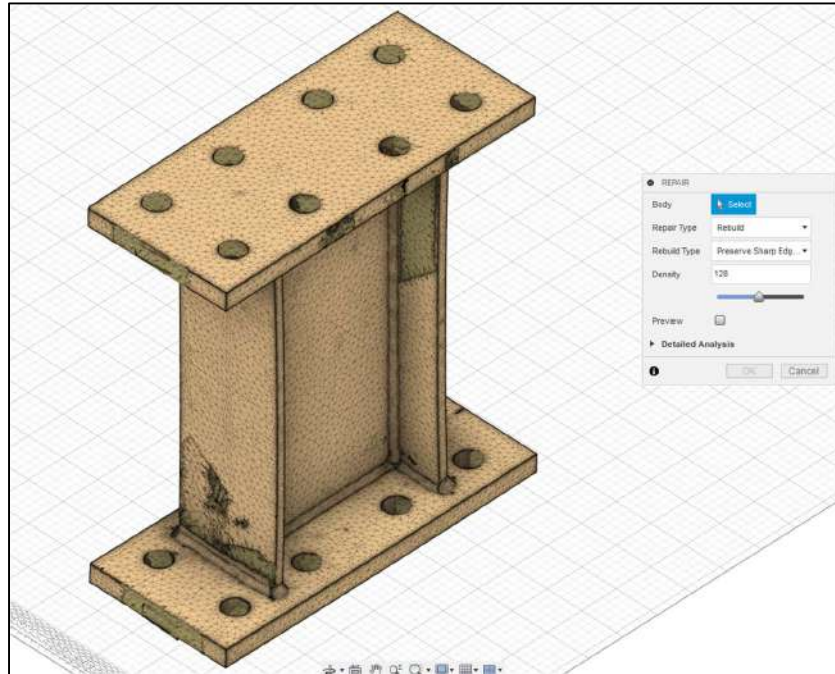


Figure 95 – Rebuild mesh body function

The repaired manifold 3D surface (see Figure 96) was then scaled to the actual size of the specimen.

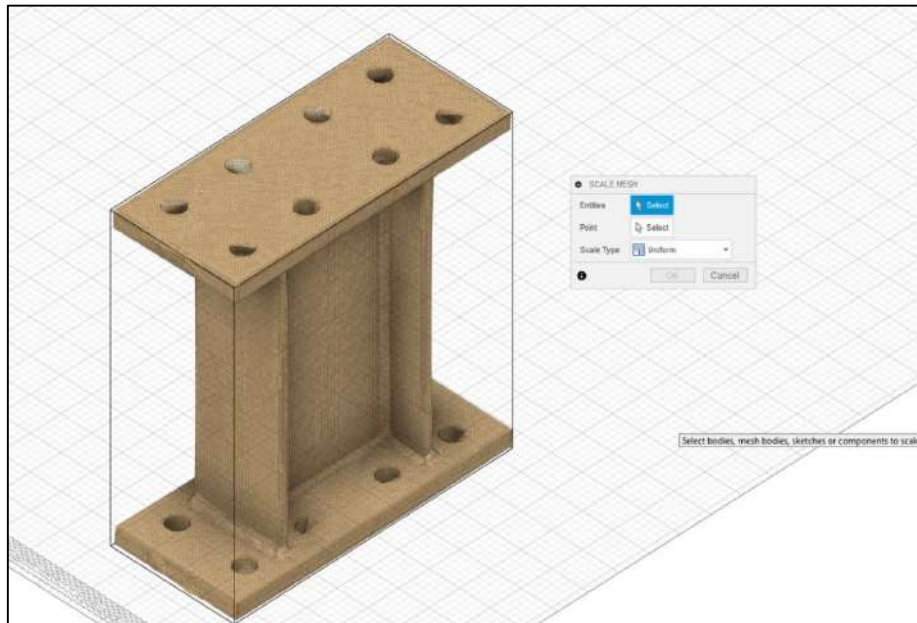


Figure 96 – Scaled and repaired model

Due to the high complexity of the obtained manifold 3D surface, it was necessary to reduce the mesh size (Figure 97). The *Face count* reduction type was proposed for this study.

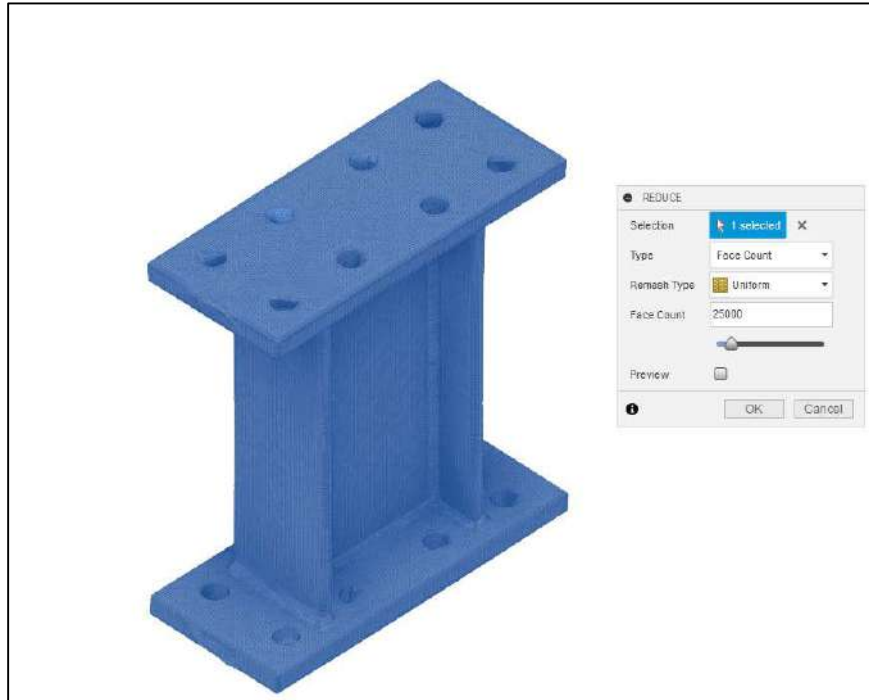


Figure 97 – Face count reduction

Autodesk Fusion 360 enables an automated conversion procedure of the mesh model to a solid model. From the 3 methods available, the *Faceted* method has shown the more reliable results (Figure 98).

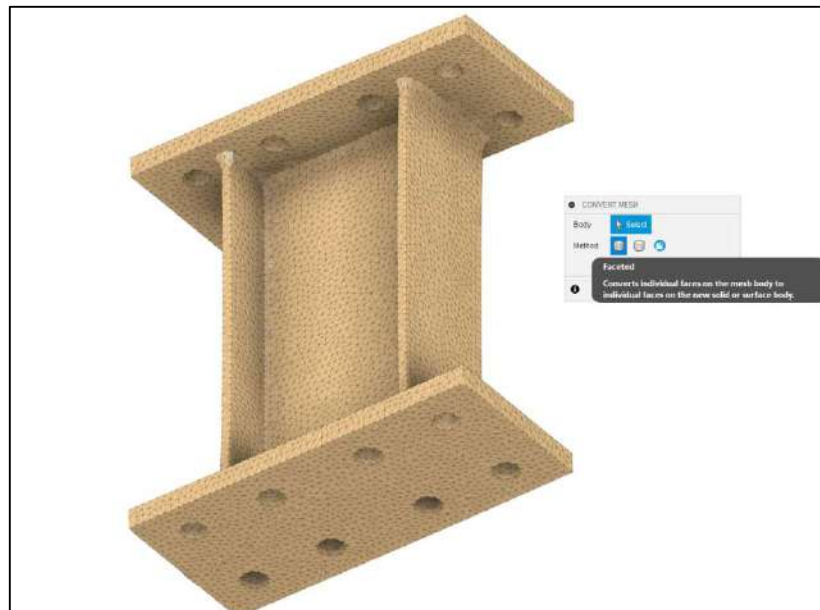


Figure 98 – Automated mesh to solid conversion

The final output (see Figure 99) is a 3D solid model with virtual topology (black lines) that can be exported as a .step file to the FEM software (Abaqus). In this manner the real initial geometric imperfections of the specimens can be considered in the FE analysis.



Figure 99 – Final 3D solid model with virtual topology (black lines)

6.4.3 DEVIATION MEASUREMENT ANALYSIS

A method to identify the real geometric dimensions and shape of the specimens is proposed by using the deviation measurement analysis, provided by the post-processing software of the 3D scanner. In case of Hexagon Absolute Arm, the embedded software **Inspire** provided this feature and was successfully applied to measure the geometric deviations of the specimen S-C. First, the point cloud model obtained from the 3D scanning measurements was overlaid on a nominal CAD model of the specimen as shown in Figure 100. Comparing the values from the point cloud with the nominal CAD model, the deviations from the nominal dimensions and shape are obtained (see Figure 101).

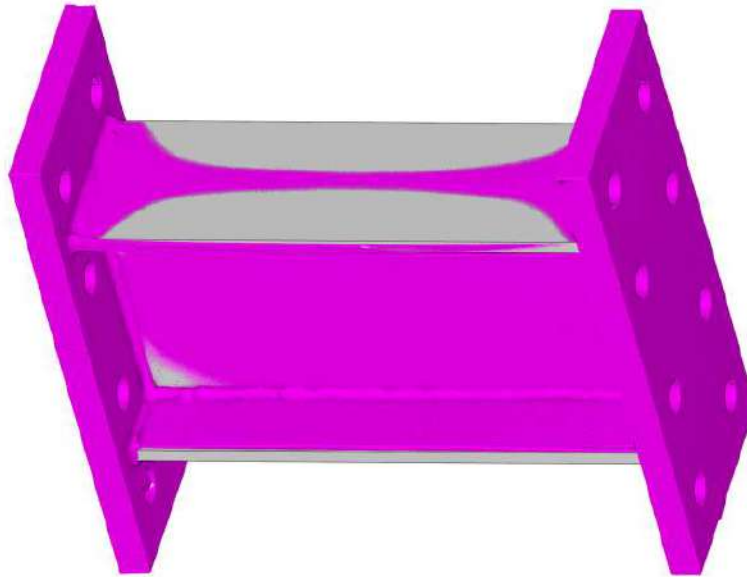


Figure 100 – Overlaying the point cloud with the CAD model

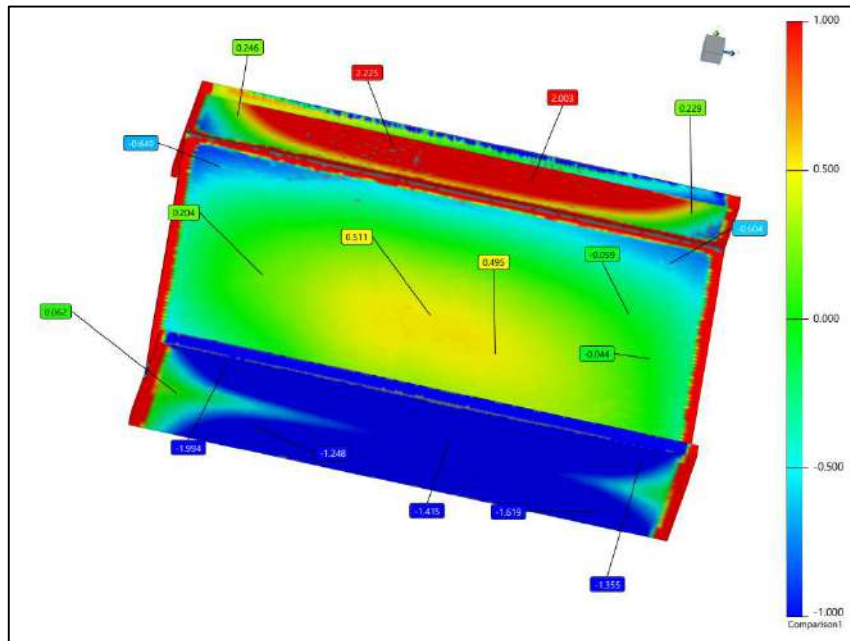


Figure 101 – Colorised map of the dimension deviation

Furthermore, cross-sections were created in order to compare the point cloud data and nominal CAD dimensions, in different section cuts (see Figures 102-103).

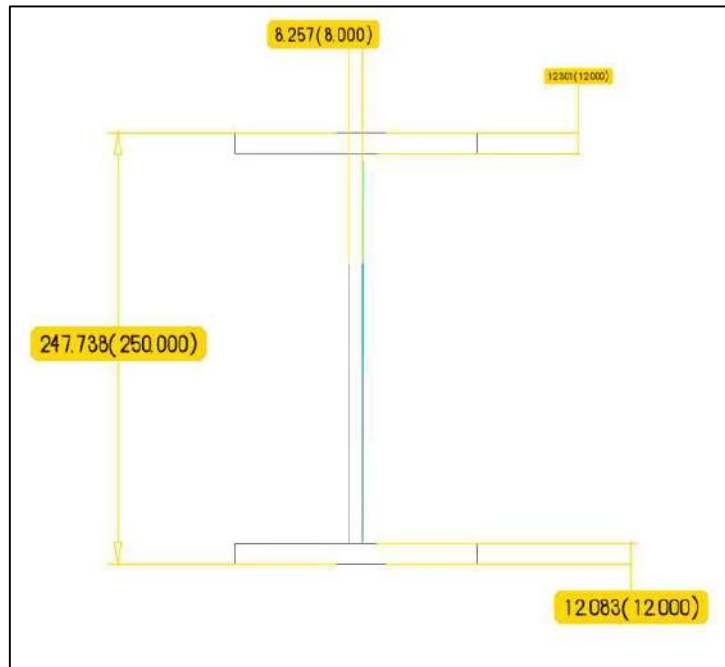


Figure 102 – Geometric dimension comparison in a section cut

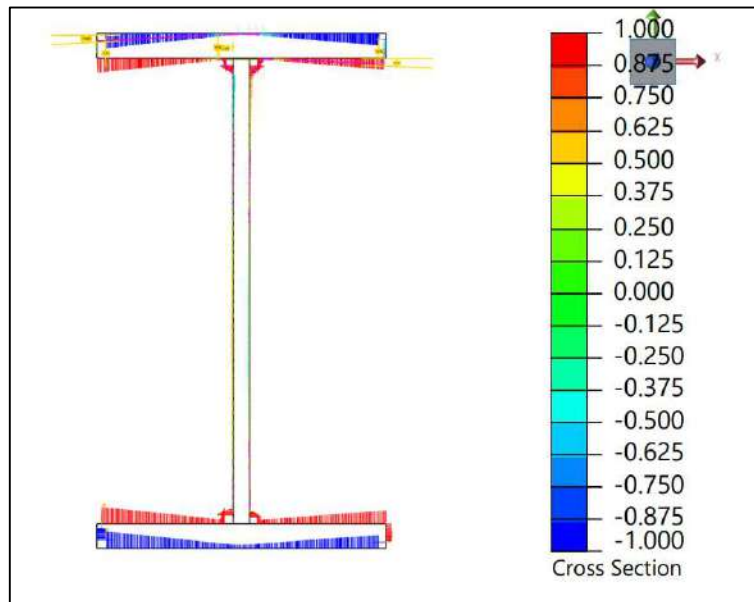


Figure 103 – Shape of the geometric imperfections of the flanges

The cross-sectional deviation analysis also includes the comparison of the welding angle (as shown in Figure 104).

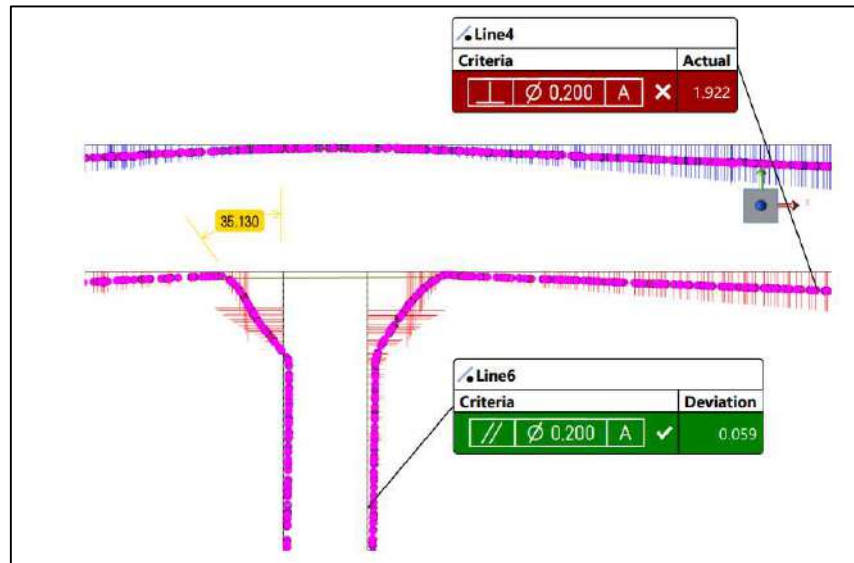


Figure 104 – Welding angle deviation measurement

The complete results of the analysis are presented in the measurement report in Appendix B.

In addition, **Ansys SpaceClaim** was used for further investigations in terms of deviations, not overlaying a scanned model with a nominal CAD model, but instead between two different scans (see Figure 105). The deviations between the measurements with Hexagon Absolute Arm and the smartphone are considerable, demonstrating the low accuracy of the latter.

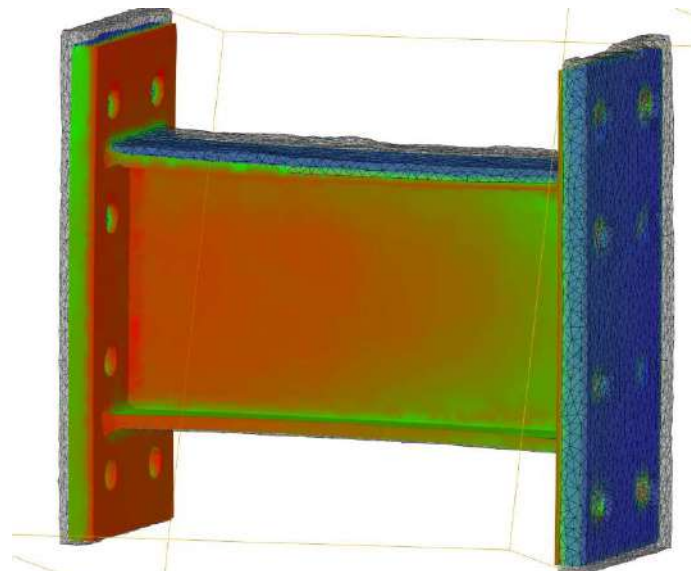


Figure 105 – Deviation measurement between two different scans

7 FINITE ELEMENT MODELLING OF THE GEOMETRIC IMPERFECTIONS

In order to investigate the influence of the geometric imperfections in the FE analysis of the steel links, a comparison was proposed between:

- FE model of the specimen S-C, developed in Abaqus/CAE of the without any geometric imperfections;
- FE model of the specimen S-C, developed in Abaqus/CAE with code-based values for the geometric imperfections applied through pressure load on the web;
- FE model of the specimen S-C, developed in Abaqus/CAE with code-based values for the geometric imperfections applied as a buckling mode;
- FE model of the specimen S-C, developed in Abaqus/CAE with measured values (from the 3D scans) for the geometric imperfections;
- FE model of the specimen S-C developed in Fusion360 with the real geometric imperfections.

7.1 NUMERICAL MODEL

7.1.1 FE MODEL WITHOUT IMPERFECTIONS

The finite element model includes both the link and the experimental rig (as shown in Figure 106). The frame was modelled using beam and truss elements. The imposed boundary conditions (out-of-plane and torsional restraints) aimed to reproduce, as closely as possible, the experimental setup. The actuator force was simulated as a displacement imposed at the top of the rig column.

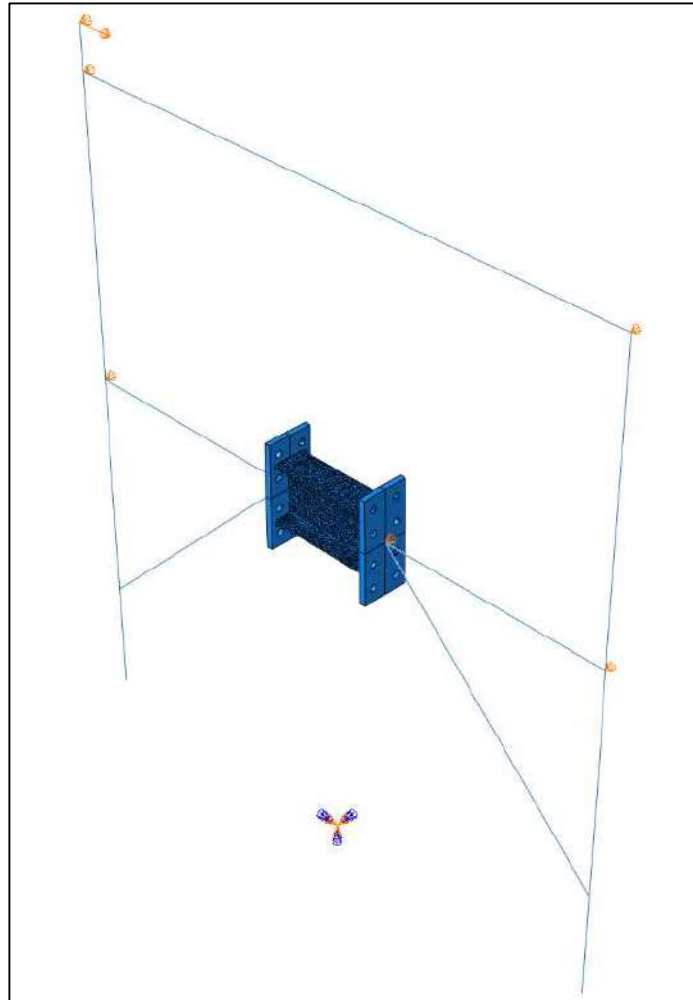


Figure 106 – Numerical model of the link and experimental rig

The link itself was modelled with solid elements using C3D8R finite elements (8-node linear brick with reduced integration and hourglass control), which were tied using Tie Constraints between corresponding surfaces. In order to set an output request similar to experimental data acquisition, two diagonal connectors between the end plates of the beams were modelled, and their relative displacements were recorded (Figure 107). These output data provided the link displacement in terms of rotational angle (rad).

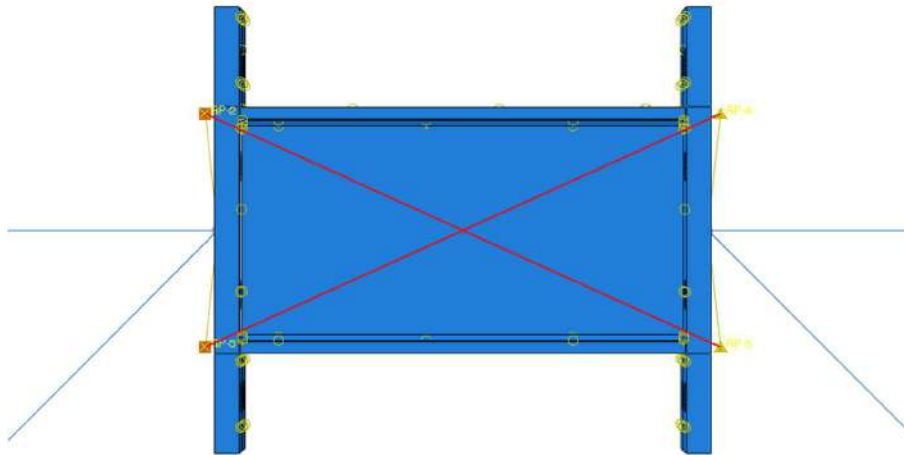


Figure 107 – Diagonal connectors DT1 and DT2 for rotation monitoring

7.1.2 FE MODEL WITH IMPERFECTIONS APPLIED AS BUCKLING MODES

The FE model was computed in Abaqus/CAE as presented in Section 7.1.1 and the geometric imperfections were applied according to **prEN 1993-1-14: Design of steel structures — Design assisted by finite element analysis**, Section 5.4.4 as equivalent geometric imperfections for cross-sections of plated structures (Figure 108), by applying a buckling analysis.

Component/type of imperfection	Shape	Magnitude
longitudinal stiffener with length a	bow	$\min(a/400, b/400)$
panel or sub-panel with short span a or b	buckling shape	$\min(a/200, b/200)$
stiffener or flange subject to twist	bow twist	$1 / 50$
outstand elements for cold-formed structures – local	buckling shape	$b / 125$
outstand elements for cold-formed structures – distortional	buckling shape	see Formula (5.17)

Figure 108 – Magnitude used for the equivalent geometric imperfections

In order to account for geometric imperfections using buckling analysis, in Abaqus software package was created a "Buckle, Linear perturbation" step in the Step Module, requesting 4 eigenvalues. After performing an eigenvalue buckling analysis to obtain the imperfection geometry, the 4th buckling mode was considered as the most appropriate one and was imported in actual analysis by specifying the eigenvalue mode number and load multiplier within "Edit keywords" option for the considered numerical model (Figure 109). The model with imperfections computed as buckling mode has the disadvantage of the impossibility of the controlled application of imperfections on the link components in the necessary amount.

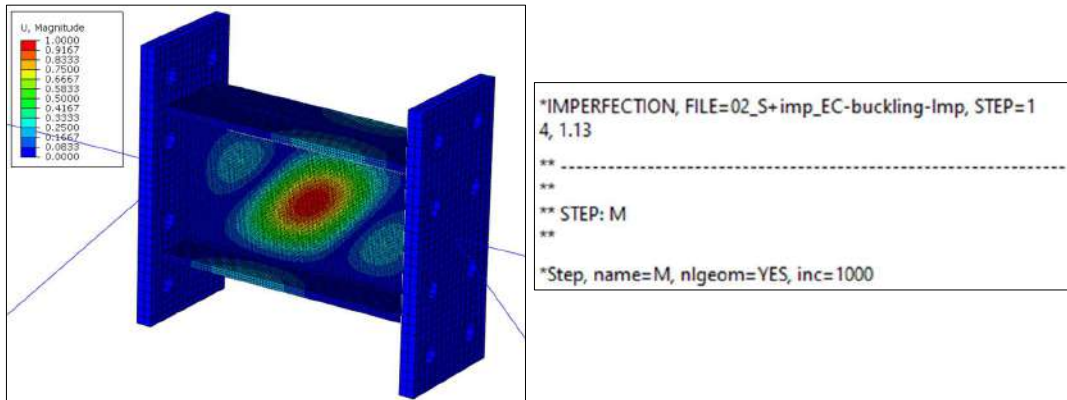


Figure 109 – The 4th eigenvalue buckling mode of the link and procedure for importing geometric imperfections obtained in buckling analysis step

7.1.3 FE MODEL WITH EQUIVALENT IMPERFECTIONS APPLIED AS PRESSURE LOAD

The same equivalent geometric imperfections were applied according to prEN 1993-1-14: Design of steel structures — Design assisted by finite element analysis, Section 5.4.4, but in this case by restraining out-of-plane translations along the web panels, and using an applied pressure load for the web and flange of the link as presented in Table 20

Table 20 – Applied code-based pressure loads on link

Type of imperfection	Component	Value
panel or sub-panel		$w_{nec} = \min(450/200; 226/200) = 1,13 \text{ mm}$
flange subjected to twist		$w_{nec} = ((140-8)/2)/50 = 1,32 \text{ mm}$

An analysis for each of these imperfection types was performed by applying a pressure on corresponding link component, and the results were multiplied in order to

obtain the needed value of the equivalent geometric imperfections. Easy controlled application of imperfections represents a significant advantage of this method (Tables 21-22).

Table 21 – Resulted imperfection values for the link flanges

Component	Imperfection value acc. to prEN 1993-1-14	Resulted imperfection value	Imperfection value multiplier
Link flanges	1.32 mm	0.0833 mm	15.85

Table 22 – Resulted imperfection values for the link web

Component	Imperfection value acc. to prEN 1993-1-14	Resulted imperfection value	Imperfection value multiplier
Link web	1.13 mm	0.624 mm	1.811

The imperfections resulted from a model including both pressure on link web and on flanges, scaled to nominal amount (Figure 110), were imported to the actual monotonic numerical simulation using "Edit keywords" options, similar to the procedure described in the previous section.

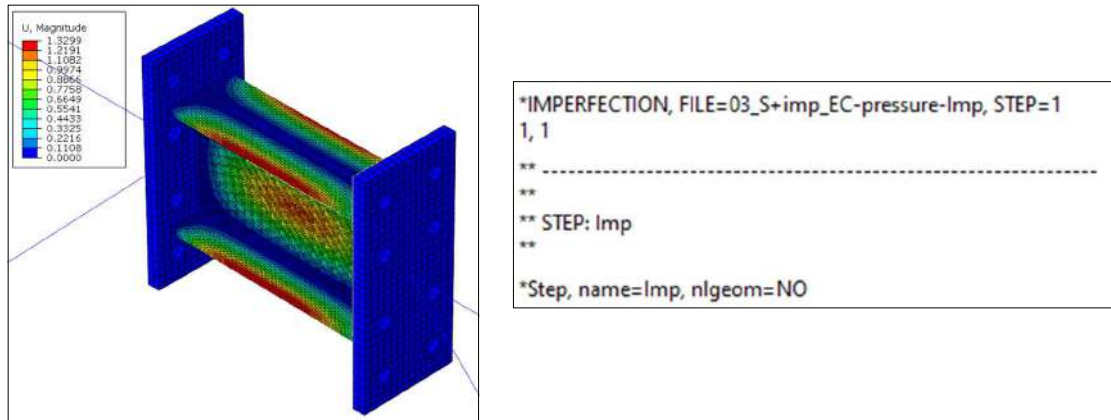


Figure 110 – The model reproducing imperfections by applying pressure on the link components and procedure for importing geometric imperfections obtained in imperfection analysis step

7.1.4 FE MODEL WITH MEASURED IMPERFECTIONS APPLIED AS PRESSURE LOAD

Geometric imperfections were modelled in this case, by restraining out-of-plane translations along the web panels and applying a pressure load on the link web to obtain a deflection equal to the values obtained from the 3D scan measurements.

The scanned link model imported in Abaqus containing geometric imperfections was inspected to determine average deviations of peripheral nodes of the web plate and flange plates with respect to the middle ones. The identified deviations defined as geometric imperfections are presented in Figure 111 and Table 23 .

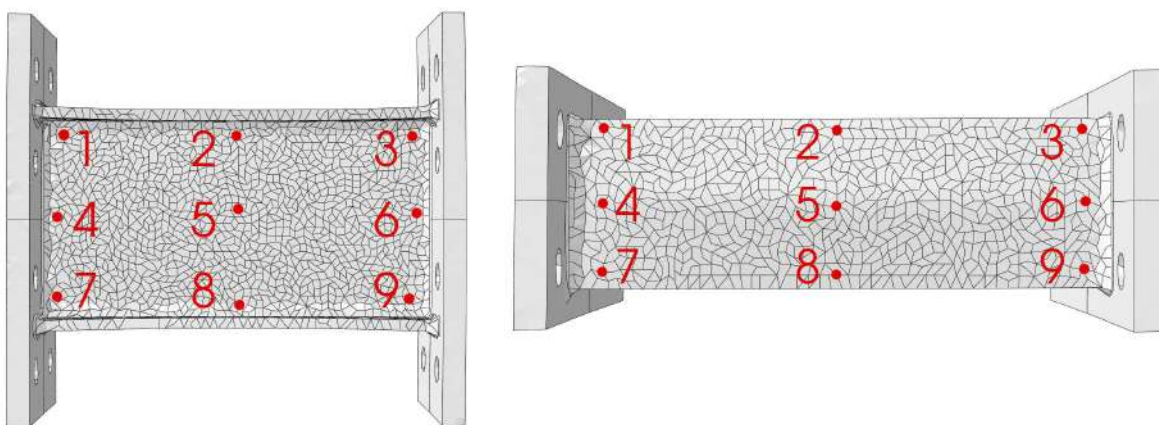


Figure 111 – Imperfection reference points on the link web and flange

Table 23 – Imperfection value calculation for link web and flanges

LINK WEB										
Points coordinates on the front surface of the link web						Average geometric imperfection	Imperfection value adopted for numerical model			
1	3.535938	2	3.325977	3	3.387012	0.764 mm	0.76 mm			
4	3.205127	5	2.438525	6	3.169727					
7	2.75835	8	2.736377	9	3.502979					
Points coordinates on the back surface of the link web						Average geometric imperfection			0.76 mm	
1	-4.397412	2	-4.74165	3	-4.493848	0.754 mm				
4	-4.957715	5	-5.646191	6	-5.50459					
7	-4.600049	8	-5.380078	9	-5.065137					
LINK FLANGES										
Points coordinates on the top flange of the link						Average geometric imperfection	Imperfection value adopted for numerical model			
1	124.155029	2	121.13806	3	124.26672	3.081 mm	3.07 mm			
4	125.387329	5	124.23926	6	125.17859					
7	124.220337	8	121.78931	9	124.36774					
Points coordinates on the bottom flange of the link						Average geometric imperfection			3.07 mm	
1	-124.70117	2	-122.2543	3	-124.9648	3.054 mm				
4	-125.10217	5	-124.4009	6	-125.5276					
7	-124.79639	8	-121.4016	9	-124.681					

The calculated geometric imperfections were imported to the actual monotonic numerical simulation using "Edit keywords" options, similar to the procedure described in the previous section.

7.1.5 FE MODEL DEVELOPED FROM THE 3D SCAN

As mentioned in Section 6.4.2 of Chapter 6, the final 3D model that was obtained in Autodesk Fusion 360 is a solid. In case of this model, it was then imported in Abaqus/CAE as a .step file, and parts of the virtual topology from the geometry were combined (see Figure 112).

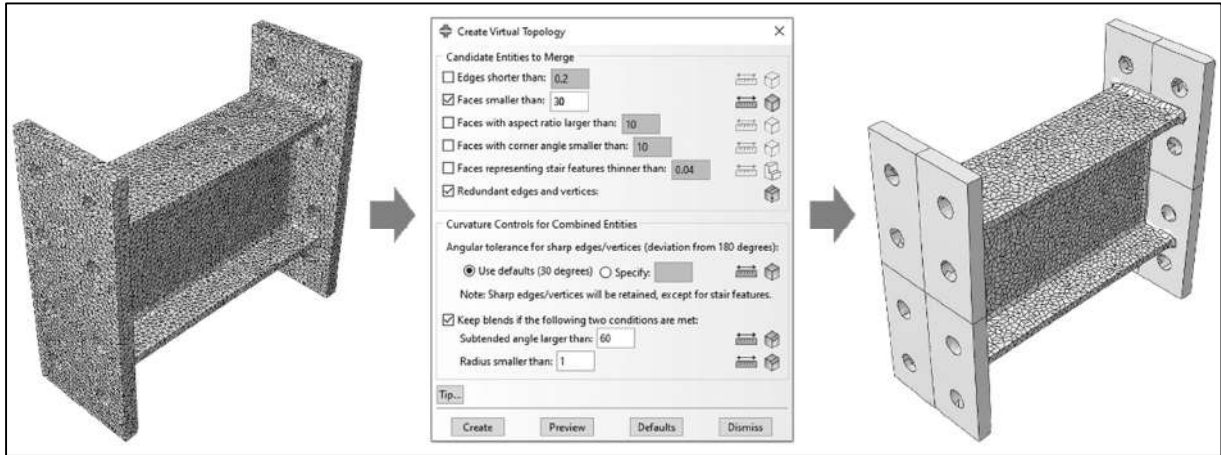


Figure 112 – Combining virtual topology

For discretizing the model with flexible and even sizes of elements, the virtual topology needs to be combined before the discretization by using the tool *Virtual Topology – Automatic create*. Since boundary conditions and loads can only be assigned at vertexes and edges, some of them might need to be restored using the tool *Virtual Topology – Restore entities*. The vertexes and edges are also the baselines for discretization.

Free meshing with tetrahedral elements was used for this FE model, as shown in Figure 113.

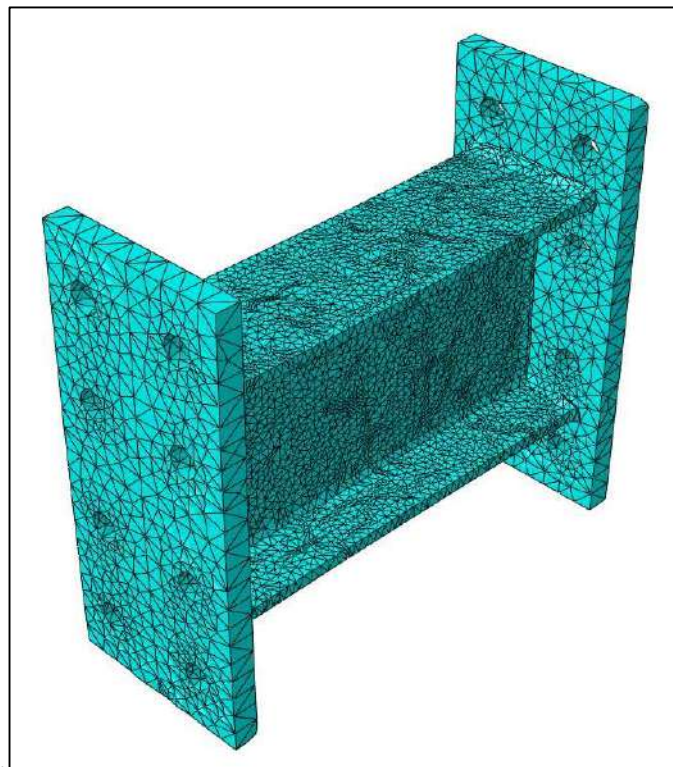


Figure 113 – The FE mesh of the model

7.2 MODEL CALIBRATION

The numerical model of the link was calibrated on past experimental tests performed on hybrid links with flanges made of mild carbon S235 steel and link web made of stainless steel 1.4404 (Raport științific și tehnic, Etapa 3: Încercări experimentale pe îmbinări sudate și linkuri, și elaborare recomandări de proiectare pentru linkuri hibride “HYLINK”, 2022). The finite element model developed using ABAQUS software includes both the link and the experimental rig. The frame was modelled using beam and truss elements, while the link using shell elements (S4R element type, a 4-node general-purpose shell with reduced integration and hourglass control). The imposed boundary conditions (out-of-plane and torsional restraints) aimed at reproducing, as closely as possible, the experimental setup. The results of FEM analysis, in terms of link shear force (V) and deformation (γ), show a good agreement with the experimental response (see Figures 114-115).



Figure 114 – Comparison of post-test deformed link and the plastic strain distribution of the numerical model at the corresponding rotation

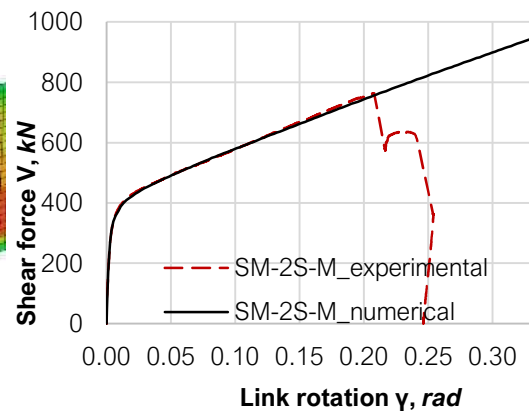


Figure 115 – Numerical vs. experimental response curves of the calibrated model

7.3 RESULTS

In order to assess the effect of the geometric imperfections, the five FE models described in the previous sections were subjected to monotonic loading and evaluated in a dynamic implicit analysis.

In Tables 24-25 are presented the main results for each model (1 – without imperfections, 2 – with imperfections applied as buckling modes, 3 – with imperfections applied as code-based pressure loads, 4 – with imperfections applied as measured values from a 3D scan, 5 – model developed directly from a 3D scan), in terms of plastic strain (PEEQ) and displacement (U3), for two different values of link rotation (0.15 rad and 0.30 rad).

Comparing the results in case of the model without any geometric imperfections and the models that account for imperfections, it is clearly visible that they substantially affect the behaviour of the link.

Applying imperfections as buckling mode has shown the lowest similarity to the real behaviour of the link during the experimental test.

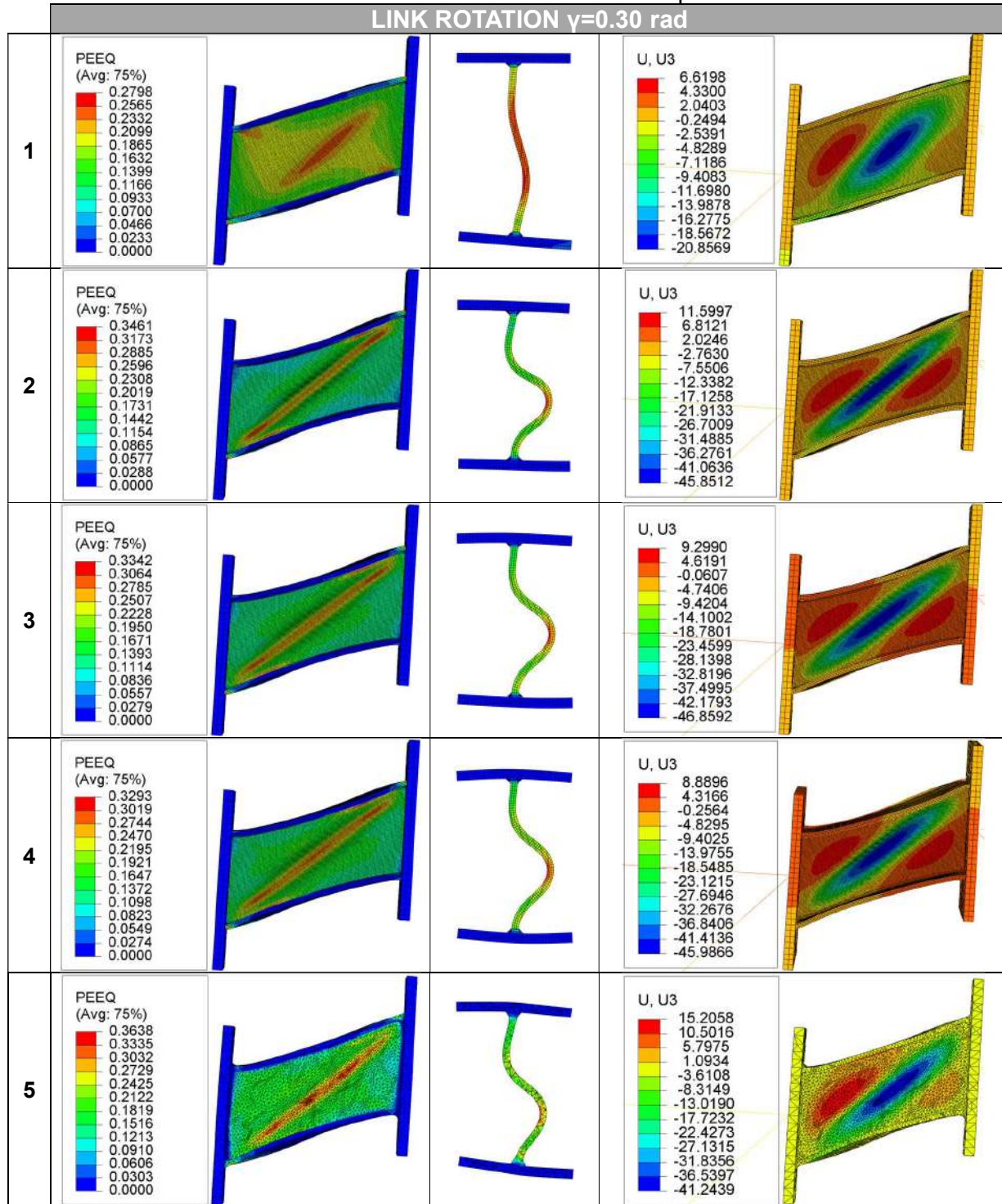
More reliable results were obtained by applying geometric imperfections as pressure loads. However, the actual value used for applying the pressure load, whether it is code-based or measured by 3D scanning has a remarkably similar effect. Thus, it is demonstrated that the deformed shape of the geometric imperfections is more important compared to their value.

It was observed that the model developed directly from the 3D scan, reflects the real behavior of the link with the greatest fidelity of all, in terms of the deformed allure of the specimen (local buckling shape and direction on the link web).

Table 24 – Results obtained for link rotation equal to 0.15 rad

LINK ROTATION $\gamma=0.15$ rad					
1	<p>PEEQ (Avg: 75%)</p>			<p>U, U3</p>	
2	<p>PEEQ (Avg: 75%)</p>			<p>U, U3</p>	
3	<p>PEEQ (Avg: 75%)</p>			<p>U, U3</p>	
4	<p>PEEQ (Avg: 75%)</p>			<p>U, U3</p>	
5	<p>PEEQ (Avg: 75%)</p>			<p>U, U3</p>	

Table 25 – Results obtained for link rotation equal to 0.30 rad



By analysing the link shear force – link rotation diagram (see Figure 116), it is shown that the effects of geometric imperfections appear at approximately 0.09 radians. This value corresponds with the local buckling of the link web. In case of the model developed directly from the 3D scan, higher strength was observed till the value of 0.09 radians (local buckling phenomena of the link web), in comparison with the other models. After this value, the allure of the curve is the similar as for the models with imperfections applied as pressure load. Between the model with code-based values for the pressure load and the one based on the measured values for the pressure load, the results almost overlap.

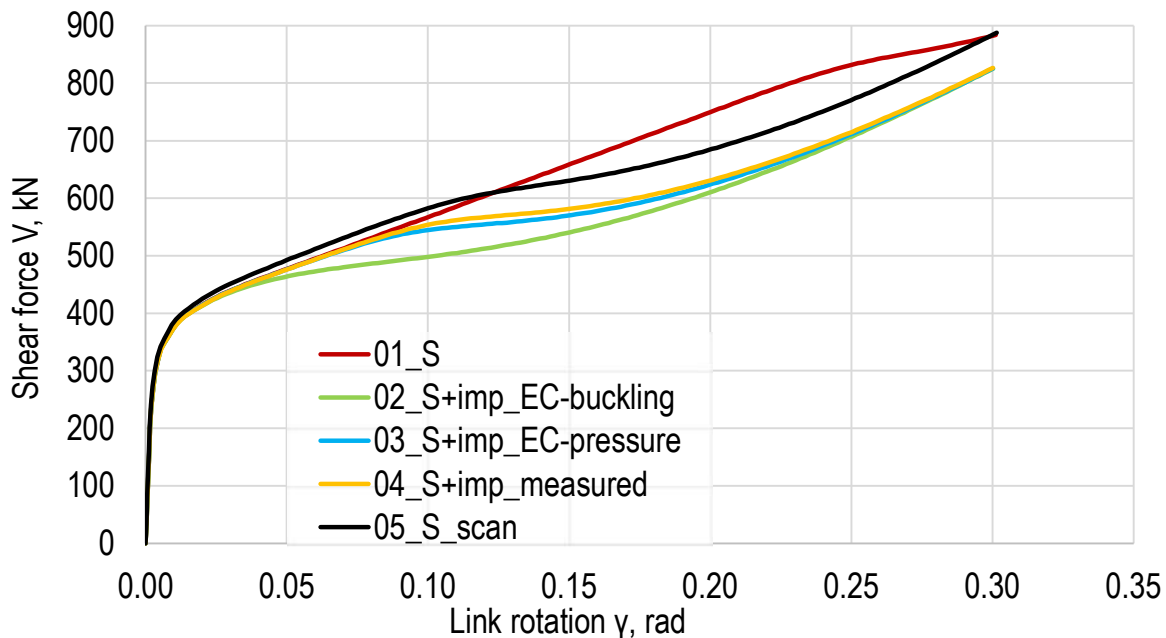


Figure 116 – Link shear force – rotation diagram for investigated link models

The numerical results reflect with high fidelity the real behaviour of the specimen during the experimental test. As shown in Figure 117, during the experimental test the phenomena that occurred first due to the geometric imperfections is the local buckling of the link web. The shape and direction (diagonal loop) of the web deflection is similar between the numerical and experimental test.

The FE model developed directly from the 3D scan, has shown the closest behaviour to the experimental test. Comparing the U3 results from the numerical analysis in Abaqus, with the real shape of the specimen (see Figure 118), in both cases it is possible to identify the 3 semi-waves (two smaller positive and one large negative) on the diagonal of the link.

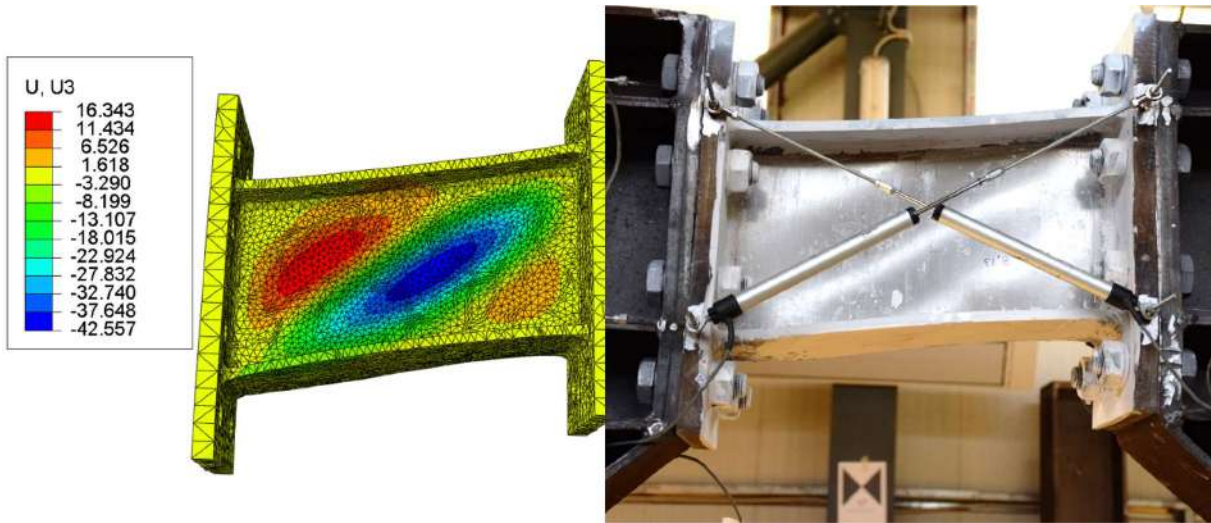


Figure 117 – Plastic strain distribution of the numerical model and buckling of the web of experimental specimen

CONCLUSIONS

A wide variety of technologies for digitally acquiring the shape of a 3D object and their current applications were presented and studied within this thesis. A relatively novel application of 3D scans in the field of civil engineering was proposed for investigation. Five different 3D scanning technologies were tested to consolidate the application on 3D modelling and measurement of geometric imperfections in case of steel links. General steps and procedures during the modelling process have been fully explained. Systems with unsuccessful results were also discussed to show the requirements and limitations of the method.

Terrestrial laser scanning technology (LiDAR) has proven highly accurate and independent of the lighting conditions of the surroundings and surface reflectiveness of the scanned object. However, it is not the most reliable option from an economic point of view, and the biggest disadvantage is represented by the need of a third-party program to obtain the 3D surface model (initial mesh model) from the point cloud.

Two different blue laser scanners were investigated within this work: with measuring arm and handheld. The blue laser scanner with measuring arm does not imply the use of targets on the measured specimen, but his scanning range is conditioned by the length of the measuring range, and the costs of this technology rise to six-figure values. Furthermore, the 3D surface models obtained directly from the embedded software have shown high quality in terms of measured dimensional values and imperfections. The handheld blue laser scanner was more flexible in use, being able to scan the whole surface of the specimens (allowing to change the initial position of the links). Also, the obtained 3D surface models were highly accurate, and the technology is more economically reliable. However, a major drawback is the necessity to use reflective targets on the measured specimen that can be time-consuming.

The structured light scanner had a similar accuracy to the blue laser scanners and the TLS, but the obtained 3D surface model is less qualitative (more holes and self-intersections were detected on the surface), this technology being more sensitive to the lighting conditions and surface reflectiveness. The actual measuring time was longer and the number of used targets on the specimens was higher. The quality-price ratio of such a device is still satisfactory.

The smartphone LiDAR scanner is still in a continuous development stage and has proven because of this reason a much lower accuracy than the other devices. Hopefully, in the near future it will be considered a reliable alternative for large-scale use due to its low price and versatility in obtaining the 3D surface model directly.

Converting the 3D surface model obtained from a scanning measurement into a valid solid model for FE analysis is yet not automated. For this scope, it was necessary to identify third-party programs that are able to feature this step. Only Autodesk Fusion 360 performed the conversion successfully.

Key steps in the editing of the imported 3D model in Abaqus CAE were introduced to ease the application of this method and eliminate common issues regarding 3D models in Abaqus CAE.

The current thesis presents a relatively novel and comprehensive method for accounting geometric imperfections of steel links in FE analysis, by using 3D scanning technology. The consideration of geometric imperfections has shown significant importance if the phenomenon of local buckling is expected. Geometrical imperfections applied as a buckling mode are least efficient in modelling the behaviour of the steel link. The application of imperfections as pressure loads reflects more accurately the real behaviour of the steel link. It is interesting to note that the shape of the imperfection is more important than the imperfection magnitudes (either code-based or measured) in reproducing the experimentally observed response.

FE models obtained directly from 3D scanning reflect most accurately the real behaviour of the steel link. The advance of 3D scanning technologies and post-processing programs in the future may also enhance its application in FEM. The development of software and computational ability of PC would also benefit the accuracy and efficiency in reconstructing 3D models of complicated structures. All the procedures of point cloud alignment, 3D surface model construction, repair of models, and conversion in a solid model may be integrated into a single program in the future to make the post-processing stage fully automatic.

REFERENCES

- [1] Bassier, M.; Vergauwen, M. Clustering of Wall Geometry from Unstructured Point Clouds Using Conditional Random Fields. *Remote Sens.* 2019, 11, 1586;
- [2] Furno, F.L.; Pietrucci, F.; Tommasi, C.; Mandelli, A. Un modello informativo parametrico per il Duomo di Milano-Test e sperimentazioni. *Archeomatica* 2017, 7, 22–25;
- [3] Chesoa, A. Stratan, and D. Dubina, “Design implementation of re-centring dual eccentrically braced frames with removable links,” *Soil Dyn. Earthq. Eng.*, vol. 112, pp. 174–184, 2018;
- [4] Stratan and D. Dubina, “Bolted links for eccentrically braced steel frames,” *The Netherlands: F.S.K. Bijlaard, A.M. Gresnigt, G.J. van der Vegte.*, Delft University of Technology, 2004, pp. 223–232;
- [5] Stratan, “Behaviour of multistorey dual steel structures located in seismic areas,” PhD, Politehnica, Timisoara, Romania, 2003;
- [6] A.P.P Jongenelen, D. G. Bailey, A.D. Payne, A.A. Dorrington, D.A. Carnegie, Analysis of Errors in ToF Range Imaging with Dual-Frequency Modulation, *IEEE Transactions on Instrumentation and Measurement*, Vo. 60, No. 5, May 2011, SSN 0018-9456;
- [7] Angelini, Maria & Baiocchi, Valerio & Costantino, Domenica & Garzia, F., (2017). Scan To Bim For 3d Reconstruction Of The Papal Basilica Of Saint Francis In Assisi In Italy. *Isprs - International Archives of the Photogrammetry, Remote Sensing and Spatial Information Sciences.* XLII-5/W1. 47-54. 10.5194/isprs-archives-XLII-5-W1-47-2017;
- [8] Angjeliu, Grigor & Coronelli, Dario & Cardani, Giuliana. (2020). Development of the simulation model for Digital Twin applications in historical masonry buildings: The integration between numerical and experimental reality. *Computers & Structures.* 238. 106282. 10.1016/j.compstruc.2020.106282;
- [9] ANSI/AISC 341-16. An American National Standard. Seismic Provisions for Structural Steel Buildings.” American Institute of Steel Construction, 2016;

- [10] Barazzetti, L.; Banfi, F.; Brumana, R.; Previtali, M. Creation of parametric BIM objects from point clouds using NURBS. *Photogramm. Rec.* 2015, 30, 339–362;
- [11] Barazzetti, Luigi & Banfi, Fabrizio & Brumana, R. & Gusmeroli, G. & Oreni, Daniela & Previtali, M. & Roncoroni, F. & Schiantarelli, G.. (2015). BIM From Laser Clouds and Finite Element Analysis: Combining Structural Analysis and Geometric Complexity. *ISPRS - International Archives of the Photogrammetry, Remote Sensing and Spatial Information Sciences*. XL-5/W4. 345-350. 10.5194/isprsarchives-XL-5-W4-345-2015;
- [12] Brian Curless (November 2000). "From Range Scans to 3D Models". *ACM SIGGRAPH Computer Graphics*. 33 (4): 38–41. doi:10.1145/345370.345399. S2CID 442358;
- [13] Castellazzi, Giovanni & D'Altri, Antonio & Bitelli, Gabriele & Selvaggi, Ilenia & Lambertini, Alessandro. (2015). From Laser Scanning to Finite Element Analysis of Complex Buildings by Using a Semi-Automatic Procedure. *Sensors*. 15. 18360. 10.3390/s150818360;
- [14] Cazals F., Giesen J.: Delaunay triangulation based surface reconstruction. In *Effective Computational Geometry for Curves and Surfaces*. Springer, 2006. 3;
- [15] Charbon, E. & Fishburn, Matt & Walker, Richard & Henderson, Robert & Niclass, Cristiano. (2013). SPAD-based sensors. *TOF Range-Imaging Cameras*. 11-38. 10.1007/978-3-642-27523-4_2;
- [16] *Close Range Photogrammetry. Principles, Methods and Applications*, by Thomas Luhmann, Stuart Robson, Stephen Kyle and Ian Harley, Whittles Publishing, ISBN 1-870325-50-8, 2006;
- [17] D. Dubina, A. Stratan, and F. Dinu, "Dual high-strength steel eccentrically braced frames with removable links," *Earthq. Eng. Struct. Dyn.*, vol. 37, no. 15, pp. 1703–1720, 2008;
- [18] Davidson, Ryan J., "A Comparison of Moiré Interferometry And Digital Image Correlation" (2008). *Theses and Dissertations*. 2676;
- [19] Dongdong Xu, Yuanqing Wang, Xiaoling Liu, Boshan Chen, Yidu Bu, A novel method and modelling technique for determining the initial geometric

imperfection of steel members using 3D scanning, Structures, Volume 49, 2023, Pages 855-874, ISSN 2352-0124, <https://doi.org/10.1016/j.istruc.2023.01.136>;

[20] James S. Aber, Irene Marzloff, Johannes B. Ries, Small-Format Aerial Photography, Elsevier, 2010, Pages 23-39, ISBN 9780444532602, <https://doi.org/10.1016/B978-0-444-53260-2.10003-1>;

[21] Eigenraam, P.; Borgart, A. Reverse engineering of free form shell structures; From point cloud to finite element model. Heron 2016, 61, 193;

[22] EN 1993-1-1:2005. Eurocode 3: Design of steel structures - Part 1-1: General rules and rules for buildings;

[23] EN 1998-1:2004. Eurocode 8: Design of structures for earthquake resistance - Part 1: General rules, seismic actions and rules for buildings.”;

[24] Fausto Bernardini, Holly E. Rushmeier (2002). "The 3D Model Acquisition Pipeline". Computer Graphics Forum. 21 (2): 149–172. CiteSeerX 10.1.1.94.7486. doi:10.1111/1467-8659.00574. S2CID 15779281;

[25] Feng, Peng & Zou, Yichong & Lili, hu & Liu, TianQiao. (2019). Use of 3D laser scanning on evaluating reduction of initial geometric imperfection of steel column with pre-stressed CFRP. Engineering Structures. 198. 109527. 10.1016/j.engstruct.2019.109527;

[26] Foschi, Renato & Leone, Matteo. (2009). Galileo, Measurement of the Velocity of Light, and the Reaction Times. Perception. 38. 1251-9. 10.1068/p6263;

[27] François, Marc & Bloch, Alexis & Thomas, Jean-Christophe. (2016). Metrology of Contours by the Virtual Image Correlation Technique. 10.1007/978-3-319-22446-6_30;

[28] Fregonese, L.; Achille, C.; Adami, A.; Fassi, F.; Spezzoni, A.; Taffurelli, L. BIM: An integrated model for planned and preventive maintenance of architectural heritage. 2015 Digit. Herit. 2015, 2, 77–80;

[29] Funari, Marco & Hajjat, Ameer & Masciotta, Maria & Oliveira, Daniel & Lourenco, Paulo. (2021). A Parametric Scan-to-FEM Framework for the Digital Twin Generation of Historic Masonry Structures. Sustainability. 13. 10.3390/su131911088;

- [30] Guarnieri, Alberto & Pirotti, Francesco & Pontin, M. & Vettore, Antonio. (2008). Combined 3d Surveying Techniques For Structural Analysis Applications;
- [31] H. Hu, T.M. Fernandez-Steeger, M. Dong, R. Azzam, Numerical modeling of LiDAR-based geological model for landslide analysis, Automation in Construction, Volume 24, 2012, Pages 184-193, ISSN 0926-5805;
- [32] Ignasi Fernandez, Jesús Miguel Bairán, Antonio R. Marí, 3D FEM model development from 3D optical measurement technique applied to corroded steel bars, Construction and Building Materials, Volume 124, 2016, Pages 519-532, ISSN 0950-0618;
- [33] J. Horswell, Recording, Editor(s): Jay A. Siegel, Pekka J. Saukko, Max M. Houck, Encyclopedia of Forensic Sciences (Second Edition), Academic Press, 2013, Pages 368-371, ISBN 9780123821669, <https://doi.org/10.1016/B978-0-12-382165-2.00207-5>;
- [34] James S. Aber, Irene Marzloff, Johannes B. Ries, Chapter 3 – Photogrammetry;
- [35] Kazhdan, Michael M. et al. “Poisson surface reconstruction.” Eurographics Symposium on Geometry Processing (2006);
- [36] León-Robles, C.A.; Reinoso-Gordo, J.F., González-Quiñones, J.J. Heritage building information modeling (H-BIM) applied to a stone bridge. ISPRS Intern. J. Geo-Inf. 2019, 8, 121;
- [37] Lizhuang Cui, Lizhi Zhou, Quanyi Xie, Jian Liu, Bo Han, Tiantao Zhang, Hongzheng Luo, Direct generation of finite element mesh using 3D laser point cloud, Structures, Volume 47, 2023, Pages 1579-1594, ISSN 2352-0124, <https://doi.org/10.1016/j.istruc.2022.12.010>;
- [38] Luetzenburg, G., Kroon, A. & Bjørk, A.A. Evaluation of the Apple iPhone 12 Pro LiDAR for an Application in Geosciences. Sci Rep 11, 22221 (2021). <https://doi.org/10.1038/s41598-021-01763-9>;
- [39] M. Hansard, S. Lee, O. Choi, R. Horaud, “Time-of-Flight Cameras: Principles, Methods and Applications”, Springer Brief in Computer Science, 2012;

- [40] Pepe M, Costantino D, Restuccia Garofalo A. An Efficient Pipeline to Obtain 3D Model for HBIM and Structural Analysis Purposes from 3D Point Clouds. *Applied Sciences*. 2020; 10(4):1235. <https://doi.org/10.3390/app10041235>;
- [41] prEN 1993-1-14: Design of steel structures — Design assisted by finite element analysis;
- [42] Raport științific și tehnic, Etapa 3: Încercări experimentale pe îmbinări sudate și linkuri, și elaborare recomandări de proiectare pentru linkuri hibride "HYLINK", 2022. Cod proiect: PN-III-P2-2.1-PED-2019-5427, Contractul de finanțare nr. 512PED/2020;
- [43] Roy Mayer, 1999. *Scientific Canadian: Invention and Innovation, From Canada's National Research Council*. Vancouver: Raincoast Books;
- [44] Shadmehri F, Hoa SV. Digital Image Correlation Applications in Composite Automated Manufacturing, Inspection, and Testing. *Applied Sciences*. 2019; 9(13):2719. <https://doi.org/10.3390/app9132719>;
- [45] Shadmehri, F.; Hoa, S.V. Digital Image Correlation Applications in Composite Automated Manufacturing, Inspection, and Testing. *Appl. Sci.* 2019, 9, 2719. <https://doi.org/10.3390/app9132719>;
- [46] T. Bell, B. Li, S. Zhang. *Structured light techniques and applications*. Wiley, 1999;
- [47] T. Bell, N. Karpinsky, and S. Zhang. *Real-Time 3D Sensing with Structured Light Techniques*. Wiley, 2014; pp 181–213;
- [48] Thomas Luhmann, Close range photogrammetry for industrial applications, *ISPRS Journal of Photogrammetry and Remote Sensing*, Volume 65, Issue 6, 2010, Pages 558-569, ISSN 0924-2716;
- [49] Trebuňa, Peter, Marek Mizerák, and Ladislav Rosocha. "3D Scanning technology and reconstruction." *Acta Simulatio* 4 (2018): 1-6;
- [50] Vacca, Giuseppina & Mistretta, Fausto & Stochino, Flavio & Dessi, A.. (2016). Terrestrial Laser Scanner For Monitoring The Deformations And The Damages Of Buildings. *Isprs - International Archives of the Photogrammetry, Remote Sensing and Spatial Information Sciences*. XLI-B5. 453-460. 10.5194/isprs-archives-XLI-B5-453-2016;

[51] Vilceanu C. B., Dungan L., Herban S., Popescu F. (2021). Using the laser scanning for conservation of cultural heritage buildings, Acta Technica Corviniensis – Bulletin Of Engineering Tome Xiv [2021] | Fascicule 3 [July – September];

[52] Wandinger, U. (2005). Introduction to Lidar. In: Weitkamp, C. (eds) Lidar. Springer Series in Optical Sciences, vol 102. Springer, New York, NY. https://doi.org/10.1007/0-387-25101-4_1;

[53] Wang, C.L. (June 2006). "Incremental reconstruction of sharp edges on mesh surfaces". Computer-Aided Design. 38 (6): 689–702;

[54] Xi Zhao, Mazdak Tootkaboni, Benjamin W. Schafer, Laser-based cross-section measurement of cold-formed steel members: Model reconstruction and application, Thin-Walled Structures, Volume 120, 2017, Pages 70-80, ISSN 0263-8231, <https://doi.org/10.1016/j.tws.2017.08.016>;

[55] XIE, Xiongyao & LU, Xiaozhi. (2017). Development of a 3D Modeling Algorithm for Tunnel Deformation Monitoring Based on Terrestrial Laser Scanning. Underground Space. 2. 10.1016/j.undsp.2017.02.001.

INTERNET SITES

- [1] http://vr.isdale.com/3DScanners/3d_scan_history/
- [2] <https://www.creaform3d.com/blog/the-history-of-metrology-from-galileo-to-optical-systems/>
- [3] http://um3d.dc.umich.edu/services/scanning/scan_intro_process.html
- [4] http://en.wikipedia.org/wiki/Coordinate-measuring_machine
- [5] http://www.nextec-wiz.com/fr_wizblade.html
- [6] <http://brownandsharpe.com/laser-metrology-solutions>
- [7] <http://brownandsharpe.com/products/coordinate-measuring-machines/non-contact-measurement/vision-metrology-solutions>
- [8] <http://www.ogpuk.com/>
- [9] http://en.wikipedia.org/wiki/3D_scanner
- [10] http://en.wikipedia.org/wiki/LIDAR#cite_note-cracknell-0
- [11] <https://www.creaform3d.com/blog/short-range-3d-scanning-technologies-an-overview/>

APPENDIX A

SYNTHESIS OF THE MATERIALS RESULTING FROM THE RESEARCH PRACTICE FOR THE ELABORATION OF THE DISSERTATION



UNIVERSITATEA DE ȘTIINȚE AGRONOMICE
ȘI MEDICINA VETERINARĂ – BUCUREȘTI



FACULTATEA
DE ÎMBUNĂȚĂȚIRI FUNCIARE
ȘI INGINERIA MEDIULUI

TO WHOM IT MAY CONCERN

Date 23.02.2023

Ref. No.: Journal of Young Scientist, FIFIM-UASVM Bucharest

We hereby certify that the article MONITORING STEEL STRUCTURES OVER TIME BY USING TERRESTRIAL LASER SCANNING TECHNIQUE FOR DISASTER PREVENTION, written by Paul Cristian ZDRENGHEA, Andreea Diana CLEPE, Viktor SZALAI was published in the Journal of Young Scientist, Volume IX, Bucharest, (ISSN 2344 – 1283, ISSN CD-ROM 2344 – 1291, ISSN ONLINE 2344 – 1305, ISSN-L 2344 – 1283) and is available online at the page <https://journalofyoungscientist.usamv.ro/> from January the 26th, 2023.

Lecturer Andreea OLTEANU, PhD

Executive Editor



APPENDIX B DEVIATION MEASUREMENT REPORT



MEASURING REPORT Raport de masurare Link

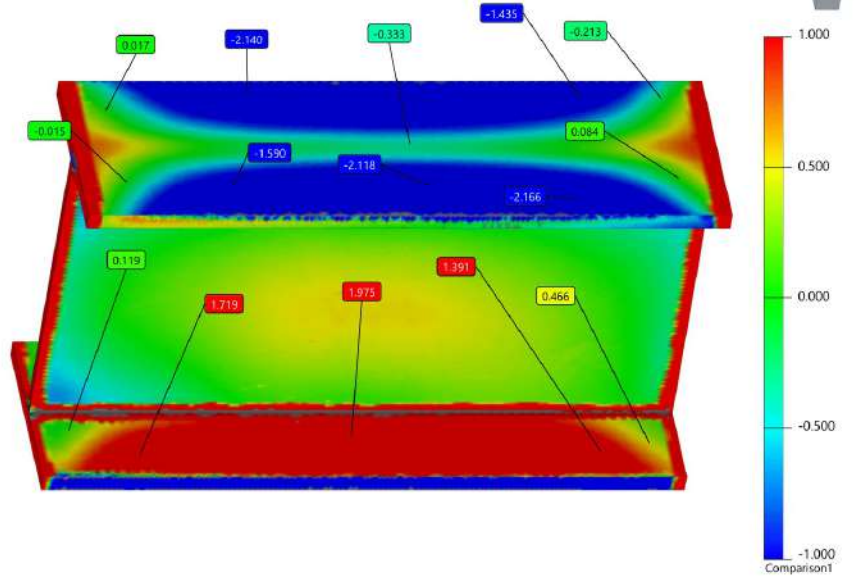


PART DESCRIPTION: Link
DATE: 4/20/2023
OPERATOR NAME: Liviu Salajan
EQUIPMENT: Absolute Arm 8525 - AS1
COMPANY: HEXAGON MANUFACTURING INTELLIGENCE ROMANIA

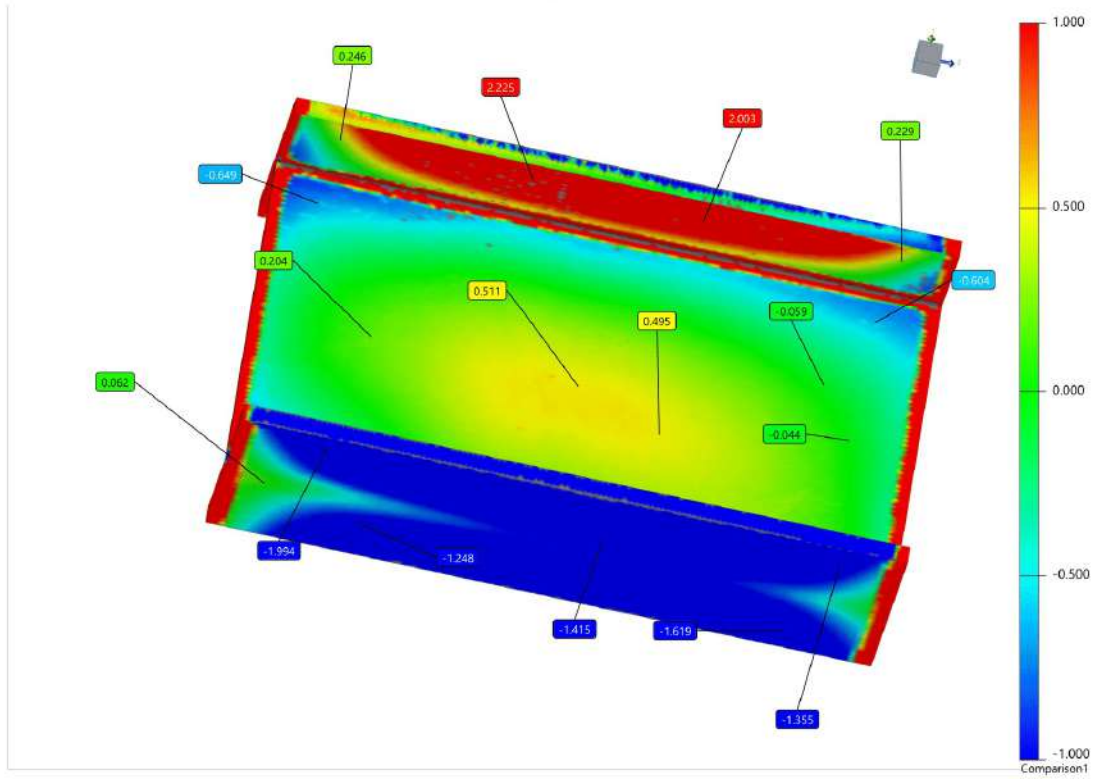
1
Not for Resale

4/20/2023

Harta de culori - diferentele dintre modelul 3d si piesa reala

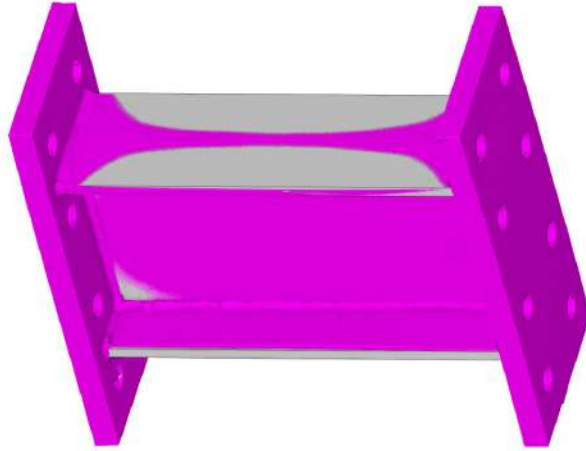


4/20/2023

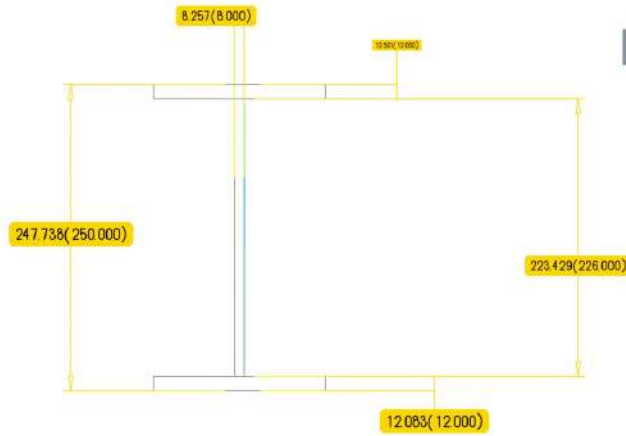
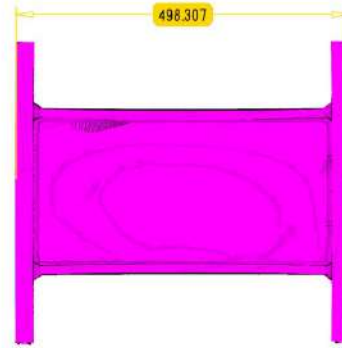


4/20/2023

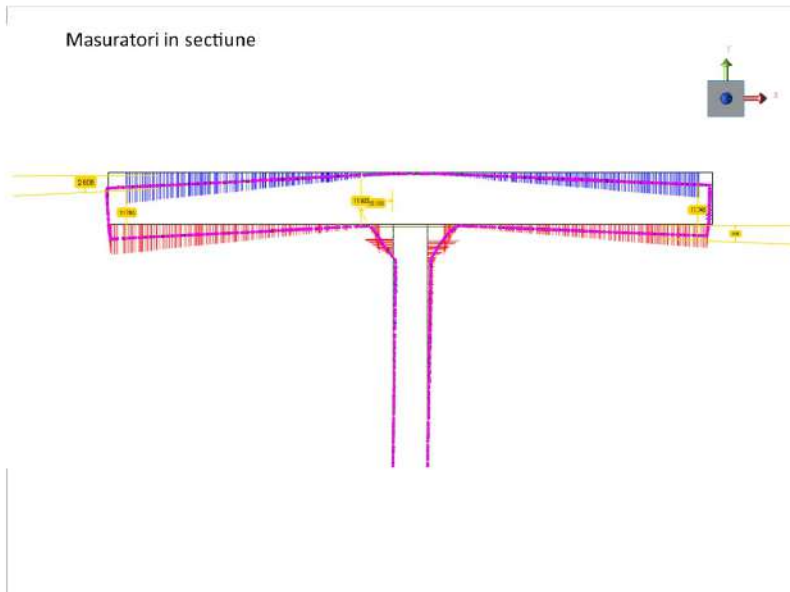
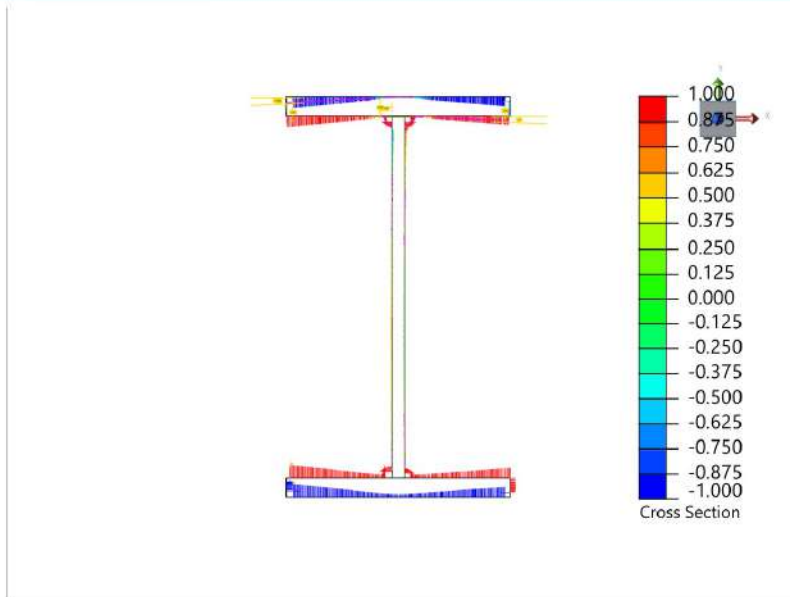
Suprapunere nor de puncte(piesa reala) cu modelul 3D



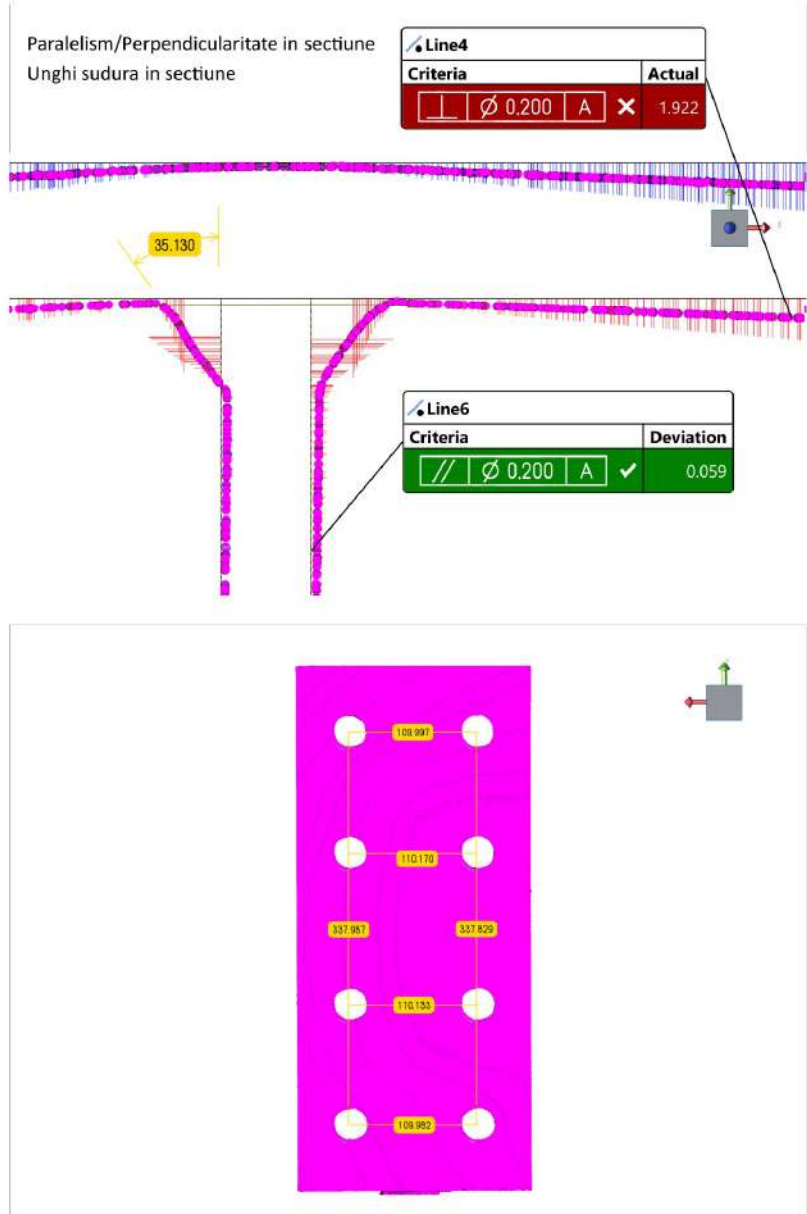
4/20/2023



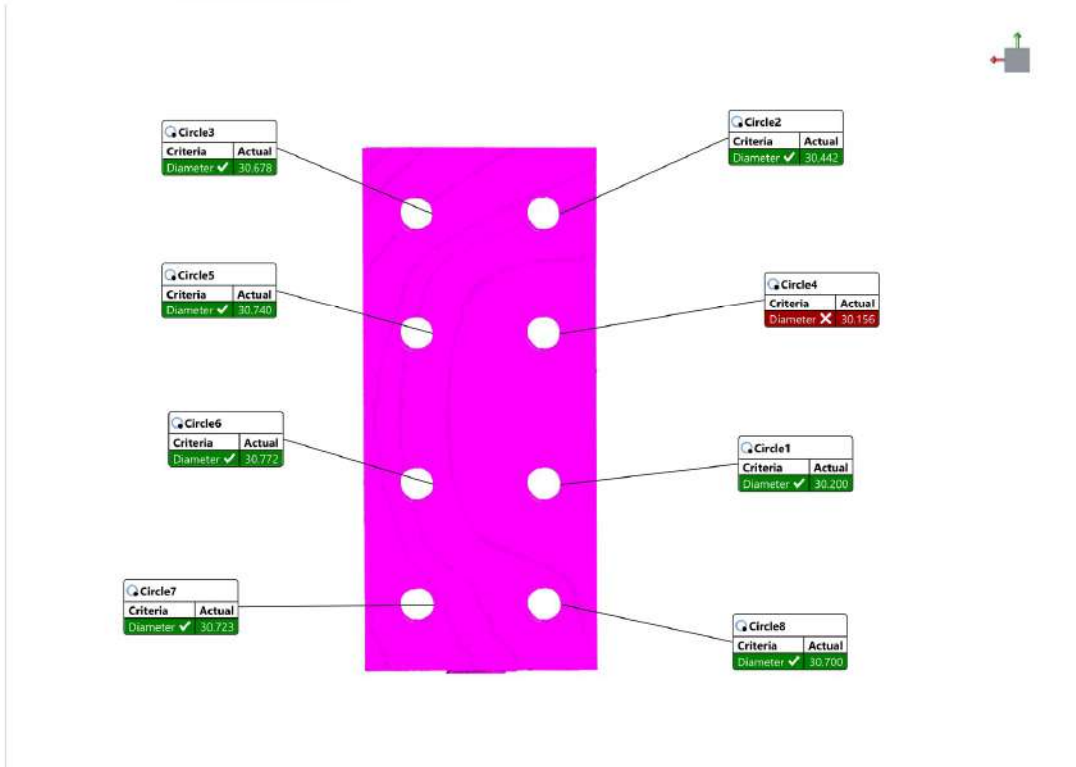
4/20/2023



4/20/2023



4/20/2023



Circle2 (Circle)					
Criteria	Nominal	Actual	Deviation	Tolerance	Amt Out
Diameter	30.500	30.442	-0.058	± 0.300	Green

Circle3 (Circle)					
Criteria	Nominal	Actual	Deviation	Tolerance	Amt Out
Diameter	30.500	30.678	0.178	± 0.300	Green

4/20/2023

Circle4 (Circle)					
Criteria	Nominal	Actual	Deviation	Tolerance	Amt Out
Diameter	30.500	30.156	-0.344	± 0.300	-0.044

Circle5 (Circle)					
Criteria	Nominal	Actual	Deviation	Tolerance	Amt Out
Diameter	30.500	30.740	0.240	± 0.300	

Circle6 (Circle)					
Criteria	Nominal	Actual	Deviation	Tolerance	Amt Out
Diameter	30.500	30.772	0.272	± 0.300	

Circle7 (Circle)					
Criteria	Nominal	Actual	Deviation	Tolerance	Amt Out
Diameter	30.500	30.723	0.223	± 0.300	

Circle8 (Circle)					
Criteria	Nominal	Actual	Deviation	Tolerance	Amt Out
Diameter	30.500	30.700	0.200	± 0.300	

Circle1 (Circle)					
Criteria	Nominal	Actual	Deviation	Tolerance	Amt Out
Diameter	30.500	30.200	-0.300	± 0.300	

Circle2 to Circle3-1 (Linear Dimension)					
Criteria	Nominal	Actual	Deviation	Tolerance	Amt Out
Length		110.000		---	

Circle4 to Circle5-1 (Linear Dimension)					
Criteria	Nominal	Actual	Deviation	Tolerance	Amt Out
Length		110.173		---	

Circle6 to Circle1-1 (Linear Dimension)					
Criteria	Nominal	Actual	Deviation	Tolerance	Amt Out
Length		110.136		---	

Circle8 to Circle7-1 (Linear Dimension)					
Criteria	Nominal	Actual	Deviation	Tolerance	Amt Out
Length		109.986		---	

Circle3 to Circle7-1 (Linear Dimension)					
Criteria	Nominal	Actual	Deviation	Tolerance	Amt Out
Length		337.990		---	

Circle2 to Circle8-1 (Linear Dimension)					
Criteria	Nominal	Actual	Deviation	Tolerance	Amt Out
Length		337.832		---	

Plane5 to Plane7-1 (Linear Dimension)					
Criteria	Nominal	Actual	Deviation	Tolerance	Amt Out
Length	12.000	12.083	0.083	---	

4/20/2023

Plane3 to Plane8-1 (Linear Dimension)					
Criteria	Nominal	Actual	Deviation	Tolerance	Amt Out
Length	8.000	8.257	0.257	---	

Plane4 to Plane6-1 (Linear Dimension)					
Criteria	Nominal	Actual	Deviation	Tolerance	Amt Out
Length	12.000	12.301	0.301	---	

Plane6 to Plane7-1 (Linear Dimension)					
Criteria	Nominal	Actual	Deviation	Tolerance	Amt Out
Length	250.000	247.738	-2.262	---	

Plane4 to Plane5-1 (Linear Dimension)					
Criteria	Nominal	Actual	Deviation	Tolerance	Amt Out
Length	226.000	223.430	-2.570	---	

**STATEMENT REGARDING
THE AUTHENTICITY OF THE THESIS PAPER ***

I, the undersigned VIKTOR SZALAI,
Identifying myself with IDENTITY CARD series TZ no. 590155,
CNP (personal numerical code) 1980620350016
author of the thesis paper 3D SCANNING IMPERFECTION MEASUREMENTS FOR
FEM ANALYSIS OF STEEL LINKS


Developed with the purpose of participating in the graduation examination completing the educational level of MASTER organized by the Faculty of CIVIL ENGINEERING within the Politehnica University of Timișoara, session JUNE 2023 of the academic year 2022-2023, coordinated by PROF. DR. ENG. AUREL STRATAN, considering Article 34 of the *Regulation on the organization and conduct of bachelor/diploma and dissertation examinations*, approved by Senate Decision no. 109/14.05.2020, and knowing that in the event of subsequent finding of false statements, I will bear the administrative sanction provided by Art. 146 of Law no. 1/2011 – law of national education, namely the cancellation of the diploma of studies, I declare on my own responsibility that:

- This paper is the result of my own intellectual endeavour,
- The paper does not contain texts, data or graphic elements taken from other papers or from other sources without such authors or sources being quoted, including when the source is another paper / other works of my own;
- bibliographic sources have been used in compliance with Romanian legislation and international copyright conventions.
- this paper has not been publicly presented, published or presented before another the bachelor/diploma/dissertation examination committee.
- In the development of the paper I have not used instruments specific for artificial intelligence (AI)¹.

I declare that I agree that the paper should be verified by any legal means in order to confirm its originality, and I consent to the introduction of its content in a database for this purpose.

Timișoara,

Date 15.06.2023

Signature 

* The statement will be filled-in by the student, will be signed by hand by them and inserted at the end of the thesis paper, as a part of it.

¹ One of the variants will be selected and inserted in the statement: 1 – AI has been used, and the source will be mentioned, 2 – AI has not been used

